Important Notice

UNIVERSITY OF CALGARY

Near-surface S-wave traveltime corrections and inversion: a raypath-consistent and interferometric approach

by

Raul Jose Cova Gamero

A THESIS
SUBMITTED TO THE FACULTY OF GRADUATE STUDIES
IN PARTIAL FULFILLMENT OF THE REQUIREMENTS FOR THE
DEGREE OF DOCTOR OF PHILOSOPHY

GRADUATE PROGRAM IN GEOLOGY AND GEOPHYSICS

CALGARY, ALBERTA
AUGUST, 2017

Abstract

Removing near-surface effects in the processing of 3C data is key to exploiting the information provided by converted waves, particularly for the case of the PS mode where converted energy travels back to the surface as S-waves. The very low velocity of S-waves amplifies the distortions introduced by the near-surface in the PS-traveltimes. This is usually solved by computing the vertical traveltimes in the near-surface layer and removing them from the data in a surface-consistent framework. However, if the velocity change between the near-surface layer and the medium underneath is small, the vertical raypath assumption that supports the surface-consistent approach is no longer valid. This property results in a non-stationary change of the near-surface traveltimes that needs to be addressed to properly remove its effect. I show how the delays introduced by the presence of very low S-wave velocities in the near-surface can introduce raypath-dependent effects which can be larger than what can be considered a residual static. In this study, a raypath-consistent solution for removing near-surface traveltime effects is proposed. This is achieved by transforming the data, organized into receiver gathers, to the τ-p domain and performing crosscorrelation and convolution operations to capture and remove the near-surface delays from the data. The τ-differences captured during the interferometric processing of the near-surface effects are then used in an inversion algorithm to estimate the S-wave velocities in the near-surface. This processing work-flow provides not only a set of corrections but also a velocity model that is based on them. I tested this method on synthetic and field data. In both cases, removing near-surface time delays in a raypath-consistent framework improved coherency and stacking power of shallow and deep events simultaneously. Shallow events benefited most from this processing due to their wider range of reflection angles. This approach can be useful in the processing of wide-angle broadband data, where the kinematics of wave propagation are not consistent with vertical raypath approximations in the near-surface. Additionally, this method provides a near-surface S-wave velocity model that can be used for building migration velocity models or to initialize elastic full waveform inversions.

Acknowledgements

First and foremost, immense thanks to my supervisor Dr. Kris Innanen for all his help and support. I am grateful to him for giving me the freedom to pursue a topic of great interest to me, and for his constant encouragement and positivity.

Special thanks to David Henley for all his support and help during the last years. Much of this work was inspired by his research. It has been a great pleasure for me working with such an amazing person.

I also would like to extend my gratitude to CREWES leadership, Dr. Don Lawton, Dr. Larry Lines, Dr. Gary Margrave and Dr. Daniel Trad for their comments and suggestions through the years. Thanks also to CREWES staff, especially to Laura Bird for always being willing to help with anything I needed.

I gratefully acknowledge the sponsors of the CREWES Project and the Natural Science and Engineering Research Council of Canada (NSERC) for providing most of the funding that made this research possible. I am also grateful to the University of Calgary International Doctoral Scholarship and the Canadian Society of Exploration Geophysicist (CSEG) for their funding.

Thanks to all my fellow CREWES students, especially to Adriana Gordon, Marcelo Guarido, Wenyong Pan, Tianci Cui, Rafael Azuaje, Scott Keating, Shahin Jabbari and Faranak Mahmoudian for their friendship and support. I also would like to acknowledge my friend Dr. Babatunde Arenrin. His kindness and willingness to help everyone were infinite. I am sure he still lives in the memory of those who were lucky of having him in their life.

I would like to thank all my family, especially to my parents Nancy Gamero, Jose Guillen, Raul Cova, Elba Leon and my aunt Eladia Gamero. Their support and unconditional love were critical for achieving this goal. Immense thanks also to my grandmother Maria Boadas de Gamero, "Maita", for raising a family where education was a core value. Her wisdom and infinite love will always live in my memory.

Last but not least, infinite thanks to my wife Michelle Montano. Her support, patience, and love made every day of my studies to be filled with joy and happiness.

Dedication

To the three most important women in my life.

Three generations that define what I am today;

Maita, my grandmother, for her unconditional love;

Nancy, my mother, for always encouraging me to aim higher;

Michelle, my wife, for sharing this journey with me.

Contents

List of Figures

Chapter 1

Introduction

The development of multicomponent sensors for seismic data acquisition has enabled geophysicists to exploit different wave-modes that were not possible to study by using single component (vertical) sensors. Since then, the processing and interpretation of converted PS-waves has begun to play an important role in the analysis of seismic data.

Similarly, acquisition designs have experienced significant changes. Broadband, wide-offset and wide-azimuth are terms that are gaining significant attention in the geophysics community. Developments in multi-parameter full waveform inversion (FWI) also highlight the need for long-offset and wide-angle data to overcome crosstalk between model parameters (Operto et al., 2013; Virieux and Operto, 2009).

Under these conditions, processing geophysicists are required to revisit their methods as the data acquisition practices and instrumentation evolve. One of the first and most important steps in any seismic data processing work-flow is the application of the so called static corrections. Hence, it is natural to start the revision with this process since it may affect the rest of the processing sequence.

Transferring known methods for P-wave static corrections to the processing of converted-wave data has proven to be a difficult task (Tatham et al., 1991). Two issues are particularly problematic to overcome. First, very little a priori information or data about S-wave velocities in the near-surface is usually available. Specifically, refraction arrivals, which are the primary source of information for processing P-wave static corrections, are usually not available for the S-wave mode or are hard to identify.

Secondly, the very low velocity of S-waves in the near-surface results in larger static problems. S-wave static corrections can be between two to six times as large as P-wave corrections (Cox, 1999). Therefore, some of the approximations used for processing P-wave statics might not be sufficiently accurate to properly remove near-surface effects from converted-wave events.

These two peculiarities of the S-wave near-surface corrections for the processing of converted-

wave data are the main motivation of this thesis. Even though most of this research deals with the near-surface correction itself, I am also interested in reproducing the associated near-surface velocity structure responsible. This velocity information can be useful for converted-wave imaging and may also be an important input for the creation of starting models for elastic full waveform inversion algorithms.

1.1 Static corrections

In the context of the seismic reflection method, the term static corrections is used to refer to the corrections needed to compensate for the effects of variation in elevation, weathering thickness, weathering velocity, or reference to a datum (Sheriff, 2002). The use of the term "static" in the name of the correction means that a constant correction is needed to remove these near-surface effects from all the events recorded on a seismic trace. In this context, the term near-surface refers to the shallowest part in the subsurface where non-consolidated or low-velocity sediments are usually present. This condition is usually encountered within the first hundred of meters of the subsurface Cox (1999).

Figure 1.1a shows a schematic cross-section of the conditions at which seismic field experiments are usually recorded. The subsurface model consists of two layers; the weathered layer, limited by the surface and the base of the weathering, and the sub-weathering layer, down to the reflector. Lateral variations in the thickness and velocity of the weathering layer introduce additional traveltimes to the reflected wavefields. Such distortions often result in the introduction of false structures in the subsurface image. Static effects can also impact the vertical resolution and stacking power of the seismic data, affecting the coherency and continuity of the seismic events. If not properly addressed the interpretation of the subsurface structures may be compromised (Cox, 1999).

The goal of static corrections is to remove the traveltimes introduced by the weathering layer to simulate the field experiment illustrated in Figure 1.1b where the weathering layer is not present. This is usually achieved in two steps. First, the source and the receiver are redatumed to the base of the weathering layer (Figure 1.2a), and this traveltime is replaced by the one that would have been obtained with the velocity of the replacement medium.

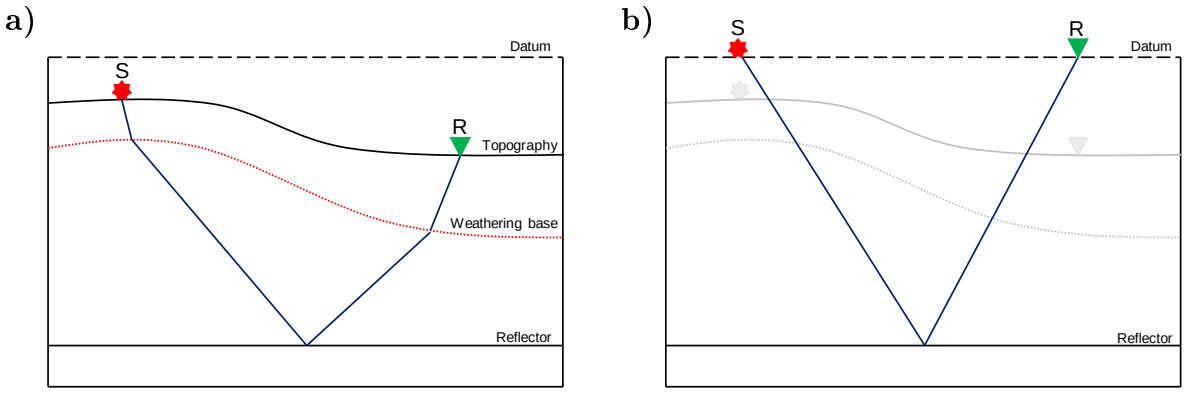

Figure 1.1: (a) Schematic cross-section of typical surface seismic experiment with raypath from source (S) to receiver (R). (b) Idealised cross-section after static corrections. The effect of the near-surface layer has been removed and, the source and the receiver have been re-datumed.

This can be expressed as

$$\Delta t_w = \frac{z_w}{v_1} - \frac{z_w}{v_0}, \tag{1.1}$$

where Δt_w is the weathering correction, z_w is the depth of the weathering base and v_0 and v_1 are the velocities in the weathering and the medium underneath. The medium with velocity v_1 is usually referred to as the replacement medium due to its role in the correction.

Secondly, the source and the receiver are moved to the final datum using the velocity of the replacement medium (Figure 1.2b). This step, also known as the elevation correction, can be written as

$$\Delta t_e = \frac{z_d - z_0}{v_1}, \tag{1.2}$$

where z_d is the elevation of the final datum and z_0 is the receiver or source elevation.

Since the near-surface and elevation conditions at the receiver and source locations can be different, the correction at each element is computed independently. The total static correction is then the sum of the weathering and elevation corrections at both the receiver and source locations at which each trace was recorded. Hence, the total static correction (Δt_T) is,

$$\Delta t_T = (\Delta t_{w,S} + \Delta t_{e,S}) + (\Delta t_{w,R} + \Delta t_{e,R}) \tag{1.3}$$

$$= \Delta t_S + \Delta t_R \tag{1.4}$$

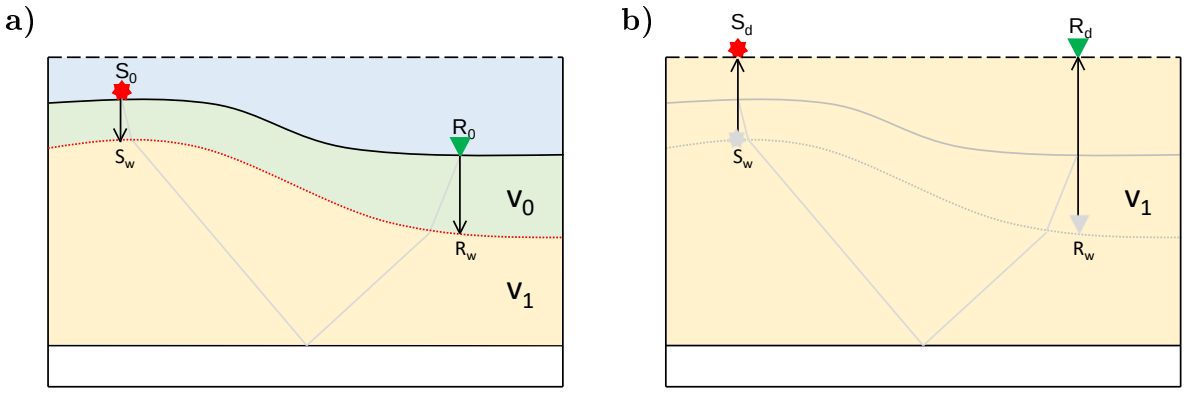

Figure 1.2: (a) Redatuming of the source and receiver locations down to the base of the weathering layer. S_w and R_w denotes the depth of the base of the weathering layer underneath each element. (b) The source and the receiver are redatumed to the final datum using the velocity v_1. As a result, the effect of the weathering layer and the topography have been removed from the data.

where Δt_S is the source static correction and Δt_S is the receiver static correction.

In the redatuming process depicted in Figure 1.2, the source and receiver locations are moved up and down following a vertical trajectory. This simplification is supported by the assumption that raypaths in the near-surface are nearly-vertical ($< 15°$) (Cox, 1999). As predicted by Snell's Law, this will occur in areas where a significant increase of velocity between the near-surface layer and the medium underneath exists. Based on this assumption, the near-surface effects are usually framed as a surface-consistent problem. Under this framework, all raypaths which travel through the same region will be affected in the same way (Sheriff, 2002). In the case of static corrections, this implies that the magnitude of the correction is constant for all the time samples recorded at each source or receiver location. Therefore, all the traces recorded at a fixed receiver location will undergo the same receiver static correction. The same principle applies for all the traces recorded using the same source location.

Static corrections are usually derived from three data sources. Static corrections derived from the direct measurement of vertical traveltimes from a buried source are known as uphole-based statics. Although this is the most accurate technique for characterizing the near-surface layers, in some cases the source depth might not be deep enough to sample the

complete thickness that affects seismic events.

The most common method to address static corrections is by using the arrivals of critically-refracted waves. Several methods and approximations have been published in the literature. Among these one can find the ABC method (Survey et al., 1931), Hagedoorn or plus-minus method (Hagedoorn, 1959), generalized reciprocal method or GRM (Palmer, 1980), and the Gardner method (Gardner, 1939). These methods provide a near-surface velocity model by the inversion of refraction traveltimes. The output velocity model is then used to compute the near-surface correction at each receiver and source location.

The third set of solutions to static corrections are usually referred to as data-smoothing static methods. In this case, common traveltime irregularities along seismic events are assumed to be the results of near-surface variations. Hence, near-surface corrections using this approach are computed by generating solutions that minimize such irregularities. The minimization is often accomplished by using a process dubbed trim static corrections. In this process, time shifts are picked from the crosscorrelation between an individual trace and a model or pilot trace. The reference trace is usually computed from stacking several traces with a common geometrical feature. Trim static corrections are a type of non-surface-consistent solution in the sense that they are not tied to any geometrical feature. Therefore, traces generated by the same source or recorded at the same receiver location may receive different static corrections.

The method developed in this thesis can be classified as a data-smoothing technique. The main reason for this is that the data needed to apply uphole- or refraction-based methods are usually not available for the processing of S-wave statics. However, in contrast to trim static corrections, my proposal is raypath-dependent. A brief introduction about S-wave static corrections is given in the next section.

1.2 Shear-wave static corrections for converted wave data processing

In multicomponent seismic data acquisition, where the arrivals of P- and S-waves at the surface can be recorded, one static solution for each wave-mode is needed. When acquiring seismic data using P-wave sources, most of the S-wave energy recorded at the surface is

the result of P-to-S conversions. These are produced at depths where changes in the rock impedance occur. Therefore, a P-wave static solution for the source side and a S-wave static solution for the receiver side will be needed to compensate for the total effect of the near-surface.

Due to the very low confining pressures in the near-surface, the propagation of S-waves occurs at very low velocities. As a result, S-wave near-surface effects on the traveltimes of converted-wave events are significant. This also implies that some of the simplifications (e.g. assuming vertical raypaths and sharp velocity contrasts in the near-surface) allowable when solving P-wave statics are inappropriate when computing S-wave statics. Since the velocity of S-waves is not significantly affected by the presence of fluids in the pores, the velocity structure of the near-surface "seen" by S-waves may differ from that controlling P-wave propagation (Cox, 1999). Moreover, S-wave velocity gradients in the near-surface can be lower than P-wave velocity gradients (Yilmaz, 2015). Therefore, the S-wave velocity contrast at the base of the near-surface may not be large enough to support the vertical raypath assumption. Also, the wider incidence angles needed to observe strong converted S-wave energy threaten this assumption (Cox, 1999). All these features make the computation of S-wave statics a very complex problem (Anno, 1983; Wiest and Edelmann, 1984; Tatham et al., 1991; Stewart et al., 2002).

The most simple approach for computing S-wave static corrections is to scale the P-wave corrections by the velocity ratio of each wave mode in the near-surface. This velocity ratio can be obtained from the analysis of surface-wave data, shallow borehole data or refracted waves. Although this might be enough for a first approximation, this approach does not yield optimum results (Cox, 1999; Garotta and Granger, 1988; Tessmer et al., 1990). These authors report lateral changes of V_p/V_s that range between two and six. Due to the particularities of the propagation of each wave mode, the two sets of static corrections should be considered independent (Cox, 1999).

Several methods have been proposed in the literature for solving S-wave statics under the surface-consistent assumption. Schafer (1991) shows a comparison of methods including hand-picked statics on common-receiver stacks (Garotta and Granger, 1988); time-difference refraction analysis (Lawton, 1989); generalized reciprocal inversion (Palmer, 1980); and

Monte Carlo simulated annealing (Eaton et al., 1991). All these methods rely on the picking of S-wave refractions or PS-wave events, which may be hard to identify at the early stages of the processing, and that may require significant amounts of time to complete.

More recently, near-surface characterization by inversion of ground roll dispersion for S-wave static corrections has gained attention. Askari et al. (2012), Socco et al. (2010) and Dulaijan and Stewart (2010) used the multi-spectral analysis of surface waves (MASW) to build near-surface S-wave velocity models and compute static corrections. However, the MASW may lack sufficient resolution when strong lateral variations of S-wave velocities are present (Lin and Lin, 2007) or when the near-surface is not horizontally layered (Bodet et al., 2005). Furthermore, the depth of investigation of surface waves is limited by the lowest reliable frequency recorded in the data. With this method, S-wave velocities can be reasonably calculated up to a maximum depth equal to half of the longest wavelength recorded (Fromm et al., 1991). Therefore, there is the risk that the near-surface thickness that can be characterized through surface waves might not be sufficient to remove near-surface effects from the converted-wave events.

Henley (2012) introduced an interferometric approach where no near-surface velocity model is needed. Instead of using a surface-consistent framework he introduces a raypath-consistent solution by processing the data in the radial-trace domain (Claerbout, 1983). In this thesis, I extend Henley's ideas to the τ-p domain where the kinematics of the wave propagation are more realistically approximated.

1.3 Seismic Interferometry

The term interferometry is generally used to refer to the study of interference patterns between two signals. The underlying goal is to obtain information about changes in the media where they propagate or to reconstruct information about the signals. Seismic interferometry can be defined as the study of interference of seismic-related signals (Curtis et al., 2006).

The mathematical operation at the heart of seismic interferometry is the crosscorrelation of pairs of signals. Figure 1.3 depicts a very simple application of this concept. There, a seismic trace that contains two reflection events (Figure 1.3a), is crosscorrelated with a

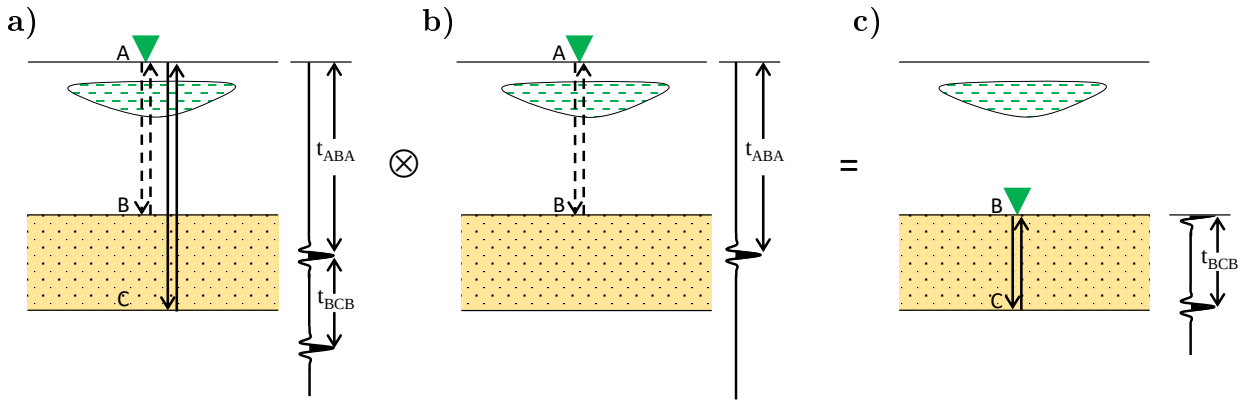

Figure 1.3: Schematic representation of an interferometric redatuming process. (a) Reflections recorded from the interfaces at depths B and C with traveltimes t_{ABA} and t_{ACA}. (b) Data containing only the reflection from the interface at depth B. (c) The output of the crosscorrelation of the data in (a) and (b) containing the traveltime that would have been recorded if the receiver were located at the base of the near-surface medium, avoiding the effect of any near-surface heterogeneity.

trace that only contains the reflection produced at the base of the first layer (Figure 1.3b). As a result, the new trace (Figure 1.3c) contains the events that would have been recorded as if the receiver had been placed at the base of the first layer, avoiding the effect of any heterogeneity in the near-surface.

Assuming an impulsive source expressed as a Dirac delta function $\delta(t)$, the zero offset data recorded at location A in Figure 1.3a can be written as,

$$d(A|A,t) = \delta(t - t_{ABA}) + \delta(t - t_{ACA}), \tag{1.5}$$

where $d(A|A,t)$ denotes the time-domain data recorded due to a source and receiver located at A and the delta functions represent the reflection arrivals produced at the subsurface points B and C, with total traveltimes t_{ABA} and t_{ACA}. No amplitude effects are considered in this example.

The Fourier transform of these data is,

$$D(A|A,\omega) = \frac{1}{2\pi}\left(e^{i\omega t_{ABA}} + e^{i\omega t_{ACA}}\right), \tag{1.6}$$

with ω denoting the angular frequency.

The trace in Figure 1.3b only contains the reflection from the base of the near-surface

medium, and its Fourier transformed representation is

$$D'(A|A,\omega) = \frac{1}{2\pi} e^{i\omega t_{ABA}}. \tag{1.7}$$

Invoking the crosscorrelation theorem, the crosscorrelation $C(A|A,\omega)$ of signals d and d', in the frequency domain is given by,

$$C(A|A,\omega) = 2\pi D'^{*}(A|A,\omega) D(A|A,\omega) \tag{1.8}$$

where the * symbol denotes the complex conjugate operator.

Substituting equations 1.6 and 1.7 in 1.8 yields

$$C(A|A,\omega) = 2\pi \left[\frac{1}{2\pi} e^{-i\omega t_{ABA}}\right] \left[\frac{1}{2\pi}\left(e^{i\omega t_{ABA}} + e^{i\omega t_{ACA}}\right)\right] \tag{1.9}$$

$$= \frac{1}{2\pi}\left(e^{i\omega (t_{ACA} - t_{ABA})} + 1\right) \tag{1.10}$$

$$= \frac{1}{2\pi}\left(e^{i\omega t_{BCB}} + 1\right) \tag{1.11}$$

Equation 1.11 represents the Fourier transform of the data that would have been recorded if the source and the receiver were located at the point B. Hence, the crosscorrelation operation equates to the subtraction of the ABA and ACA raypaths. This yields the traveltimes corresponding to the segment BCB as if the near-surface medium had not been present during the acquisition.

The multidimensional generalization of the process above, in terms of Green's functions, is given by the so called reciprocity equation of the correlation type (Schuster et al., 2004; Wapenaar, 2004) given by,

$$G(B|A,\omega) - G^{*}(A|B,\omega) = \int_S \left[G^{*}(x|B,\omega)\frac{\partial G(x|A,\omega)}{\partial n_x} - G(x|A,\omega)\frac{\partial G^{*}(x|B,\omega)}{\partial n_x}\right] d^2x. \tag{1.12}$$

Equation 1.12 allows to reconstruct the Green's function recorded at location A given a point source in B ($G(B|A,\omega)$), by crosscorrelating the Green's functions generated by a sources in the locations A and B. Then, following the integration over the recording surface S, all the output crosscorrelations are summed to obtain the reconstructed data. This operation equates to the search for and subtraction of shared raypaths between the $G(x|B,\omega)$ and $G(x|A,\omega)$ datasets. In the derivation of equation 1.12 it is assumed that the recording surface S encloses points A and B.

The convolutional form of equation 1.12, also known as the reciprocity equation of the convolution type (Schuster, 2009; Wapenaar and Fokkema, 2006) is given by,

$$G(B|A,\omega) - G_0(A|B,\omega) = \int_S \left[G_0(x|B,\omega) \frac{\partial G(x|A,\omega)}{\partial n_x} - G(x|A,\omega) \frac{\partial G_0(x|B,\omega)}{\partial n_x} \right] d^2x. \tag{1.13}$$

In contrast to equation 1.12, the reciprocity equation of the convolution type performs a search for and addition of the shared raypath between the datasets in the integrand.

According to Schuster (2009), a major benefit of seismic interferometry is that data can be redatumed closer to the imaging target without the need of static corrections or a near-surface velocity model. This is a result of the data acting as natural wavefield extrapolators. Moreover, by avoiding the distorting effects of the near-surface a better image resolution at the target level can be achieved.

However, the main problem with the reciprocity equations 1.12 and 1.13 is that a wide aperture of source and receivers is needed to produce a complete cancellation of coherent noise and avoid the presence of numerical artifacts in the reconstructed data (Schuster, 2009). This requires proper filtering of unwanted events before performing the crosscorrelation and convolution operations.

1.4 Thesis objective and overview

The main goal of this thesis is to propose, validate and apply a method for removing S-wave near-surface effects from converted-wave data, using interferometric concepts in a raypath-consistent framework. I also aim to retrieve the near-surface velocity model that reproduces the derived near-surface corrections.

Each chapter of this thesis contains the intermediate tasks that I completed to develop and demonstrate my approach for dealing with S-wave near-surface corrections.

Chapter 2 deals with the problem of non-stationarity of the near-surface corrections. Based on Snell's Law, I quantify the deviations of the S-wave raypaths from the nearly-vertical assumption given a range of velocity contrasts and structural conditions. Here, I challenge the convenience of using a surface-consistent framework for addressing S-wave near-surface effects. Instead, a raypath-consistent framework is proposed.

Chapter 3 introduces the principles of plane-wave interferometry as defined by Tao and Sen (2013). As an extension, I then introduce the mathematical formulation for a convolution-type interferometry in the plane-wave domain. I explain how these concepts can be used to capture and remove near-surface effects from converted-wave data. I then evaluate the performance of this process under different transformations. First, I study the τ-p transform and then I show its relationship with the radial trace transform (Claerbout, 1985). The Snell's ray transform (Ottolini, 1982) is also considered in this chapter. Finally, I apply near-surface corrections in each one of these domains and explain the benefits and limitations of each of then.

Chapter 4 contains an extension of the processing work-flow introduced by Henley (2012) to the τ-p domain and its application on two converted-wave field datasets. The first dataset displays moderate near-surface effects in a smoothly varying geological structure. The second one presents very large near-surface effects in a flat geological setting. The particularities of the processing work-flow for each dataset are presented. Results are evaluated in terms of improvements in coherency and stacking power of the events observed in common-receiver and common-conversion-point stacked sections.

Chapter 5 presents the mathematical framework to perform an inversion for S-wave near-surface velocities using τ-differences between receiver stations. Sensitivities for each one of the model parameters are derived and a quasi-Newton inversion approach is framed. I then test this inversion using both noisy synthetic data and field data.

Chapter 6 contains the conclusions of this thesis and draws some lines for future work.

The contents of chapters 2 and 4 have been published in Cova et al. (2017). The content of chapter 5 was accepted for publication in Cova et al. (In press 2017).

Chapter 2

Raypath-consistent near-surface corrections

In the processing of PS converted-wave data, S-wave static corrections are needed for the receiver side. Static effects are usually addressed using a surface-consistent approach. This implies that a constant correction is to be applied to all the data recorded at the same receiver location. This is a result of the assumption that a large velocity change exists between the near-surface and the medium underneath, which produces nearly-vertical raypaths. Even though this assumption works in most cases for the processing of P-wave data it does not necessarily hold for S-waves. The reason for this is that P-wave and S-wave velocities are not affected to the same magnitude by changes in rock properties. Therefore, the ability to reach wider raypath angles in the near-surface combined with the very low velocity of S-waves magnifies the effect of the near-surface on the data.

In this chapter, I show how the delays introduced by the presence of very low S-wave velocities in the near-surface result in non-stationary effects that are raypath-dependent. I also show that the magnitudes of these delays can be larger than what can be considered a residual static. Arguments for developing a raypath-consistent solution in contrast to a surface-consistent solution are presented here.

2.1 Angle-dependent near-surface traveltimes

Most traditional approaches for finding statics solutions rely on the assumption of nearly-vertical raypaths in the near-surface. However, the low velocity of S-waves magnifies the delays in traveltime produced by the inevitable violation of this assumption by the real near-surface.

Based on Snell's Law, it is possible to compute the transmission angle of a wavefield propagating through the near-surface layer. In equation 2.1, the transmission angle into the near-surface layer (θ_0), of an upcoming wavefield with incident angle (θ_1) depends on the

velocity ratio between the media.

$$\sin\theta_0 = \frac{v_0}{v_1}\sin\theta_1, \tag{2.1}$$

where v_0 is the velocity in the near-surface layer and v_1 the velocity in the medium underneath.

When $v_0 \ll v_1$, the ratio $v_0/v_1 \approx 0$, and regardless of the magnitude of the incidence angle θ_1 the transmission angle θ_0 will be close to zero. This is the basic condition which supports the assumption of vertical raypaths through the near-surface. However, S-wave velocity variations with depth may occur more gradually than those for P-waves. P-wave velocities are dependent upon the bulk modulus of the rock and the presence of fluids, which generally causes a rapid velocity increase with depth, whereas S-wave velocities depend on neither the bulk modulus nor the fluid content and generally increase more slowly with depth (Yilmaz, 2015).

Angle-dependent traveltimes in the near-surface can be computed as,

$$t(\theta) = \frac{z}{v_0\cos\theta_0}, \tag{2.2}$$

where z is the depth of the near-surface base at the receiver location. Combining equations 2.1 and 2.2, I compute the maximum expected transmission angle for a range of velocity ratios v_0/v_1 from 0 to 1 and their deviation from the vertical traveltime ($\theta_0 = 0°$). I assumed an upcoming ray with an incidence angle of 60° at the base of the near-surface layer. Results for a near-surface layer with a thickness of 100 m and a velocity of 500 m/s are shown in Figure 2.1. There, velocity ratios less than 0.35 produce deviations from the vertical traveltime that are less than 10 ms. However, for ratios greater than 0.48, near-surface delays can be larger than 20 ms and may reach more than 100 ms if the velocity of the near-surface is close to the velocity of the underlying medium ($v_0/v_1 > 0.85$). In this case, transmission angles could reach magnitudes larger than 48°. Hence, gradual velocity changes in the near-surface will produce time delays significantly different from those assuming vertical raypaths.

An additional degree of complexity can be introduced if the base of the near-surface layer is considered to have some dip. In this case, the deviation from the vertical raypath assumption is controlled not only by the velocity ratio but also by the dip of the base of this layer. Figure 2.2 shows the geometry of the problem.

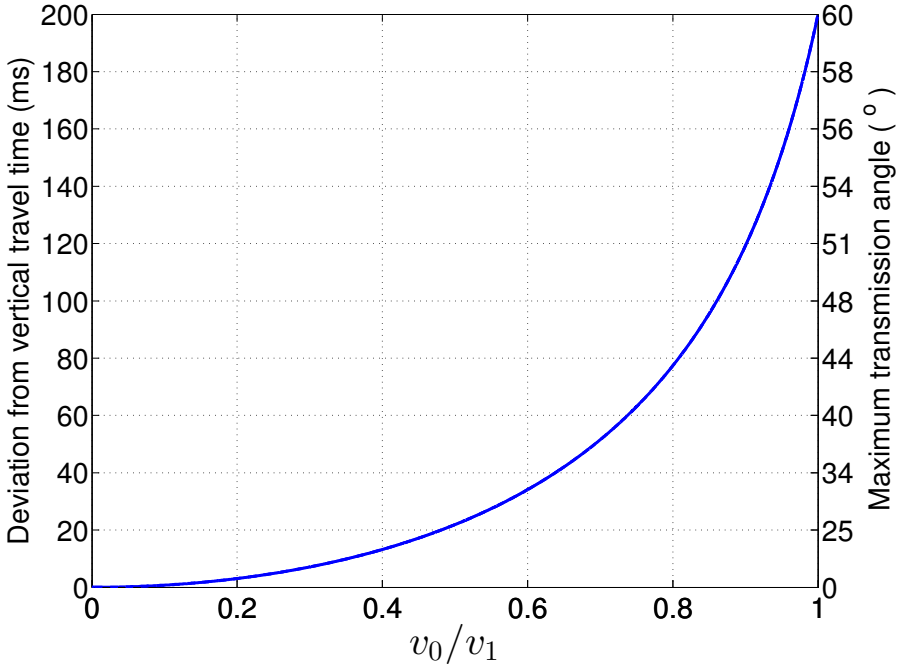

Figure 2.1: Deviation from vertical traveltime and maximum raypath angle in the near-surface as a function of the velocity contrast between the near-surface (v_0) and the medium underneath (v_1). A near-surface layer with velocity v_0=500 m/s and 100 m thickness is assumed. The incidence angle at the base of the near-surface was fixed at 60°. For velocity ratios greater than 0.48, deviations are larger than 20 ms. Raypath-dependent corrections will be needed to account for this difference.

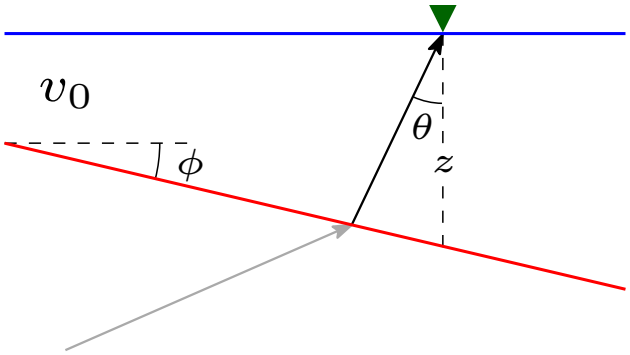

Figure 2.2: Geometry used for computing raypath-dependent traveltimes for a dipping near–surface layer in a 2D medium. Here, z is the vertical thickness at the receiver location, θ is the raypath angle, ϕ is the dip angle at the base of the near-surface and v_0 is the velocity of the near-surface layer.

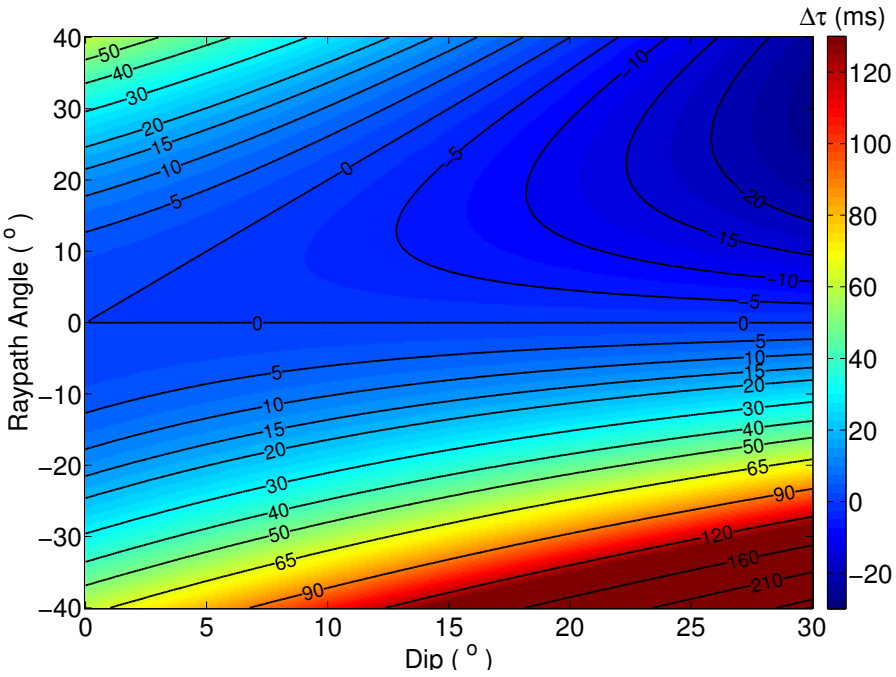

Figure 2.3: Expected deviation from the vertical raypath assumption when changes of the dip of the near-surface layer and transmission raypath angles are considered. Even for small dips ($\sim 5°$) deviations of more than 20 ms can be observed if raypath angles are larger than 20°. Ray-path angles are measured clockwise respect to the normal to the recording surface.

The near-surface traveltime along the ray depicted in Figure 2.2 is given by

$$t(\theta) = \frac{z}{v_0} \frac{\cos\phi}{\cos(\theta - \phi)}. \tag{2.3}$$

where ϕ is the dip angle of the base of the near-surface. In Figure 2.3 one can see the combined effect of the dip at the base of the near-surface and the variation of the raypath angles on the computation of traveltimes, as predicted by equation 2.3. Notice the asymmetry in the time delays around the raypath angle. Traveltimes recorded at a fixed receiver location will be affected differently depending on the transmission angle into the near-surface. For a small dip of 5°, the deviation from the vertical traveltime condition amounts to 20 ms and 43 ms for raypath angles of 30° and -30°, respectively. As the dip increases, larger deviations can occur with smaller raypath angles. Under this condition, a single constant correction for all the traces recorded at a fixed receiver location will not be enough to properly remove the near-surface time delays. A traveltime correction that changes with the raypath angle is required for this purpose.

Additionally, depending on the depth at which the P-S mode conversion occurs, events will arrive at the near-surface with wider or smaller raypath angles. Therefore, shallower events that are more likely to reach wider conversion angles will need larger corrections than those produced at large depths. Thus, the effect is no longer a "static" problem, but a non-stationary correction problem. These issues need to be addressed to properly correct for the near-surface effect.

2.2 Data analysis in the rayparameter domain

The rayparameter "p", when measured from data recorded with surface arrays, is related to the emerging angle of the wavefield at the surface (Tatham, 1989). This feature makes the rayparameter domain a good candidate for characterizing near-surface effects. According to Snell's Law, the rayparameter p is a constant quantity when the propagation of the wavefield occurs in horizontally layered media. The conservation of the horizontal slowness can be applied to the propagation of converted waves. For the PS raypath depicted in Figure 2.4 one may write

$$p = \frac{\sin\theta_{p,i}}{v_{p,i}} = \frac{\sin\theta_{s,i}}{v_{s,i}}, \tag{2.4}$$

where $v_{p,i}$ and $v_{s,i}$ are the P- and the S-wave velocities in the $i-th$ layer and $\theta_{p,i}$ and $\theta_{s,i}$ are the P- and S-wave propagation angles. This expression allows us to characterize the full raypath of a converted wave by using a single rayparameter value, despite the difference in velocity between the P- and S-wave legs.

To transform the data to the rayparameter domain, the "slant-stack" or τ-p transform can be applied (Claerbout, 1975; Stoffa, 1989). The transformation is achieved by stacking data along straight lines within a given range of slopes (p) and intercept times (τ). Equation 2.5 shows the integral definition of the τ-p transform acting on the x-t domain,

$$\tilde{u}(\tau, p) = \int_{-\infty}^{\infty} u(\tau + px, x)dx. \tag{2.5}$$

Since seismic reflection arrivals exhibit near-hyperbolic moveout, the τ-p transform amounts to scanning for all the possible tangents that define such hyperbolas. The "scanning" character of the transform relieves it from needing any *a priori* knowledge of the velocity model of the subsurface.

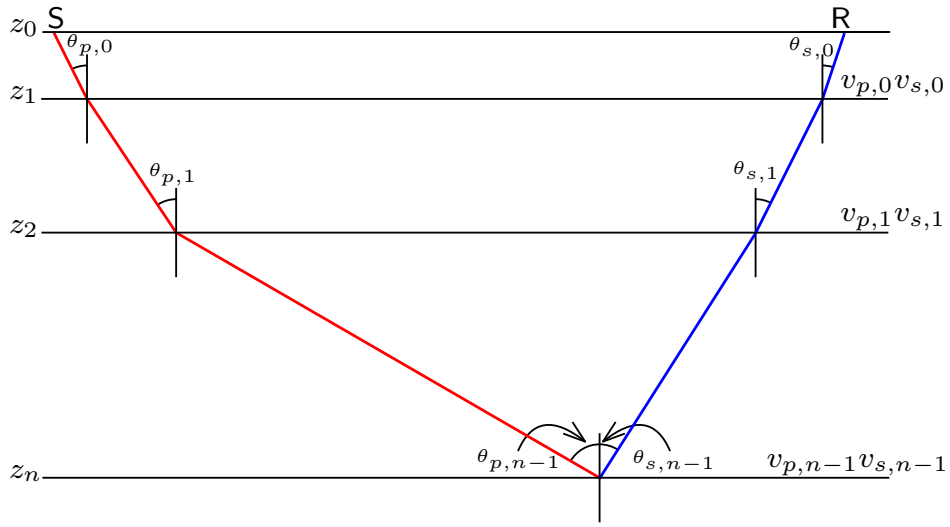

Figure 2.4: Schematic representation of a PS-raypath. Despite the asymmetry in the raypath the rayparameter p is constant in horizontally layered media.

The inverse τ-p transform can be defined as,

$$u(t,x) = -\frac{1}{2\pi}\int_{-\infty}^{\infty} \tilde{u}^{\dagger}(t-px,p)dp. \tag{2.6}$$

where $\tilde{u}^{\dagger}(\tau,p)$ is the derivative of the Hilbert transform of $\tilde{u}(\tau,p)$ (Chapman, 1978). The transform pair defined in equations 2.5 and 2.6 is often used for plane wave decomposition since $\tilde{u}(\tau,p)$ represents the plane-wave response of a laterally homogeneous model to a line source. Hence, it is very useful for studying two dimensional wave propagation in a model with variation in one dimension.

2.3 Raypath-consistent near-surface corrections

In a layered medium, the intercept time τ represents the aggregate vertical slowness-thickness product in equation 2.7 (Bessonova et al., 1974; Diebold and Stoffa, 1981; Hake, 1986):

$$\tau = \sum_{i=0}^{n-1} \Delta z_i \left(q_i^d + q_i^u\right) = \tau^d + \tau^u, \tag{2.7}$$

where q_i is the vertical slowness $q_i = \cos(\theta_i)/v_i$ in the i-th layer and Δz_i is the layer thickness $\Delta z_i = z_{i+1} - z_i$. The superscripts ^{d} and ^{u} denote the downgoing and upgoing legs of the raypath in Figure 2.4, respectively. For PS-waves, the downgoing vertical slowness is controlled by P-wave velocities and the upgoing by S-wave velocities.

To understand the effect of the near-surface on the receiver side I isolate and expand the upgoing contribution to the intercept time τ,

$$\tau^u = \sum_{i=2}^{n-1} \Delta z_i q_i^u + (z_2 - z_1)\, q_1^u + (z_1 - z_0)\, q_0^u. \tag{2.8}$$

Assuming the measurement surface z_0 is at depth $z_0 = 0$ m and re-arranging terms yields

$$\tau^u = \sum_{i=2}^{n-1} \Delta z_i q_i^u + z_2 q_1^u + z_1 \left(q_0^u - q_1^u\right). \tag{2.9}$$

The first term in equation 2.9 gives the total upgoing τ-contribution from the conversion point up to the base of the second layer. The second term represents the contribution from the base of the second layer up to the surface with velocity v_1 and raypath angle θ_1, as if the layer with velocity v_0 where not present in the model. The effect of the near-surface layer with velocity v_0 and thickness z_1 is contained in the last term. Therefore, to remove the near-surface effect amounts to isolating and subtracting this term from the total intercept time. The receiver-side near-surface correction can then be written as

$$\Delta\tau^u = z_1 \left(q_1^u - q_0^u\right). \tag{2.10}$$

Notice that in the correction term in equation 2.10, the τ contribution of the near-surface layer ($z_1 q_0$) is removed and replaced by the τ contribution obtained with the rayparameter controlling the propagation in medium 1. Therefore, under this raypath-consistent framework, near-surface corrections are obtained by first replacing the near-surface layer velocity with the velocity of the lower medium (i.e., the replacement medium), and second, by extending the raypath parameters of the lower medium up to the surface.

The vertical slowness q is related to the rayparameter value by

$$q_i^2 + p_i^2 = \frac{1}{v_i^2}, \tag{2.11}$$

hence, the receiver-side near-surface correction for the intercept times can be parametrized in term of p-values as

$$\Delta\tau^u = z_1 \left(\sqrt{\frac{1}{v_{s,1}^2} - p^2} - \sqrt{\frac{1}{v_{s,0}^2} - p^2} \right). \tag{2.12}$$

Since the rayparameter value is constant in a horizontally layered medium, equation 2.12 shows that the delays introduced by the near-surface and elevation variations are constant for a fixed p-value.

To illustrate this idea, I performed PS raytracing over the velocity models in Figure 2.5. Note that there is no P-wave velocity contrast in the near-surface layer. This simulates a situation in which source-side near-surface corrections have already been applied. Figure 2.5a depicts a model with a low near-surface S-wave velocity layer. Removing the near-surface layer and replacing it with the velocity of the medium underneath results in the velocity model represented in Figure 2.5b. The resulting PS-traveltimes from the surface to the interfaces at 200 m and 1000 m depth are plotted in time-offset (Figure 2.6a) and τ-p (Figure 2.6b) coordinates. I then subtracted the traveltimes with and without the near-surface low velocity layer for each event to understand the corrections needed to remove the near-surface traveltimes in each domain (Figure 2.6c and d).

From Figure 2.6c it is evident that the corrections needed to remove the time delays produced by the near-surface in the time-offset domain are non-stationary. The magnitude of the corrections not only changes with offset but also depends on the depth of the event. This is a result of the raypath-dependent character of the correction. For a fixed offset, energy arriving from deep interfaces will present raypath angles closer to the vertical. However, for the same offset, a shallow interface will produce energy that will be transmitted into the near-surface with a wider raypath angle. For this reason shallow events will need corrections with larger magnitudes than deeper events.

Figure 2.6d confirms that in the τ-p domain the correction needed to remove the near-surface time delays is the same for both events. For a fixed rayparameter value, a constant τ correction will suffice to remove the delays caused by the near-surface on both events. By simply moving the data from the space-time to the τ-p domain a problem that was originally non-stationary can be dealt with as an actual static problem.

2.3.1 Dipping near-surface layer

For dipping interfaces, equation 2.7 still holds (Diebold and Stoffa, 1981). However, the rayparameter value p is no longer constant, and its computation requires us to consider the

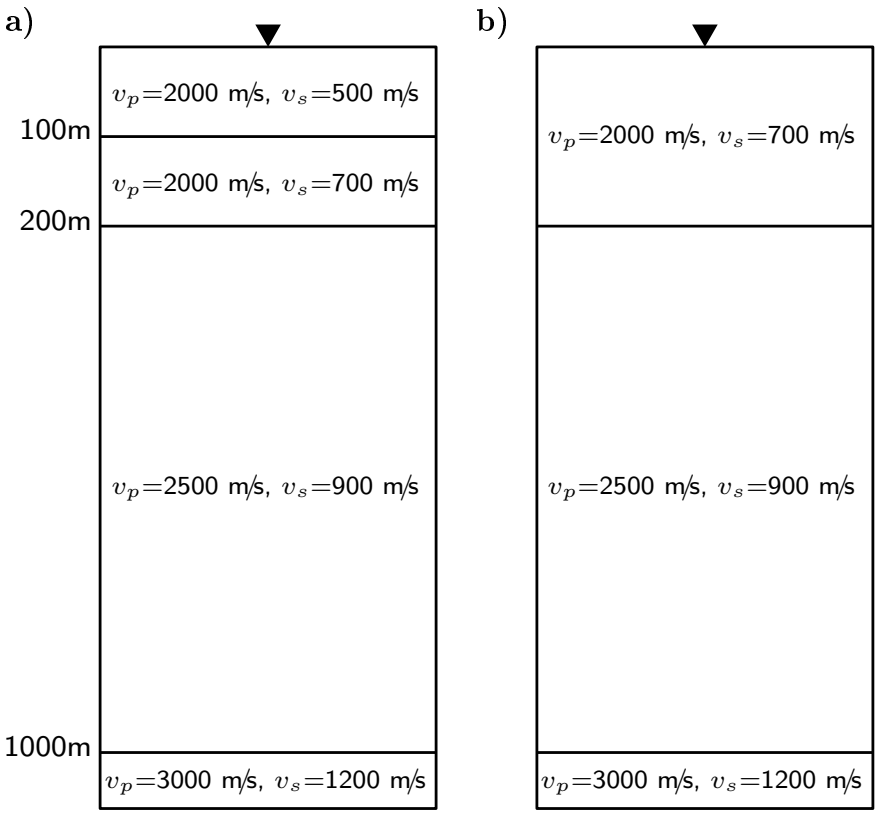

Figure 2.5: Subsurface velocity models (a) with a low S-wave velocity layer at the near-surface and (b) without a low velocity layer. No P-wave velocity contrast was included in the near-surface to simulate the case where source-side statics have already been corrected.

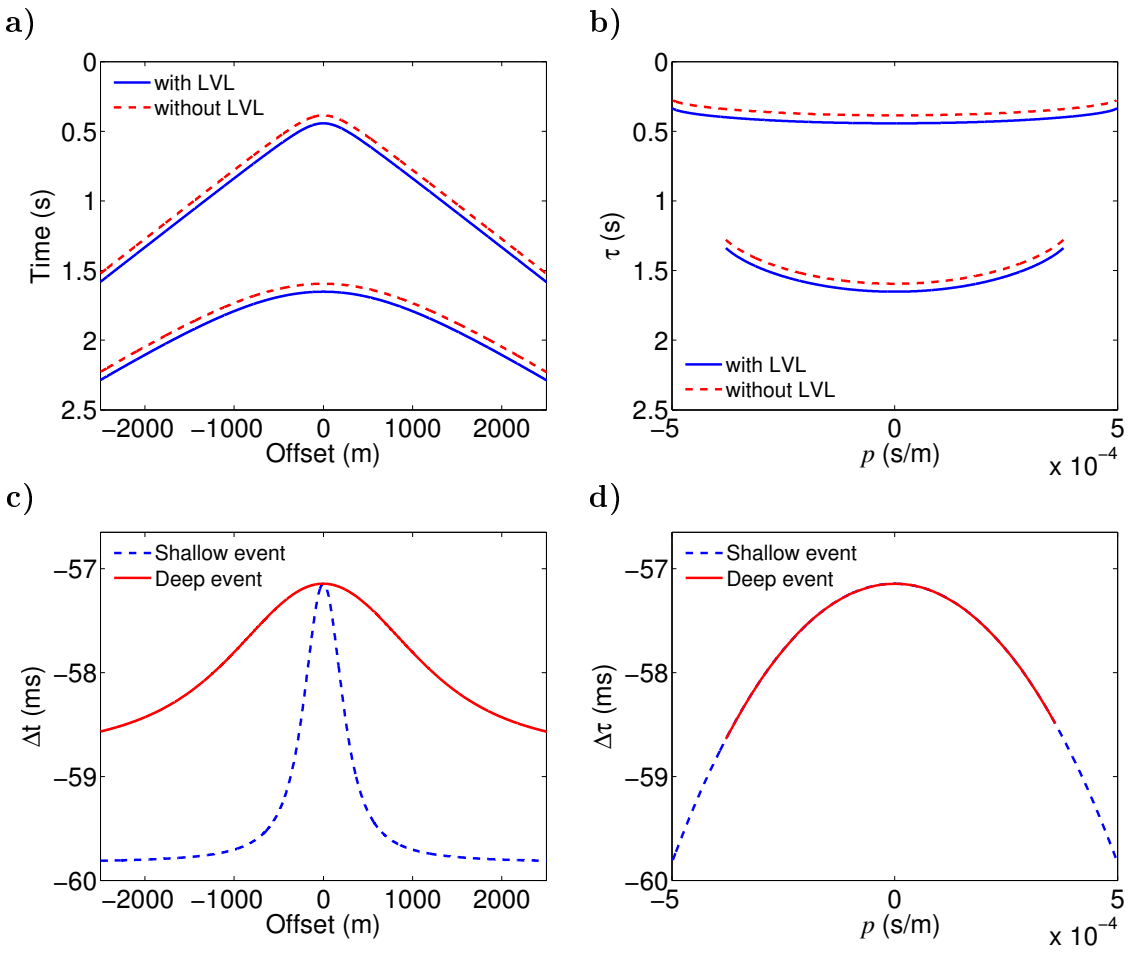

Figure 2.6: Traveltimes with and without a low velocity layer (LVL) at the near-surface in (a) time-offset and (b) τ-p domain. The events correspond to the PS-traveltimes to the interfaces at 200 m and 1000 m depth in Figure 2.5. The difference between these traveltimes for each event are plotted in (c) and (d) for each domain. Notice that in the τ-p domain the same correction can be applied to both events to simulate the traveltimes without a low velocity layer present at the near-surface.

dip of each interface.

By reciprocity, the traveltimes of the events in a PS-mode receiver gather are equivalent to those in an SP-mode source gather (Thomsen, 1999). Assuming that the effect of the near-surface on the P-wave leg has been removed and that the rest of the interfaces are flat, the vertical slowness at the base of the replacement medium can be computed as,

$$q_1^u = \left(\frac{1}{v_{s,1}^2} - p^2\right)^{1/2}. \tag{2.13}$$

The apparent slowness (p_a) along the base of the near-surface layer is

$$p_a = p\cos\phi - q_1\sin\phi. \tag{2.14}$$

This is the result of projecting the horizontal and vertical slownesses in the medium 1 along the interface with dip angle ϕ.

Invoking Snell's Law, the slownesses measured parallel to the interface should be equal on both media ($p_{a,1} = p_{a,0} = p_a$). To compute the vertical slowness in the near-surface layer a second projection must be performed. This time the slownesses measured along the interface defined by the base of the near-surface layer are projected along the plane defined by the surface. As a result

$$q_0^u = \left(\frac{1}{v_{s,0}^2} - p_a^2\right)^{1/2}\cos\phi - p_a\sin\phi. \tag{2.15}$$

Equations 2.13 and 2.15 can be used to compute the vertical slownesses needed to obtain the near-surface correction in equation 2.10. Because the correction is still raypath-consistent, a constant correction will remove the near-surface effect from all the events even if the base of the near-surface is dipping.

Next, the model in Figure 2.7 was used to ray-trace converted-wave traveltimes using a dipping near-surface layer. These traveltimes were compared with the ones obtained from the model in which no low velocity layer is present at the near-surface (Figure 2.5b), in both time-offset (Figure 2.8a) and τ-p (Figure 2.8b) domains. The traveltime differences for each event are plotted in Figure 2.8c and 2.8d. Notice that the raypath dependency of the correction has been magnified. Since the vertical thickness beneath the receiver location is 65 m, the magnitude of the corrections are smaller than in Figure 2.6. However, the range

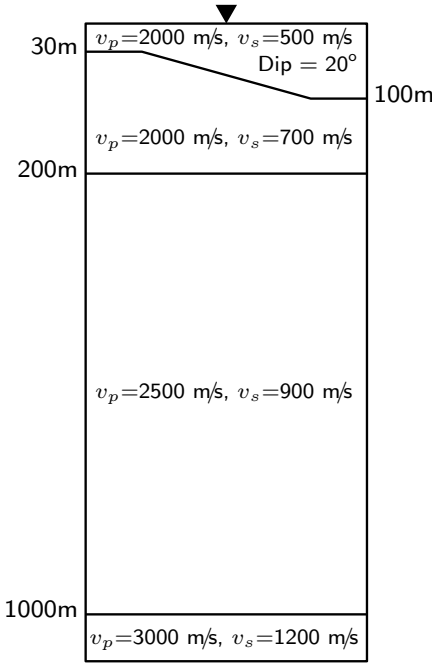

Figure 2.7: Velocity model used for ray tracing converted-wave traveltimes to a fixed receiver location with a locally dipping near-surface layer. The vertical thickness of the near-surface layer beneath the receiver location is 65 m with a dip of 20°.

of the corrections is now larger and asymmetric. For the shallow event, negative offsets will need a correction of about 43 ms while positive offsets will require a correction of 36 ms. The difference on the corrections for the shallow and deep events confirms the non-stationarity of the problem in the time-offset domain. However, the results in the τ-p domain still exhibit robust stationarity.

Figure 2.9 displays the correction values for dip angles between 0° and 45°. Notice that as the dip angle increases, the range of the corrections needed to remove the effect of the near-surface increases. For the model used here, the value of the correction, assuming vertical traveltimes in the near-surface, should be 37 ms. As the dip increases the deviation of the corrections from the vertical traveltime condition may reach magnitudes larger than 20 ms. As a result, using a constant shift for all the traces will not remove the near-surface time delays completely, particularly for energy propagating with large rayparameter values.

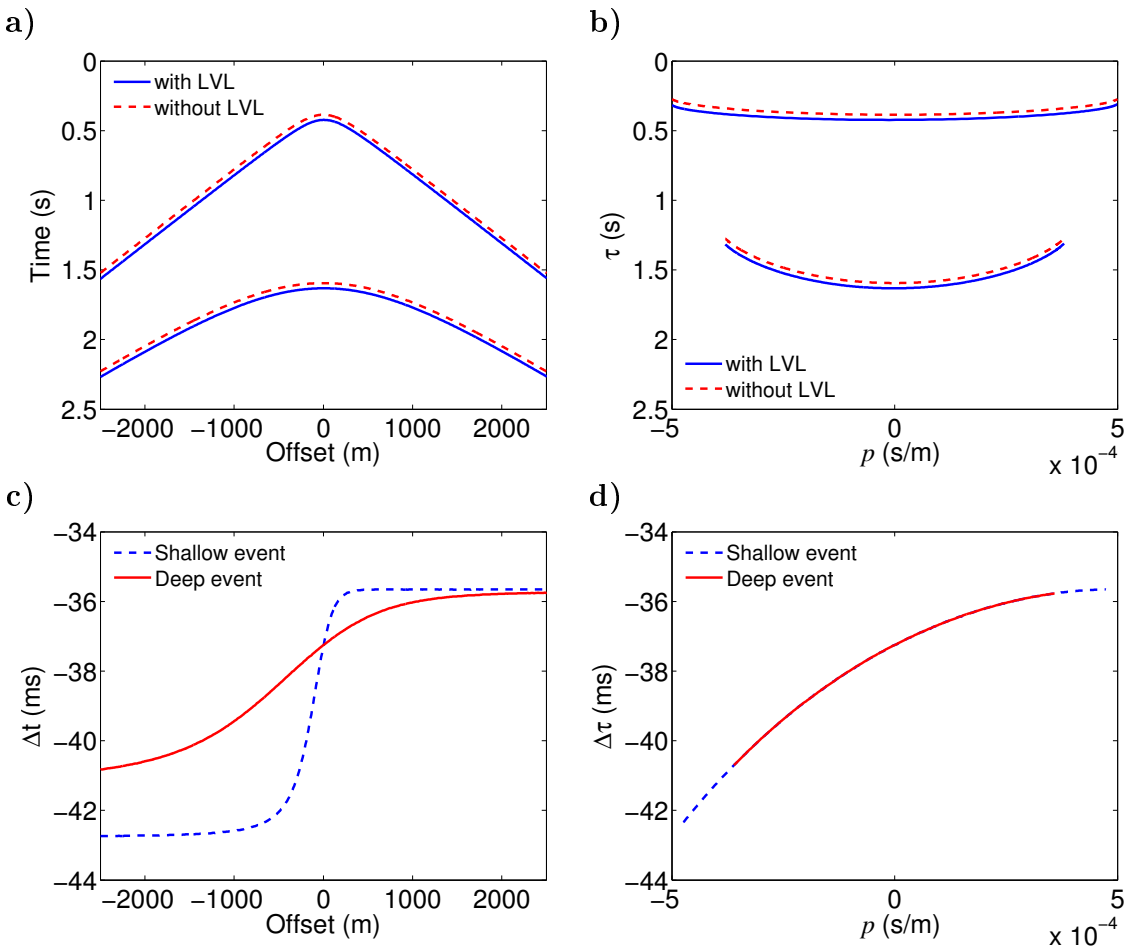

Figure 2.8: Traveltimes with and without a dipping near-surface layer in (a) time-offset and (b) τ-p domain. The differences between these traveltimes for each event are plotted in (c) and (d) for each domain. Notice that in the τ-p domain the same correction can be applied to both events to simulate the traveltimes without a dipping low velocity layer present at the near-surface.

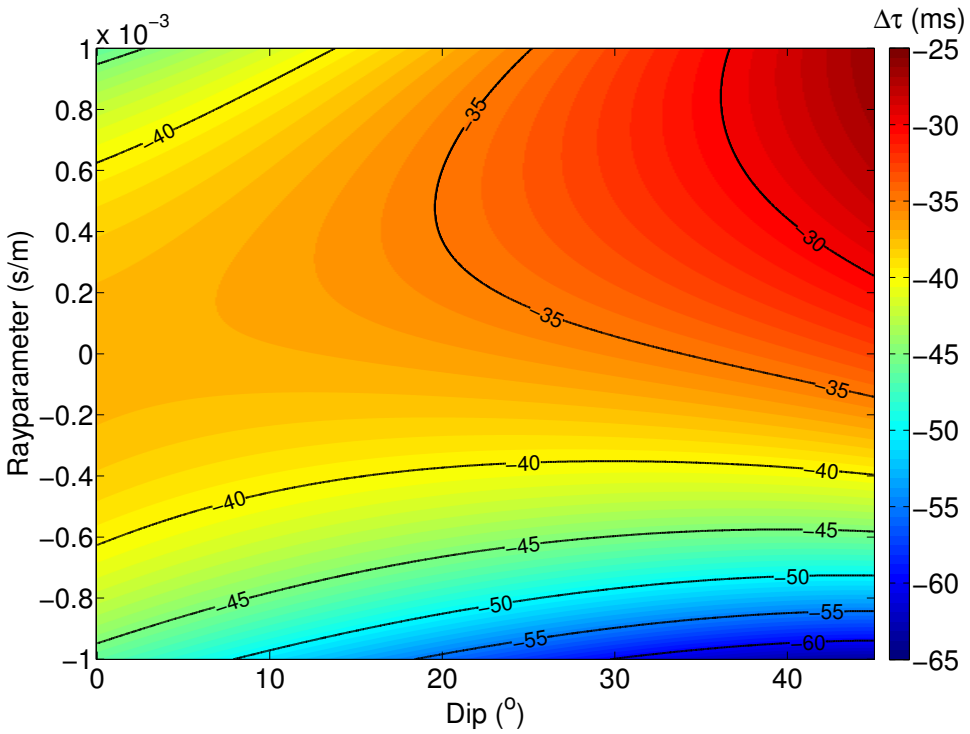

Figure 2.9: Near-surface corrections for various dip angles at the base of the near-surface layer. Thickness beneath the receiver location is fixed at 65 m, the S-wave velocity of the near-surface layer is 500 m/s and the replacement velocity is 700 m/s.

2.4 Remarks

Ray trace modeling of PS raypaths showed how variations in the transmission angle through the near-surface layer can introduce significant additional delays. Dips in the near-surface layer can deviate the raypaths even more and change the magnitude of the delays depending on the direction of propagation. This leads to a non-stationary effect that needs to be addressed in a raypath-consistent framework. Wavefronts produced at different depths can arrive at the base of the near-surface layer, with dissimilar angles, also leading to different near-surface corrections.

I showed that the raypath-consistent solution responds well when the near-surface layer has some structural complexity that may lead to non-stationary statics. When velocities are structurally complex, the non-stationary character of the near-surface delays becomes more significant and a raypath-consistent solution is required to account for the complex kinematics through the near-surface.

Chapter 3

Raypath-domain interferometry

Near-surface traveltime corrections are usually computed from the analysis of critically-refracted waves. However, in the acquisition of multicomponent data, using compressional sources, such data are usually not available or are buried by surface-wave noise. In this chapter, I show how near-surface corrections can be extracted by using interferometric principles on converted-wave data. Since I wish to operate on a raypath-consistent framework, I first introduce the concepts of interferometry in the rayparameter domain.

I also explore different options for moving the data to a raypath-consistent framework. As explained in the previous chapter, this is required to address the non-stationarity of the near-surface effects. The τ-p, radial trace (RT) and Snell's trace (ST) transforms are considered here. The approximations, benefits and limitations of each one of them are explained.

3.1 Interferometry in the plane-wave domain

Plane wave interferometry uses the τ-p transform or "slant-stack" transform to compute the ray parameter values (p) present in the data (Claerbout, 1975; Stoffa, 1989). In the space-time (x-t) domain, the τ-p transform stacks data along straight lines given by the equation $t = \tau + px$, where τ is the intercept time and x is the offset. In the frequency domain, the τ-p transformation is achieved by phase-shifts followed by summation in the space coordinate. Equation 3.1 shows the expression for transforming a source gather into the ω-p domain.

$$\hat{D}(x_s|p_r,\omega) = \int D(x_s|x_r,\omega)e^{i\omega p_r x_r}dx_r, \tag{3.1}$$

where $D(x_s|x_r,\omega)$ is the recorded data in the frequency domain, x_s is the source position, x_r is the receiver position, p_r is the receiver ray parameter, and $\hat{D}(x_s|p_r,\omega)$ is the transformed plane-wave gather from the original shot gather.

The inverse τ-p transform is given by,

$$D(x_s|x_r,\omega) = \omega^2 \int \hat{D}(x_s|p_r,\omega)e^{-i\omega p_r x_r}dp_r. \tag{3.2}$$

For a receiver gather the same equations hold, but integration is performed over the shot position coordinate (x_s) and shot-ray-parameter values (p_s).

Seismic interferometry as introduced by Wapenaar (2004) and Schuster (2009) is based on the crosscorrelation of frequency domain data and integration over the location coordinates in order to retrieve or redatum data at different spatial locations. Equation 3.3 shows the so called reciprocity equation of the correlation type after assuming far field conditions and ignoring amplitude effects.

$$Im\left[D(x_B|x_A,\omega)\right] \approx \int D(x|x_A,\omega)D(x|x_B,\omega)^* dx. \tag{3.3}$$

Tao and Sen (2013) introduced the concept of rayparameter interferometry. Here I summarize their derivation of the reciprocity equation of the crosscorrelation type in the rayparameter domain.

From equation 3.2 the complex conjugate of the data at the x_B location can be written as,

$$D(x|x_B,\omega)^* = \omega^2 \int \hat{D}(x_B|p,\omega)^* e^{i\omega px} dp. \tag{3.4}$$

Substituting equation 3.4 into equation 3.3 results in,

$$Im\left[D(x_B|x_A,\omega)\right] \approx \omega^2 \int\int D(x|x_A,\omega)\hat{D}(x_B|p,\omega)^* e^{i\omega px} dp dx. \tag{3.5}$$

Rearranging equation 3.5 one may write

$$Im\left[D(x_B|x_A,\omega)\right] \approx \omega^2 \int \hat{D}(x_B|p,\omega)^* dp \int D(x|x_A,\omega)e^{i\omega px} dx. \tag{3.6}$$

Notice that the rightmost integral is the forward τ-p transform (equation 3.1) of the data at location A. Therefore, equation 3.6 gives,

$$Im\left[D(x_B|x_A,\omega)\right] \approx \omega^2 \int \hat{D}(x_B|p,\omega)^* \hat{D}(x_A|p,\omega) dp. \tag{3.7}$$

Equation 3.7 suggests that, similar to how a crosscorrelation and sum over trace locations allows us to cancel out shared raypaths, in the τ-p domain this can be achieved by crosscorrelation and summation over rayparameter values. Figure 3.1 depicts this idea. Since the direct ray from the source location S* to the receiver location A has the same ray parameter as the event S*AOB, the traveltimes along the shared raypath are canceled out by the crosscorrelation. The output is a trace whose source appears to be at location A and whose receiver is located at B.

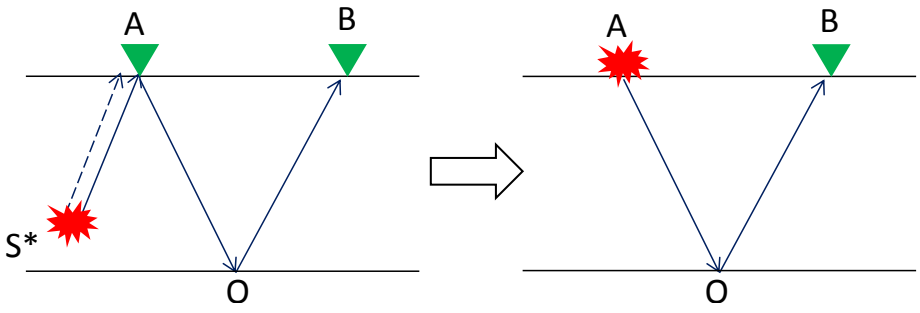

Figure 3.1: Sketch showing how the crosscorrelation of the direct arrival from the stationary source position S* with the raypath S*AOB cancels out the shared raypath S*A retrieving the traveltime as if the source had been in at the location A. In the τ-p domain this cancellation is possible since the raypaths share the same rayparameter.

3.1.1 Convolution-type interferometry in the plane-wave domain

To complete the set of reciprocity equations in the rayparameter domain, I now derive the reciprocity equation of the convolution type. I start by writing the normalized version of the convolution-type reciprocity equation in the space domain (Schuster, 2009; Wapenaar et al., 2011),

$$D(x_B|x_A,\omega) \approx \int D(x|x_A,\omega)D(x|x_B,\omega)dx. \tag{3.8}$$

Note that instead of multiplication with a complex conjugate, in the convolution-type interferometry a simple multiplication must be performed. As a result, the phases of the functions inside the integral are summed producing a new function with longer traveltimes.

Replacing the functions inside equation 3.8 by their inverse τ-p transforms gives

$$D(x_B|x_A,\omega) \approx \int \left[\omega^2 \int \hat{D}(x_A|p,\omega)e^{-i\omega px}dp\right]\left[\omega^2 \int \hat{D}(x_B|p',\omega)e^{-i\omega p' x}dp'\right]dx, \tag{3.9}$$

Changing integration orders and adding the phases,

$$D(x_B|x_A,\omega) \approx \int\int \omega^4 \hat{D}(x_A|p,\omega)\hat{D}(x_B|p',\omega)dpdp' \int e^{-ix\omega(p'+p)}dx, \tag{3.10}$$

The rightmost integral can be identified as a scaled delta function. Hence, equation 3.10 becomes,

$$D(x_B|x_A,\omega) \approx \int\int \omega^4 \hat{D}(x_A|p,\omega)\hat{D}(x_B|p',\omega)\left[\frac{2\pi}{\omega}\delta(p'+p)\right]dpdp', \tag{3.11}$$

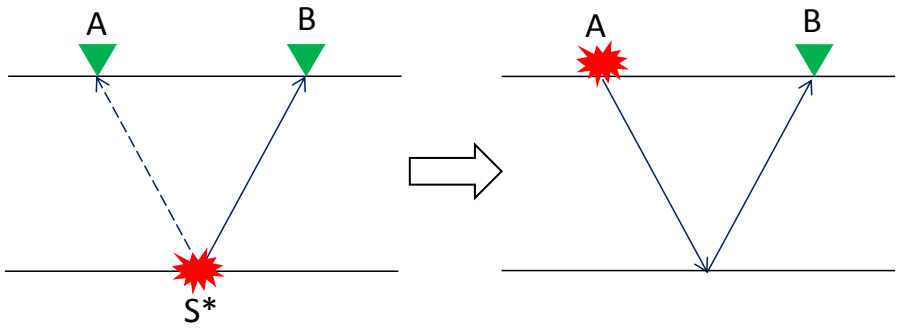

Figure 3.2: Sketch showing how the addition of the traveltimes from the source location S* to receivers A and B, leads to the two way traveltime as if the source had been in location A. Since the convolution happens between rays with the same rayparameter but in opposite directions the resulting raypath is symmetric as in a pure-P or pure-S-wave reflections.

Using the sifting property of the delta function after integrating over p',

$$D(x_B|x_A,\omega) \approx 2\pi\omega^3 \int \hat{D}(x_A|p,\omega)\hat{D}(x_B|-p,\omega)dp. \tag{3.12}$$

The operation expressed in Equation 3.12 is depicted in Figure 3.2. There, the traveltimes along two raypaths with the same rayparameter value but pointing in opposite directions are added yielding the two-way traveltime of a reflection-like event.

3.1.2 Rayparameter domain corrections

In my data-driven approach for removing near-surface effects, I use crosscorrelation and convolution operations to add and subtract traveltimes along raypaths. In contrast to full waveform interferometry, I do not seek to reconstruct the data, but just to remove the effect of the traveltimes in the near-surface. To illustrate this process, I computed synthetic PS-traces using the velocity models in Figure 3.3. My goal is to remove the effect of the near-surface layer in Figure 3.3a to produce the traveltime that would have been recorded under the subsurface conditions represented in Figure 3.3b.

The synthetic receiver gathers obtained with each velocity model are shown in Figure 3.4. Notice that no amplitude effects were included in the modelling. I then transform both datasets to the τ-p domain and crosscorrelate them, as shown in Figure 3.5.

The crosscorrelation functions in Figure 3.5c capture the differences between the models with and without a near-surface layer. Then, to remove the near-surface effect from the data

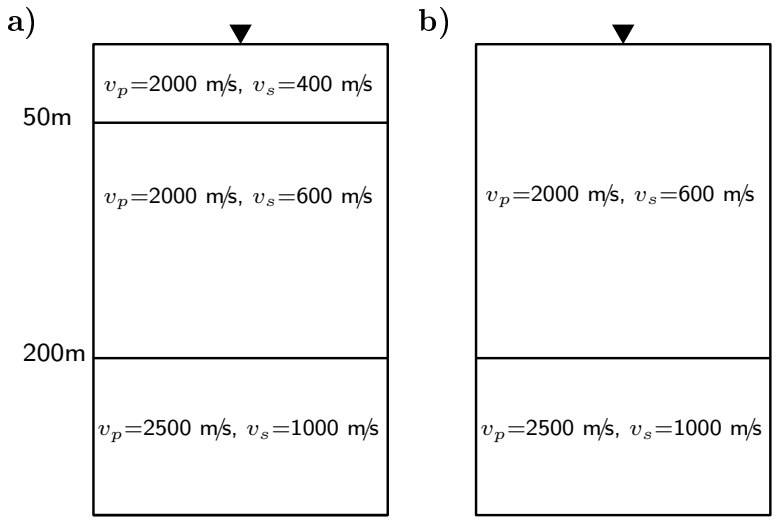

Figure 3.3: (a) Velocity model including a low S-wave velocity layer in the near-surface. (b) Velocity model after replacing the near-surface layer with a medium with the same velocity as the second layer.

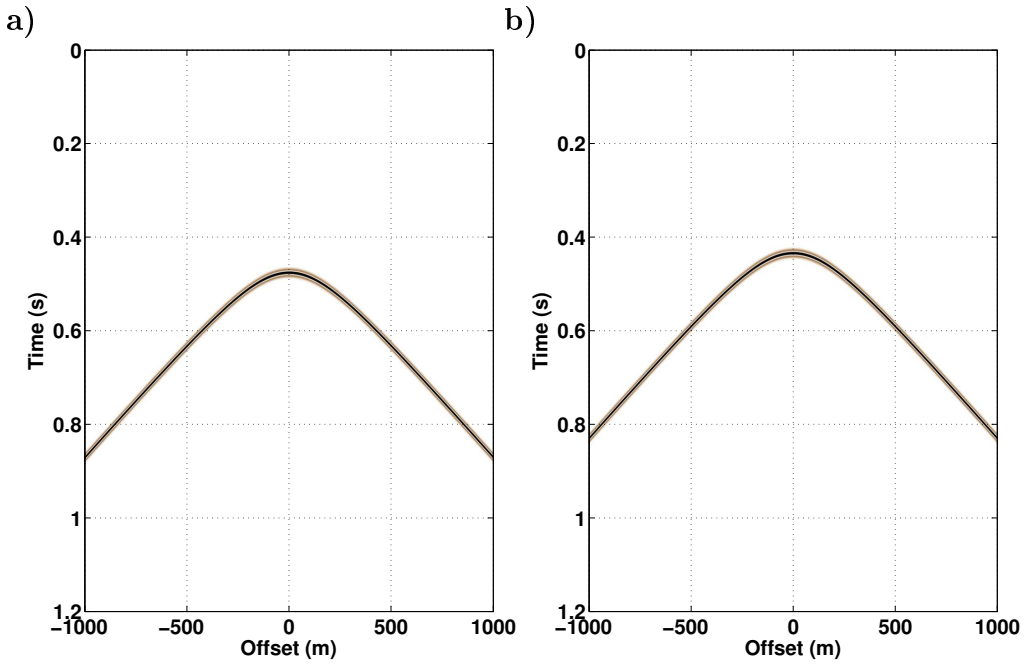

Figure 3.4: a) Raytraced converted-wave events using the velocity models in (a) Figure 3.3a and (b) Figure 3.3b. No amplitude effects were included in the modelling. Notice that traveltimes in (a) are larger than those in (b) due to the presence of the low S-wave velocity layer in the near-surface. No reflections from the base of the near-surface were modelled since they usually are not distinguishable in field data.

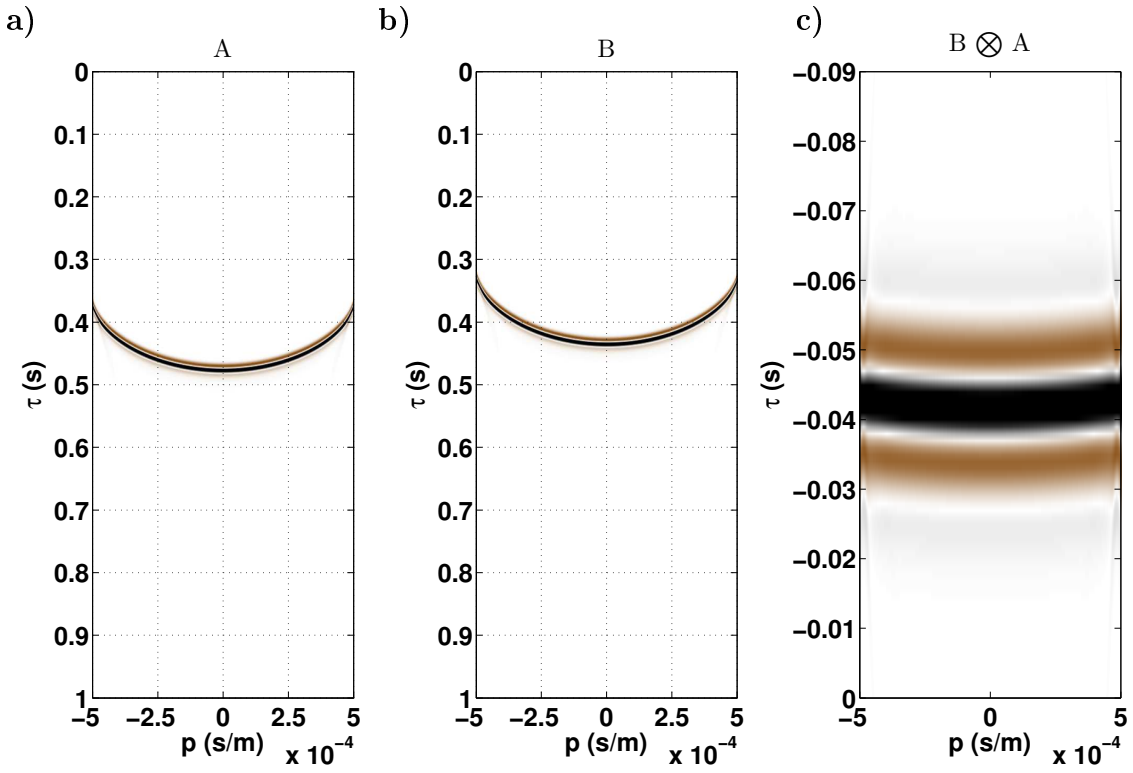

Figure 3.5: τ-p representation of the data (a) with and (b) without near-surface effects. (c) Crosscorrelation between both datasets.

in 3.4a, I use the crosscorrelation functions in 3.5c as matching filters. The output is shown in Figure 3.6a. These data represent the corrected receiver gather in τ-p domain. After applying an inverse τ-p transform the corrected data in the x-t domain is recovered (Figure 3.6b).

Figure 3.7 displays a comparison of the traveltimes picked from the modelled and corrected data. There, one can see how the traveltimes obtained from the corrected data match the data modelled without the near-surface layer.

The process illustrated above is an idealised representation of how the interferometric near-surface corrections should work in the rayparameter domain. Two important features are important to consider. First, the character of the data without near-surface effects was assumed to be known. In a real case, one will need to create "model" traces that will represent the data without near-surface effects. This will be addressed in the following chapter. Second, this example does not deal with non-stationary effects, since only one event was modelled. In

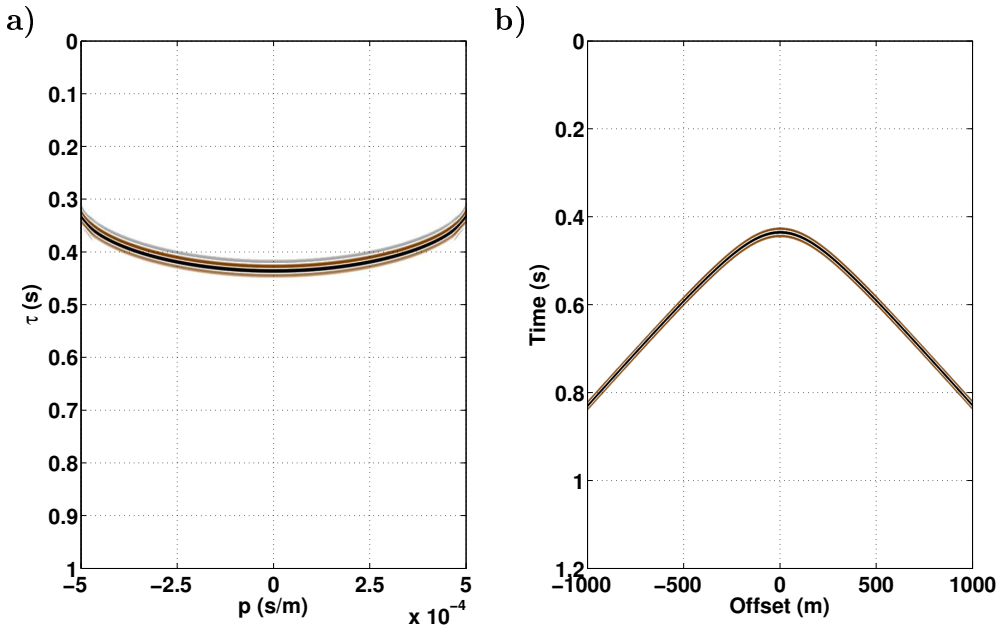

Figure 3.6: (a) Data obtained after convolving the initial data that includes near-surface effects (Figure 3.5a) and the crosscorrelation functions in Figure 3.5c. (b) Back-transformation of these data to the space-time domain. Since the crosscorrelation functions are band-limited they filter part of the spectrum of the original data resulting in broader waveforms in (a) and (b).

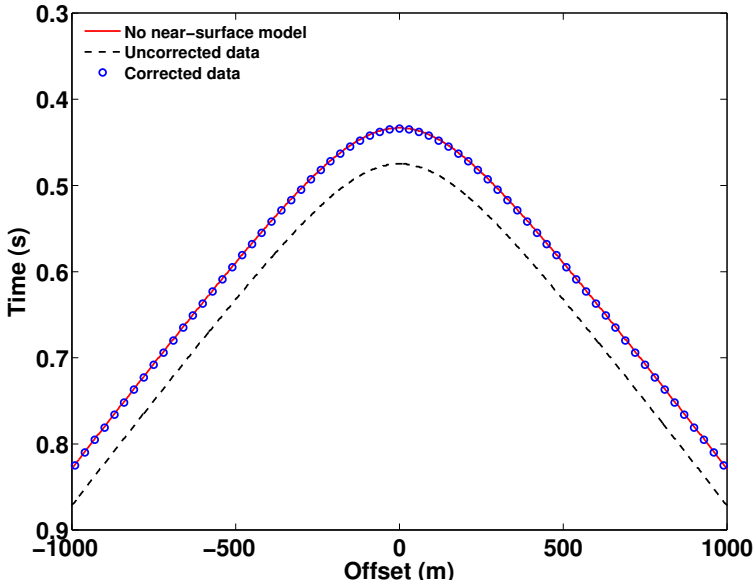

Figure 3.7: Traveltimes picked from the modelled data without near-surface effects (continuous lines) compared with the traveltimes picked from the uncorrected (dashed line) and corrected (circles) seismic gathers. The corrected traveltimes match the modelled traveltimes without a near-surface layer.

this regard, the next section will explore three different approximations for moving the data to a raypath-consistent framework. They will be judged based on their ability to properly handle non-stationary effects.

3.2 Alternatives to the τ-p transform

3.2.1 The radial trace transform

The radial trace transform consists of a deformation of the time-space domain into a radial domain via the expression,

$$u'(t,r) = u(t,rt) \tag{3.13}$$

where r is the radial-trace parameter defined as $r = x/t$ (Claerbout, 1985).

Since the RT-transform involves just a remapping of amplitude values, it can be rewritten using the sifting property of the delta function as,

$$u'(t,r) = \int_{-\infty}^{\infty} u(t,x)\delta(x-rt)dx \tag{3.14}$$

From equation 3.14 one can see that the effect of the RT-transform is that of resampling the amplitudes recorded in the x-t domain along lines of constant slope. All the amplitudes gathered along each one of the lines form a new radial trace.

Figure 3.8 shows the geometrical construction of the RT-transform. There, one can note that the RT-transform seems to be related to the τ-p transform in the following way: First, the RT transform operates along lines that intersect the coordinate system at a fixed location. Having a constant intersection with the time axis is equivalent to having a fixed τ value (usually τ=0) in the τ-p transform. Secondly, the slope of the trajectories in the RT-transform is $1/r$ while in the τ-p transform it is p, so, for a constant velocity medium the radial trace parameter can be seen as the reciprocal of the rayparameter. Lastly, since the RT-transform involves just a remapping of the amplitudes as defined by equation 3.13, amplitudes never get stacked. Thus, the RT-transform can be seen as the gathering of all the data needed to compute the amplitudes along a constant τ value in the τ-p domain. To show this let us evaluate equation 2.5 for $\tau = 0$ and rewrite it using the sifting property of the delta function,

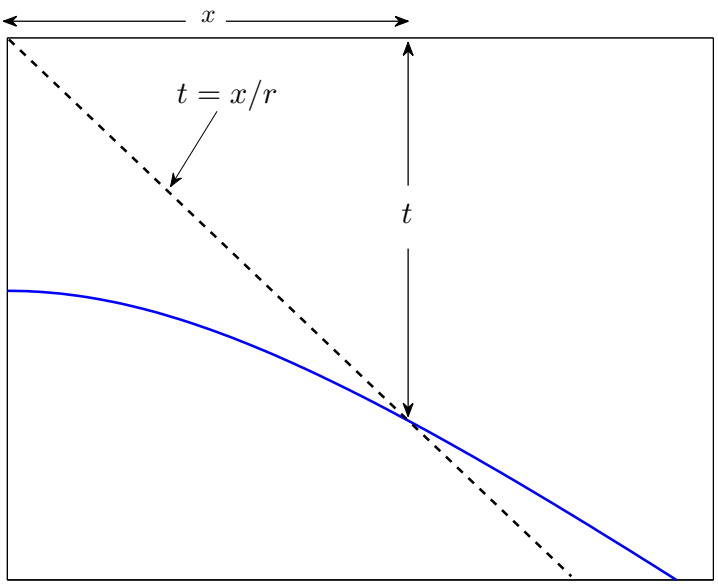

Figure 3.8: Representation of the RT transform. Amplitudes along the line $t = x/r$ are gathered to from a new trace in the RT domain.

$$\tilde{u}(0,p) = \int_{-\infty}^{\infty} u(px,x)dx, \tag{3.15}$$

$$= \int_{-\infty}^{\infty}\int_{-\infty}^{\infty} u(t,x)\delta(t-px)dtdx. \tag{3.16}$$

Using the scaling property of the delta function and changing the order of the terms inside of it yields,

$$\tilde{u}(0,p) = \frac{1}{|p|}\int_{-\infty}^{\infty}\int_{-\infty}^{\infty} u(t,x)\delta\left(x-\frac{t}{p}\right)dtdx, \tag{3.17}$$

$$= |r|\int_{-\infty}^{\infty}\int_{-\infty}^{\infty} u(t,x)\delta\left(x-rt\right)dtdx, \tag{3.18}$$

$$= |r|\int_{-\infty}^{\infty} u(t,rt)dt, \tag{3.19}$$

$$= |r|\int_{-\infty}^{\infty} u'(t,r)dt \tag{3.20}$$

Equation 3.20 shows that a radial-trace gather contains all the amplitudes to be stacked for computing the data at a constant τ value in a τ-p gather. To complete the τ-p construction, one will need to compute additional RT gathers where the time-axis intercept assumes

each possible value in succession, from 0 to the maximum traveltime. Then, gathering all the traces with the same $1/r$ value, but associated with each of the different intercepts, and stacking them, will provide a trace equivalent to a constant p trace in the τ-p domain.

Despite the simplicity and cheap computational cost of the RT transform, it may not be appropriate when strong velocity changes are present in the data. In this case a transform able to gather amplitudes along nonlinear trajectories may be needed. Figure 3.9 shows an example of a synthetic gather and its RT-transform. There, it is possible to compare the straight line trajectories used for the RT-transform to gather the amplitude values versus the curved trajectories used in the Snell trace transform. The latter will be described in the next section.

3.2.2 The Snell trace transform

The Snell trace transform can be seen as a generalization of the RT-transform for a flat-layered medium with depth varying velocities (Ottolini, 1982). In contrast to the RT transform, the ST transform gathers the amplitudes along curved trajectories in x-t space. The most important feature is that those trajectories are intended to follow Snell's Law. In so doing the ST transform attempts to remap each event so that projected rays follow the velocity changes in the subsurface.

The moveout of reflection events can be approximated by the equation,

$$t = \left(t_0^2 + \frac{x^2}{v_{rms}(t)^2} \right)^{1/2}. \tag{3.21}$$

Following the definition of the rayparameter,

$$p = \frac{dt}{dx} = \frac{1}{2} \left(t_0^2 + \frac{x^2}{v_{rms}(t)^2} \right)^{-1/2} \frac{2x}{v_{rms}(t)^2} \tag{3.22}$$

$$= \frac{x}{v_{rms}(t)^2 t}. \tag{3.23}$$

By following equation 3.23 the Snell trace transform tries to extract from the x-t domain the amplitudes that were recorded with the same rayparameter value. If the true velocity model is unknown, the sampling trajectories can be updated by assuming a constant linear increment as proposed by Henley (2000). In figure 3.9 one can see the curved trajectories used in the ST transform and the resulting gathers.

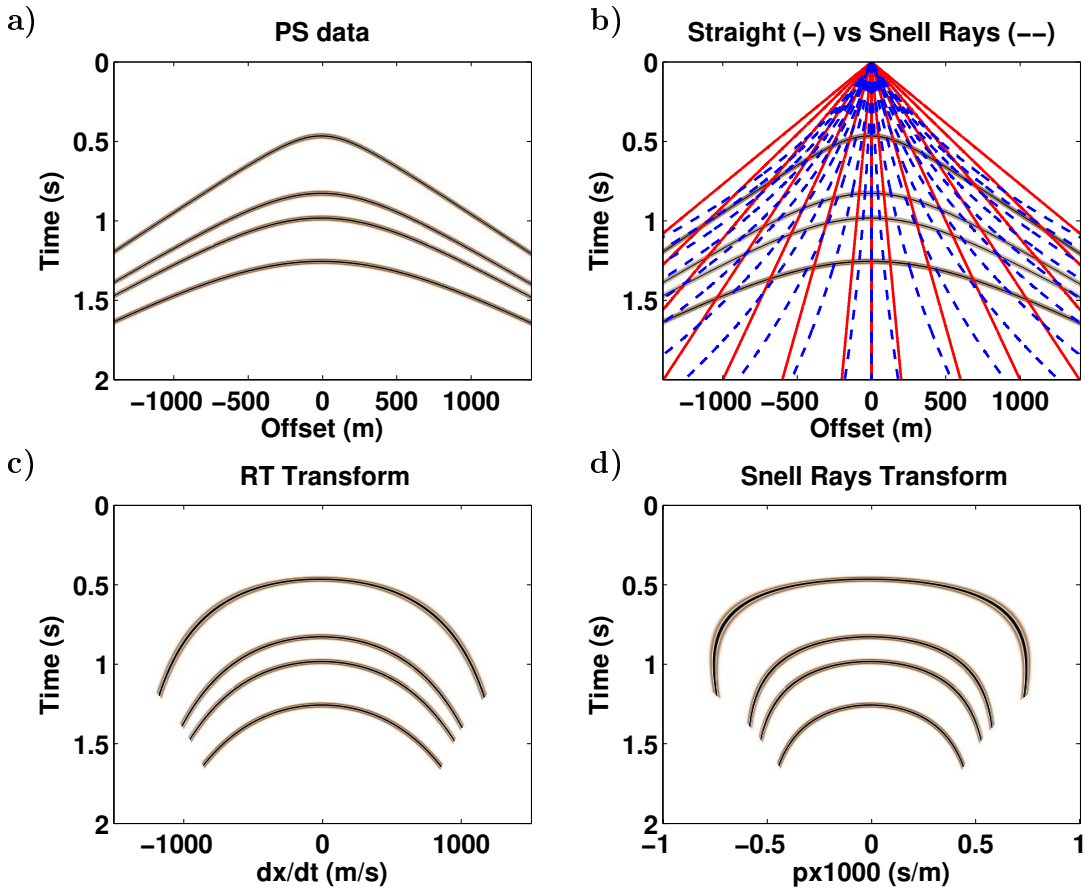

Figure 3.9: (a) Synthetic shot gather. (b) RT and ST mapping trajectories. (c) Input data transformed to the RT domain. (d) Input data transformed to the ST domain.

Although more accommodating of velocity variations than the RT transform, the ST transform still needs some a priori information about the velocity model in order to properly gather amplitudes recorded with the same rayparameter value. Its strength is its very simple inversion and very cheap computational cost.

In the following sections the application of τ-p, RT and ST transforms to synthetic data will be performed in order to compare the performance of each of them in the solution of raypath-dependent statics.

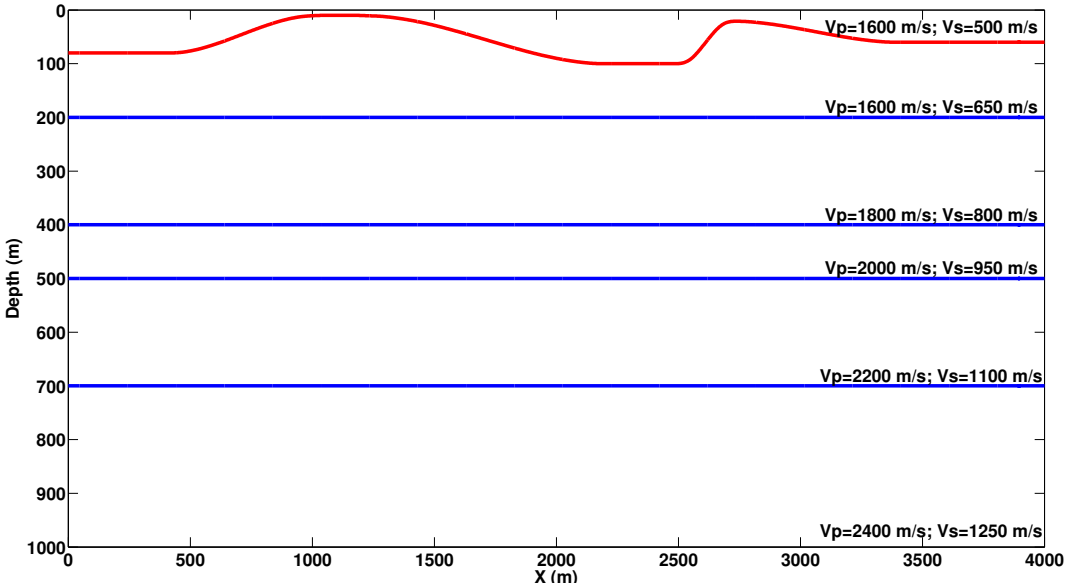

Figure 3.10: Velocity model used for computing synthetic data.

3.3 Synthetic data analysis

Figure 3.10 shows the velocity model used to compute converted-wave synthetic traces via ray-tracing using the software Omni. The low velocity layer (LVL) at the top shows thicknesses ranging between 20 m and 100 m and has an S-wave velocity of 500 m/s. No P-wave velocity contrast was included between the LVL and the underlying layer in order to bypass P-wave statics. Both the S-wave and P-wave velocities increase monotonically with depth in order to study the effect of these changes on each one of the transforms explained above.

Figure 3.11 displays the source and receiver gathers obtained at the location x= 3000 m in the model. The source gather in Figure 3.11a displays significant near-surface effects. Since the reflecting interfaces are flat one should not expect this type of deformation. Therefore, such deformations are the footprint of the geometry of the near-surface on the moveout of the events. In contrast, on the receiver gather on Figure 3.11b no near-surface effects are evident. Since no P-wave velocity contrast was included between the near-surface layer and the layer underneath no source-side statics are produced.

Due to the asymmetry of PS raypaths, for a fixed source-receiver pair the location of the conversion point varies with depth. I used the asymptothic approximation to the conversion

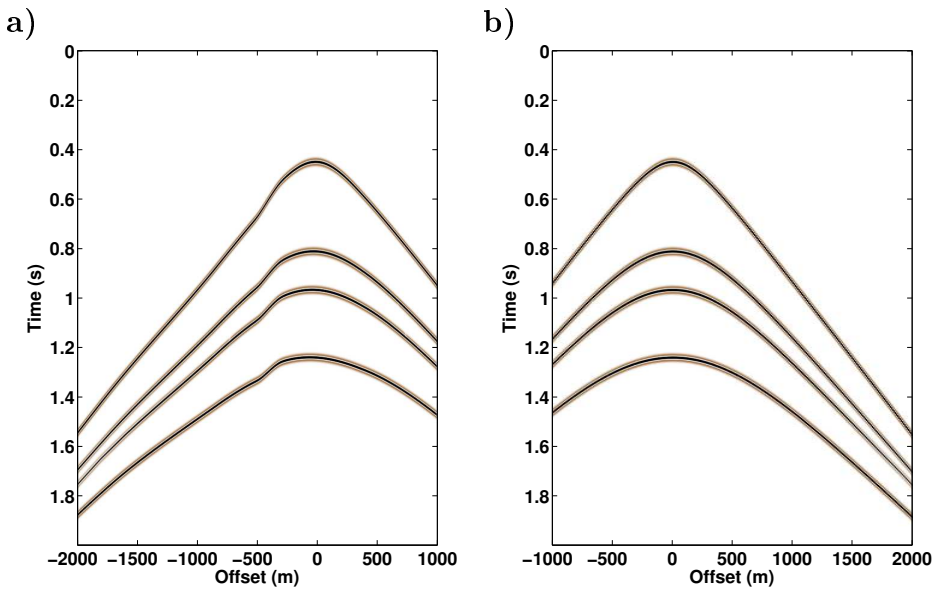

Figure 3.11: (a) Source and (b) receiver gathers obtained at the location x = 3000 m in Figure 3.10. No amplitude information was included in the modelling. Notice how the moveout of the events in the source gather are deformed due to the near-surface geometry. Since no P-wave velocity changes were included in the near-surface the receiver gather does not show any deformation.

point introduced by Fromm et al. (1985) to form ACP (asymptotic conversion point) gathers. Figure 3.12 shows the raw ACP stack before applying any correction. In this section the effect of the S-wave velocities in the near-surface is very clear. Even though the interfaces in the model are flat, the stacked section shows deformed interfaces that mimic the geometry of the near-surface layer.

To understand the stationarity of the S-wave delays produced by the LVL I gathered the data into receiver gathers and apply the RT, ST, and τ-p transforms. Figure 3.13 shows trace panels where data with a common parameter for all the receiver locations are displayed. For example, in the common-offset panel all the traces recorded with an offset of 1500 m at each receiver location are extracted and plotted according to their location. The other three panels follow the same concept, but samples are selected according to the parameter that controls each one of the transforms.

To test each one of these domains for stationarity I picked the first event and flattened the data around that event. If the deformations produced by the near-surface are of the

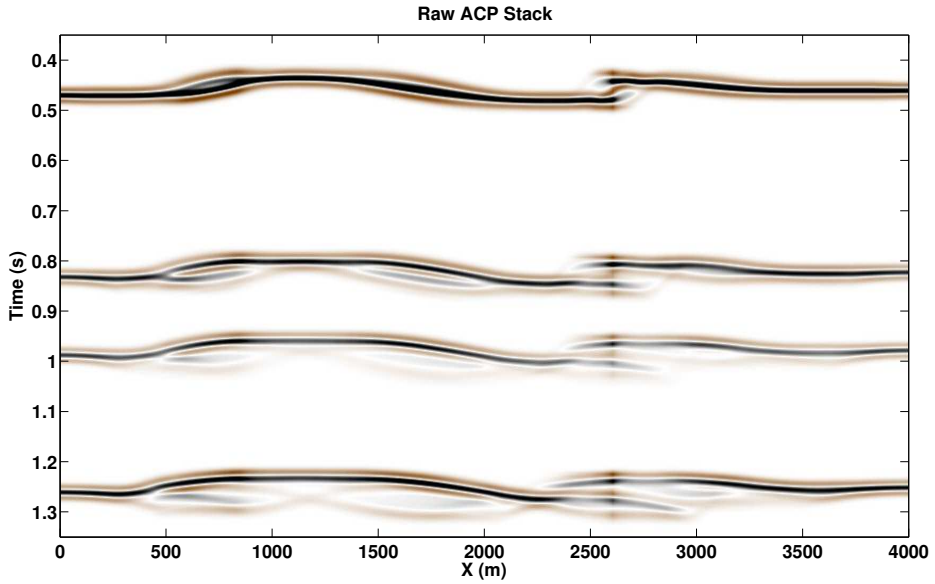

Figure 3.12: ACP stack before static corrections. Notice the imprint of the geometry of the near-surface on the events.

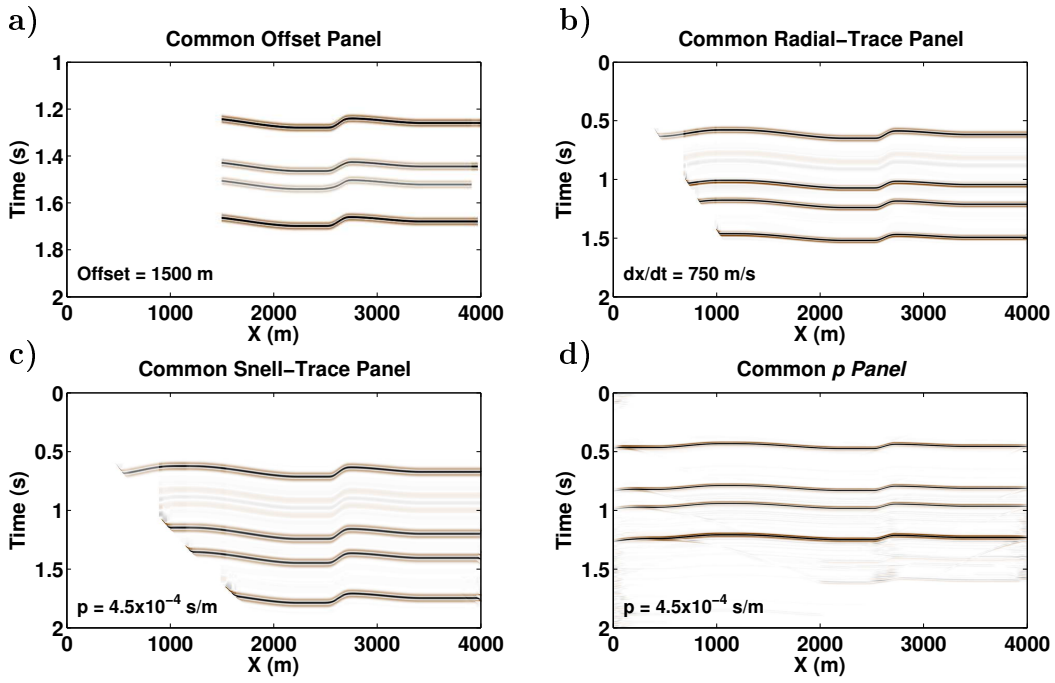

Figure 3.13: Raw data gathered in different domains. (a) Common offset domain. (b) Radial trace domain. (c) Snell trace domain. (d) τ-p domain.

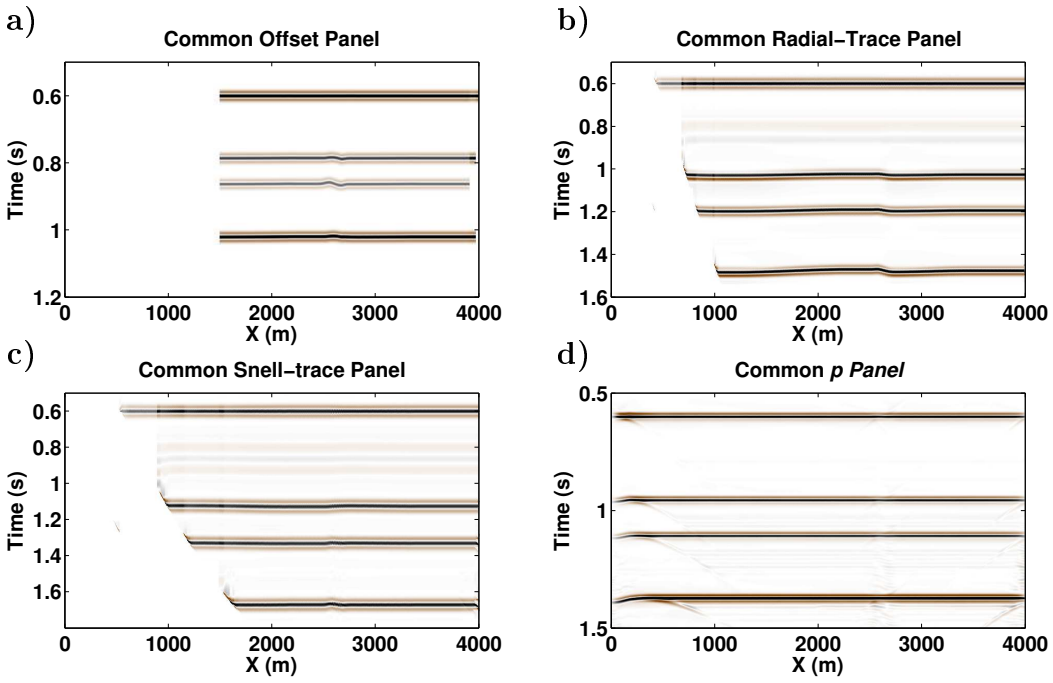

Figure 3.14: Results after flattening the data with respect to the shallowest event. (a) Common offset domain. (b) Radial trace domain. (c) Snell trace domain. (d) τ-p domain.

same magnitude for all the events, then removing the deformation from one of them should correct the deformations on the rest of the reflectors. Figure 3.14 shows the result of this test. There, it is possible to see how, after flattening the shallow event, there is still a residual deformation on the common-offset, RT and ST panels, particularly around x = 2600 m. Only in the τ-p panel was the non-stationary character of the statics fully compensated. In other words, the τ-p transform was able to move the data to a fully stationary condition. This is in agreement with the analysis presented in Chapter 2, where I show that, the near-surface effect at a fixed receiver location is constant for all the events recorded with the same p-value.

Finally, figure 3.15 shows the resulting ACP stacks after removing the static effect in each domain. The result in the common-offset domain shows unsolved static problems for the four events, specifically around x=2600 m. This problem is likely the result of using the picks of a single common-offset panel to remove the statics from all the dataset. The RT transform produces high quality statics corrections for the three first events. However, for the deepest event the wavelet seems deformed (figure 3.16). This may be a result of stacking wavelets that are not properly aligned, leading to a decrease of the seismic resolution. One

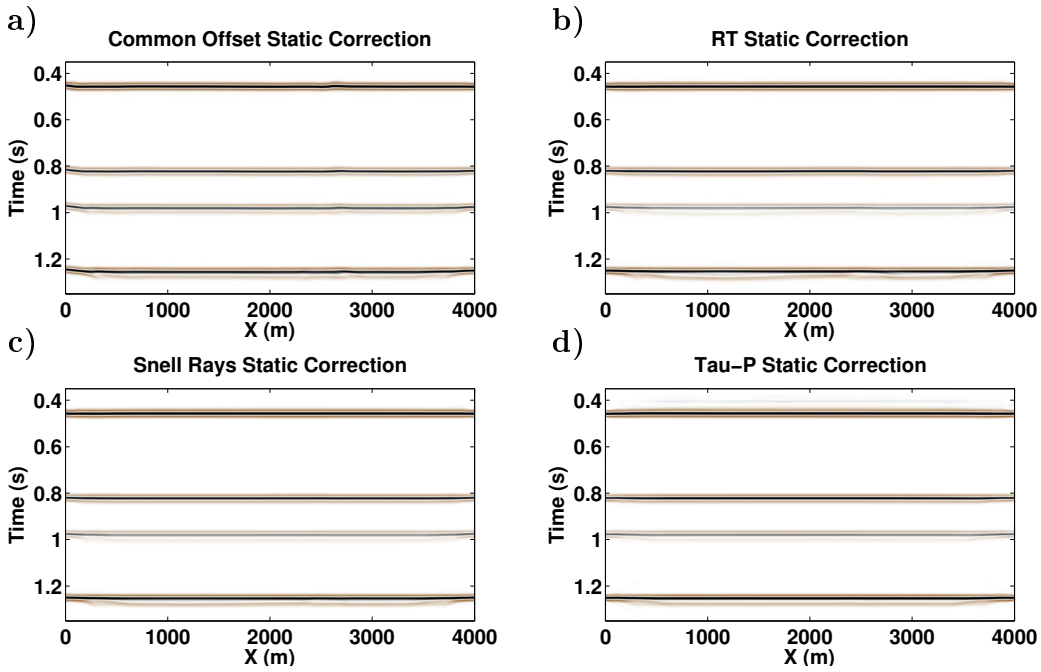

Figure 3.15: ACP stacks after removing the statics in each raypath sensitive domain. (a) Common offset domain. (b) Radial trace domain. (c) Snell trace domain. (d) τ-p domain.

can also observe the presence of edge effects due to the limited range of offsets, slopes and p-values for the deep reflector toward the ends of the line. The stacks after removing the statics in the Snell-ray and τ-p domains are very similar. There are very small differences in the coherence of the deepest event where the τ-p solution seems to have worked slightly better. However, this result also shows small artifacts in the shallowest part of the section. The Snell-ray transform, although being a "cleaner" solution, requires some knowledge or assumptions about the velocities in the subsurface.

3.4 Remarks

Addition and subtraction of traveltimes along raypaths can be achieved by using interferometric operations in the rayparameter domain. These operations allow us to capture and remove near-surface effects from converted-wave data.

Transformation of the data from x-t to a raypath-consistent framework is required to properly handle the non-stationary character of the near-surface problem. The three different

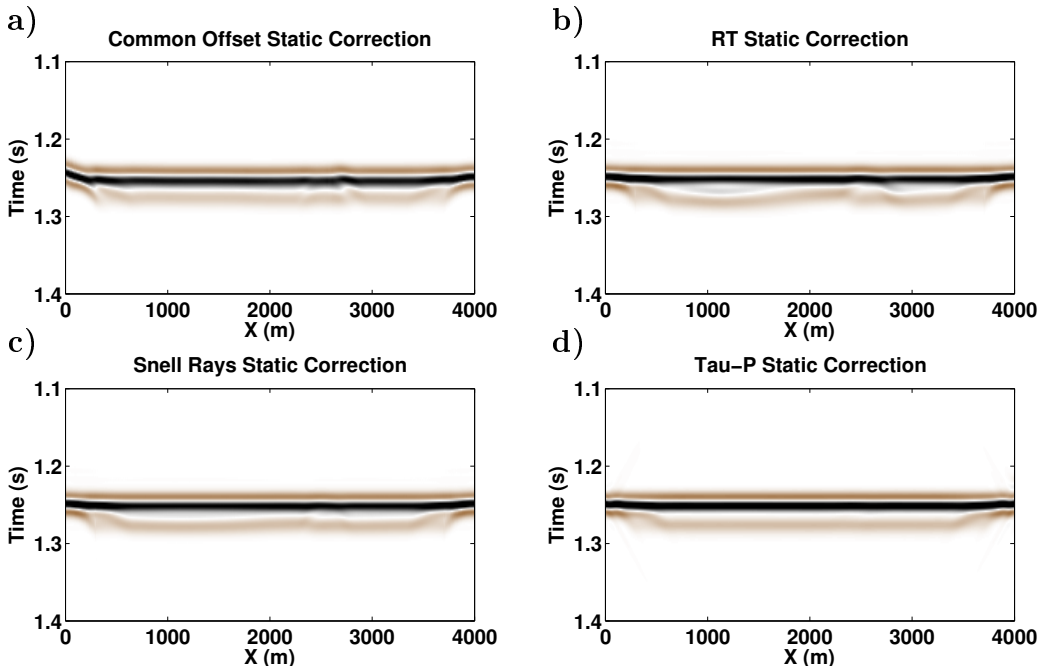

Figure 3.16: Zoomed plot of the deep reflector after removing the statics in each raypath sensitive domain. (a) Common offset domain. (b) Radial trace domain. (c) Snell trace domain. (d) τ-p domain.

transforms compared here successfully achieved the goal of removing the reflection distortions caused by the near-surface. However, better coherency was provided by the solution in the τ-p domain. The main advantage of the τ-p transformation is that vertical velocity changes can be accommodated without having any a priori information. However, due to the limited aperture of the seismic data, the integration in equations 2.5 and 2.6 is truncated, leading to the possible introduction of numerical artifacts. This also has an important effect on the ability to recover the original amplitudes after applying the inverse transformation. The strengths of the RT and ST transforms reside in their very cheap computational cost and complete invertibility. However, the first assumes that propagation occurs in a constant velocity medium. The second requires the character of the vertical velocity changes to be known.

Based on these observations, I consider the τ-p domain to be the more appropriate choice for dealing with non-stationary near-surface effects. The numerical artifacts that can be introduced during the transformation can be removed by filtering the data after

the transformation is performed. On the other hand, a careful selection of the algorithm and parameters for the τ-p transformation must be done in order to minimize amplitude distortions during the processing.

Chapter 4

Field Data Near-surface Corrections

Multiple approaches have been developed for dealing with non-stationary or raypath-dependent near-surface effects. Wave-equation datuming (Wapenaar et al., 1992; Berryhill, 1984; Shtivelman and Canning, 1987; Yilmaz and Lucas, 1986) and dynamic or ray-traced static corrections (Blackburn, 1981; Krey, 1978; Blyth et al., 1989; Alkhalifah and Bagaini, 2006; Bagaini and Alkhalifah, 2006) have been proposed to account for this. Wenzel (1988) proposed a Kirchhoff-based near-surface correction in the τ-p domain for the processing of wide-angle P-wave data. In varying degrees, all these approaches require a velocity model for the near-surface and the medium beneath. This makes them difficult to use when incomplete information about the near-surface is available.

Henley (2012) introduced an alternative approach based on the concepts of interferometry and raypath consistency in which no velocity model for the near-surface is needed. Applications of this approach have been successfully demonstrated in both P- and S-wave statics applications (Henley, 2012, 2014a). The problem of raypath-dependent statics was addressed by moving the data to a domain where amplitudes are a function of raypath angle, by using the radial-trace (RT) transform (Claerbout, 1983). The main weakness of the approach is that the RT transform remaps amplitudes assuming an underlying constant velocity model.

I propose using the τ-p transform as a more complete way of moving data to a raypath-consistent domain while accounting for vertical variations of velocity. In this work I will apply the robust of the "raypath interferometry" approach to solve for S-wave statics. An important feature of this method is that near-surface effects are extracted from the reflected data. Therefore, no first break analysis or refraction data are needed. Moreover, I will show how accounting for the non-stationarity of the problem provides stacking power improvements for both shallow and deep events simultaneously.

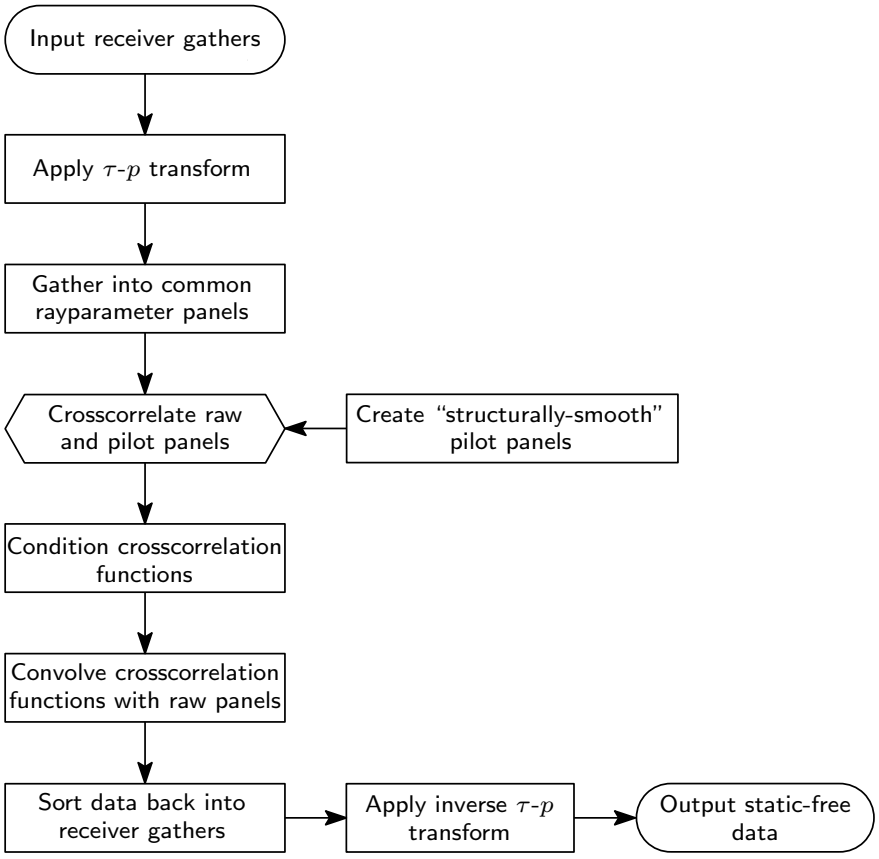

Figure 4.1: Interferometric near-surface corrections processing flow.

4.1 Processing Flow

The processing flow used to remove near-surface effects from field data is outlined in Figure 4.1. It is a modified version of the work-flow introduced by Henley (2012) where near-surface effects are captured and removed by using interferometric principles. Here, input receiver gathers are transformed to the τ-p domain and gathered into common-rayparameter panels. An important difference with the work-flow of Henley (2012) is that the transformation to the raypath-consistent framework is done without the need of a NMO correction. This relieves the process from any errors that could be introduced by the inaccuracy of the NMO velocity picking.

A set of pilot traces which represent a model of the data without near-surface effects is then computed. They are obtained by enforcing continuity on the seismic events, after sorting the data into common-rayparameter panels.

Crosscorrelation between the input and pilot traces is then performed. The output set of crosscorrelation functions should be conditioned to be used as matching filters in a later step. Whitening the spectrum of these functions is needed to preserve the original amplitude spectrum of the data. Hanning weighting (Henley, 2012) is then used to attenuate or suppress any spurious energy captured during the crosscorrelation operation, especially at unrealistically large time lags. The resulting set of conditioned functions is then convolved with the input data to remove the near-surface effects.

By using this deconvolution approach, I aim not only to produce a time shift on the seismic traces, but also to remove waveform variations attributable to event uncertainty and multipath arrivals (Henley, 2012). Doing this in the τ-p domain relaxes the assumption of a constant velocity earth used in the radial-trace transformation. Therefore, when vertical velocity variations are present, the τ-p transformation should honor the kinematics of the wavefield more completely.

4.2 Sinopec dataset

The dataset used in this part of the thesis was facilitated by Sinopec. It consisted of 209 source points with a 20 m spacing acquired in an undisclosed area. A maximum of 1540 channels per shot were recorded with a 10 m receiver spacing in a split-spread configuration, providing a maximum offset of 7700 m. Figure 4.2 shows the geometry of the line. Notice that source points start at receiver station 540. This implies that in receiver stations 1 to 500 near-offset information will not be present.

Conventional processing was applied to the vertical component data to produce a reference stacked section. Refraction statics were computed after first break picking. This static solution provided the source-side corrections used later in the processing of the horizontal components. Figure 4.3 shows the resulting CMP stacked section. Notice the nearly horizontal and continuous character of the events from CMP 1 to 1000. After CMP 1000, the events exhibit anticlinal folding.

The pre-processing of this dataset was critical, due to the presence of acquisition problems. Misorientation of the horizontal components of the receivers and consistent polarity

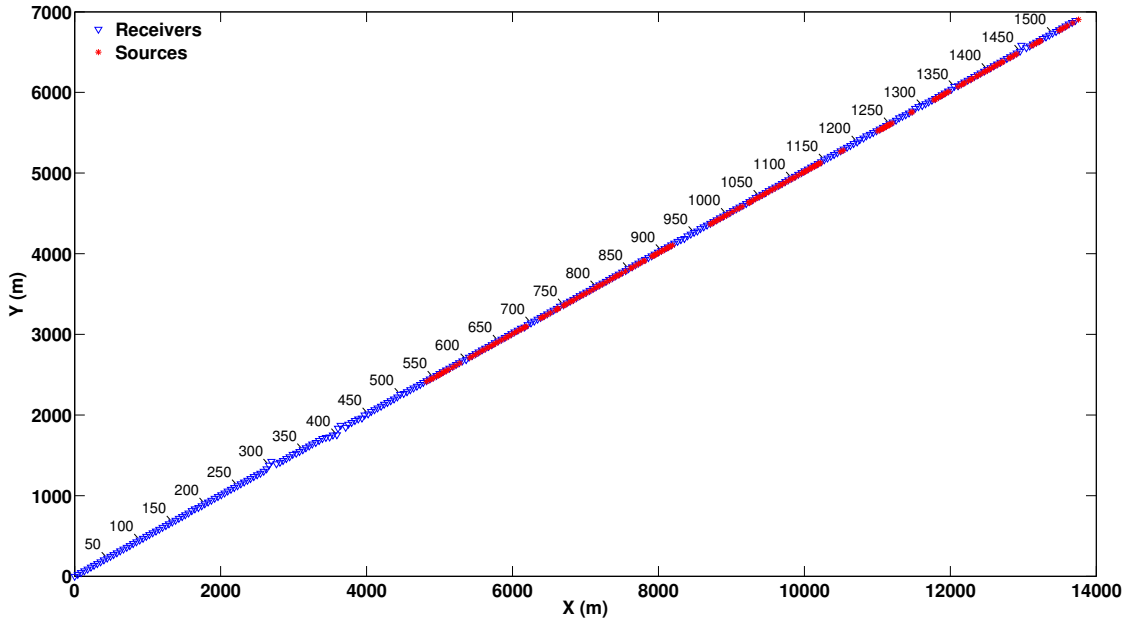

Figure 4.2: 2D-3C survey geometry. Notice the presence of gaps in the source locations. No source points were recorded between receiver stations 1 to 540.

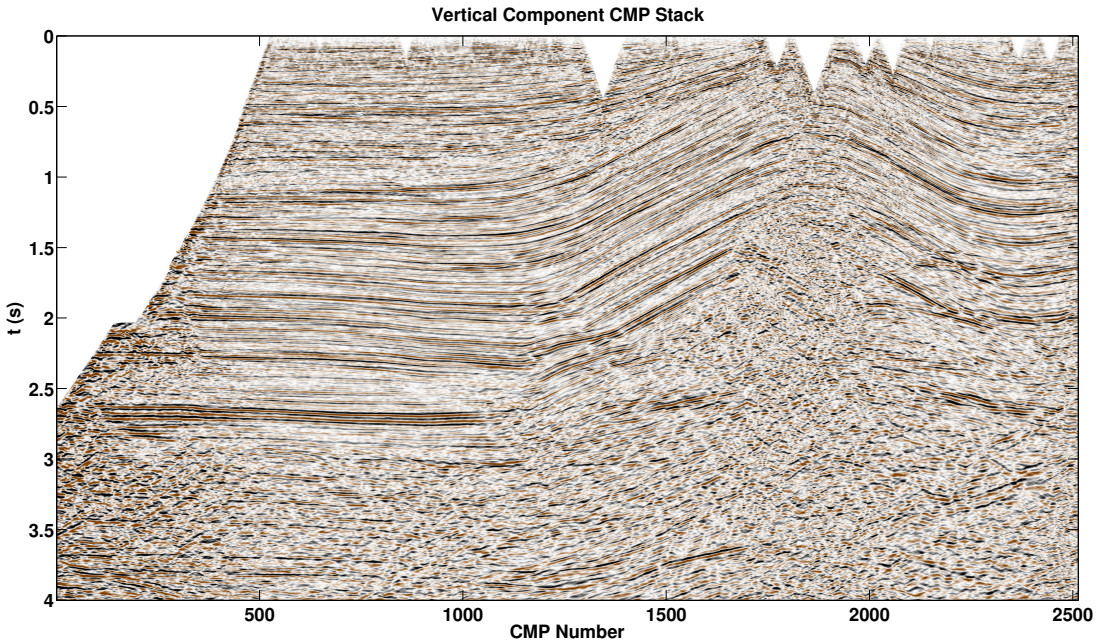

Figure 4.3: Vertical component CMP stacked section. Notice the continuity of the events along the line. Reflectors show a flat character between CMP stations 1-1000 and then are folded into an anticline shape.

reversals were found. Before explaining the processing of the near-surface effects I first show how these problems were approached.

4.2.1 Rotation toward the source-receiver plane

One of the first steps in the processing of the horizontal components is the rotation of the recorded data into the plane defined by the source and receiver locations and the normal to the measurement surface. The component rotated toward the source is referred to as the "radial component" and the perpendicular to it is the "transverse component". In conventional 2D-3C data processing this is achieved by reversing the polarity of all the traces recorded in the inline component, with either positive or negative offsets, depending on the polarity convention chosen by the analyst. This simple correction assumes that all sources and receivers are already located in the same plane. However, this condition may not be true when obstacles are present on the field and receivers need to be planted at an offset from the original plane defined for the survey.

Figure 4.4 shows a zoom around the source station 197 and some of the receivers that were live for that shot. Notice that the receiver stations 1452-1458 and 1502-1505 are located away from the original plane defined for the 2D survey. A simple polarity reversal will not account for this effect and the rotated data will not represent true radial or traversal components. For this reason, in this study I chose to perform a full 2D rotation as in the processing of 3D-3C data. In this way, the data will be rotated toward the actual plane defined by the source and receiver locations.

Figure 4.5a shows the inline component data before performing the rotation toward the source. Using the first arrivals of the vertical component data as a reference, I chose to rotate the horizontal components to produce a trough around the first arrivals. In fact, the first arrival energy recorded on the horizontal components is P-wave refracted energy that has been projected onto these components. Based on this, all the traces at positive offsets must show a polarity reversal after rotation, as can be observed in Figure 4.5b. Notice that not only the first arrival energy now shows a consistent polarity but also the low frequency noise displays better coherency.

Since I chose to perform a full 2D rotation, additional changes can be observed on the

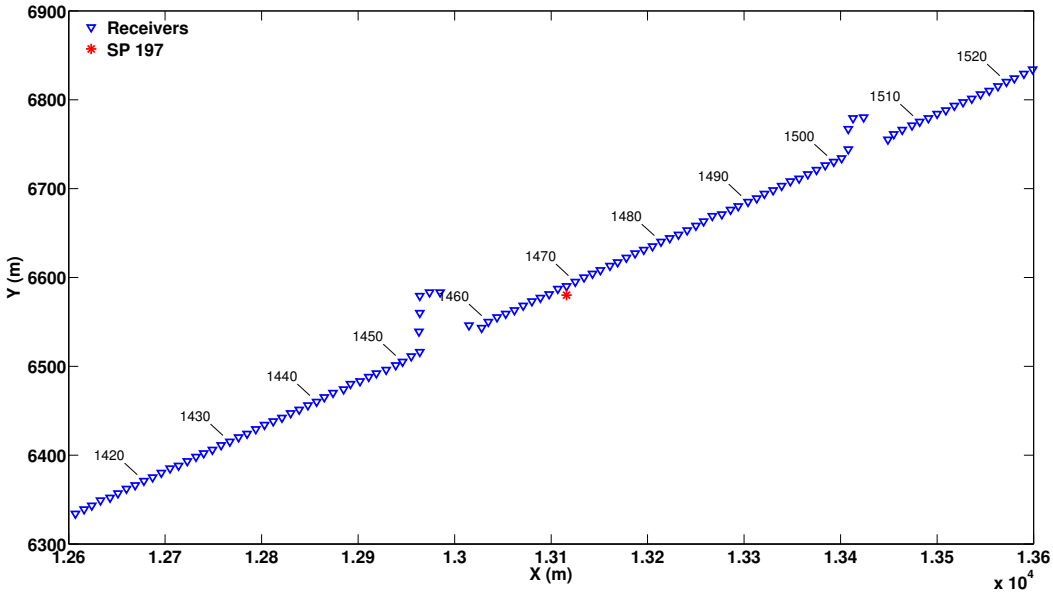

Figure 4.4: Receivers used to record source point 197. Notice how the receiver stations 1452-1458 and 1502-1505 are located outside the original plane define by the 2D survey.

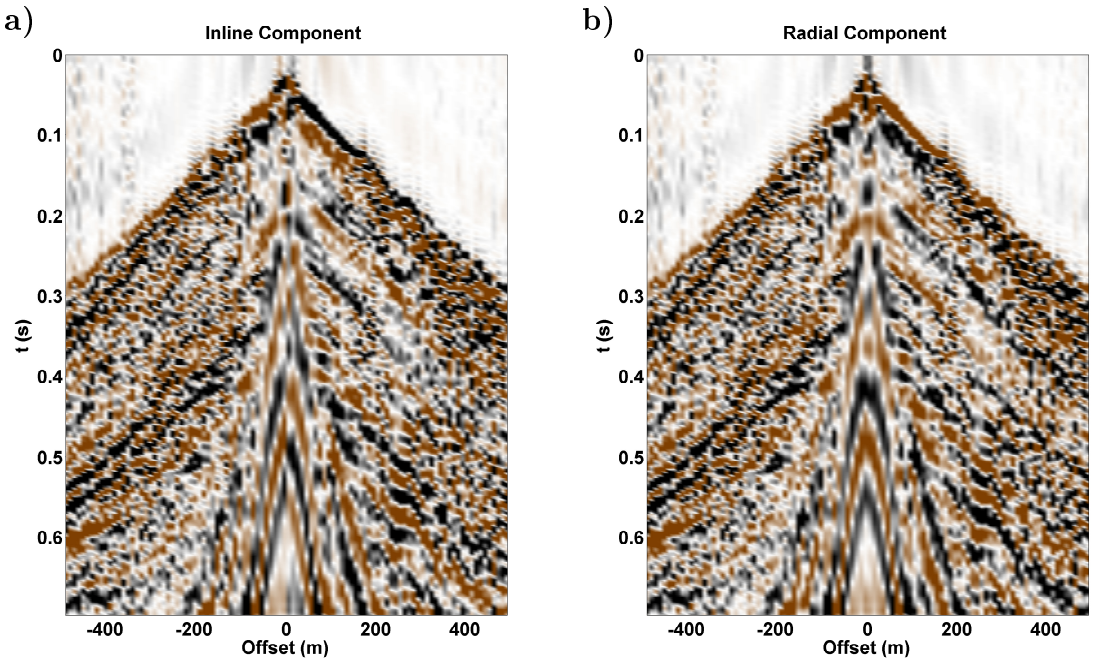

Figure 4.5: Source gather 197 (a) before and (b) after rotation toward the radial direction. The polarity of the first arrivals after rotation matches on both ends of the spread. The surface wave signal also displays better coherency.

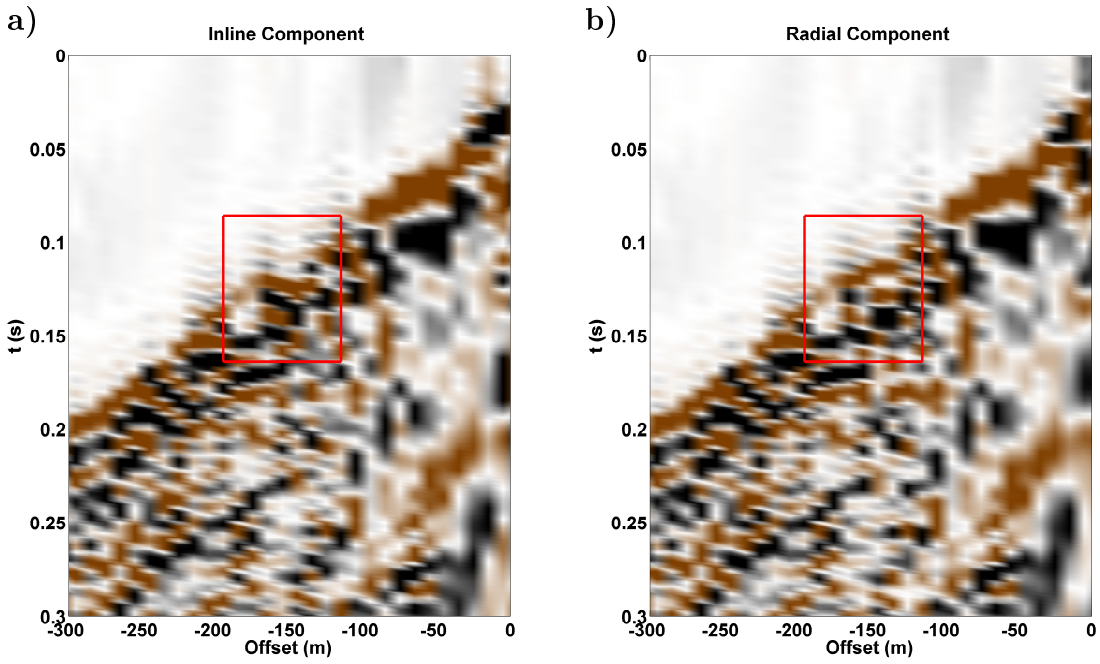

Figure 4.6: Zoom view around the first arrivals on the negative offsets of source gather 197. After using a full 2D rotation the first arrivals recorded by the receivers outside of the original 2D plane (red box) show better coherency. This would not have been corrected if a simple polarity reversal on one end of the line was used to rotate the horizontal components toward the source.

data recorded at negative offsets. Figure 4.6 shows a zoom around the first arrivals recorded at negative offsets. Notice how the first arrivals enclosed in the red box show better coherency after rotation. These traces correspond to the receiver stations 1452-1458 which are outside of the original 2D plane defined by the survey. Using a full 2D rotation enabled us to correct for receiver orientation on both ends of the spread and project the data onto true radial and transverse orientations.

4.2.2 Polarity corrections

After rotating the data toward the radial and transverse directions I identified some polarity reversals still present in the data. Figure 4.7 displays the (a) vertical and (b) radial component data recorded at source point 197. The traces with polarity reversals are enclosed in the box on Figure 4.7b. This type of polarity problems may be related to misorientation of the receivers on the field. Comparing the radial and vertical component data it can

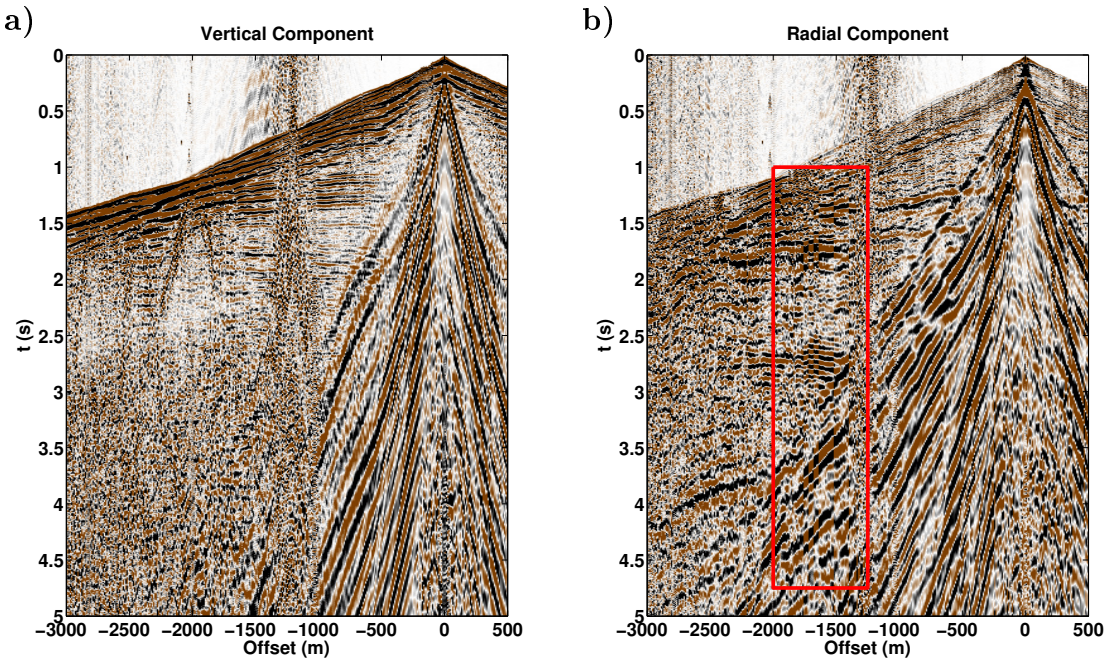

Figure 4.7: (a) Vertical and (b) radial component data recorded by source gather 197. Enclosed in the red box is a set of traces with polarity reversal problems.

be observed that such polarity reversals are not present on the vertical component data. This confirms that the receivers with polarity reversals were planted with the horizontal components oriented in the opposite direction compared to the rest of the survey.

To solve this problem, I performed a crosscorrelation based analysis to identify all the receiver stations with orientation problems. First, radial and vertical component data were sorted into receiver gathers. Then, the gathers were windowed around the first arrivals, and crosscorrelations of the radial and vertical component data were computed. Finally, all the output crosscorrelation functions that belong to the same receiver gather were stacked to improve signal/noise ratio. Since the vertical component data are not affected by the misorientation of the horizontal components, the output crosscorrelation functions must show a change in polarity when compared with neighbour receiver stations.

Figure 4.8a shows the initial crosscorrelation panel for the receiver stations recorded by source point 197. Notice how the sign of the zero-lag crosscorrelation amplitudes changes between receiver stations 1275 to 1350. On this panel, the receiver stations with polarity problems can be easily identified and captured.

The previous panel was further improved by performing one additional pass of crosscorrelation. In the second pass I created a set of pilot traces which represent the data without polarity reversals. For this purpose I used a trace-mixing process, with a window of one hundred traces, to remove all the polarity changes, as can be observed in Figure 4.8b. Next, the initial set of crosscorrelation functions are crosscorrelated with the pilot functions. The output is shown in Figure 4.8c. Notice how the crosscorrelation panel now shows sharper amplitudes around the zero-lag of the crosscorrelation. To make this correction automatically, I captured the sign of the crosscorrelation functions at the zero-lag for each receiver station and saved them in a database. This generates a flag with a value of -1 for traces with polarity problems and +1 for traces without problems. These values were loaded to the trace headers and used to remove the polarity reversals by multiplying the traces by these header values.

Figure 4.9 shows the source gather 197 after polarity corrections. Notice how the events now show a more coherent character. The surface-wave noise also displays better coherency. This will facilitate its removal later in the processing sequence.

4.2.3 Near-surface corrections

Figure 4.10 shows a common-receiver stacked section before near-surface corrections. Source-side statics and surface-wave noise was removed before stacking the data. There, one can observe the jitter present in the events between 1 s and 3 s which are evidence of static problems. The near-surface processing flow used on this dataset was the same as introduced in Figure 4.1. The four key stages of this work-flow are shown in Figure 4.11.

In the processing of data from structurally complex areas, computing pilot traces may require additional steps. In particular, the structural features present in the data must be preserved at all times. Therefore, enforcing coherency on the seismic events, while creating pilot trace panels, must be handled carefully. To compute the pilot traces in Figure 4.11b a horizon following the structural trend displayed in Figure 4.10 was picked and the data were flattened to this horizon. After removing the structural trend, trim statics and lateral trace averaging were used to force continuity on the events. For the lateral trace averaging, Gaussian weights were applied to the traces within each window before averaging. In this

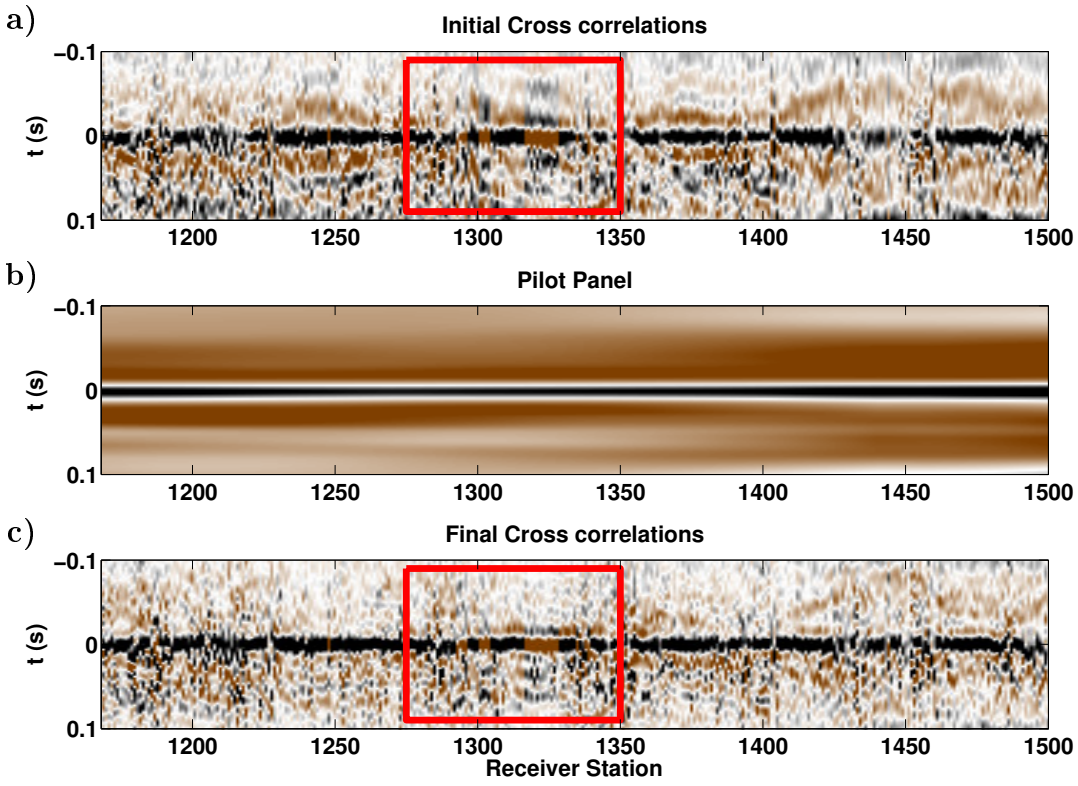

Figure 4.8: (a) Vertical and radial component crosscorrelation functions stacked by receiver gather. (b) Pilot traces representing a set of crosscorrelation functions without polarity reversal. (c) Final set of crosscorrelations between the initial set of functions and the pilot panel. Enclosed in the red box the receiver stations with polarity problems can be identified.

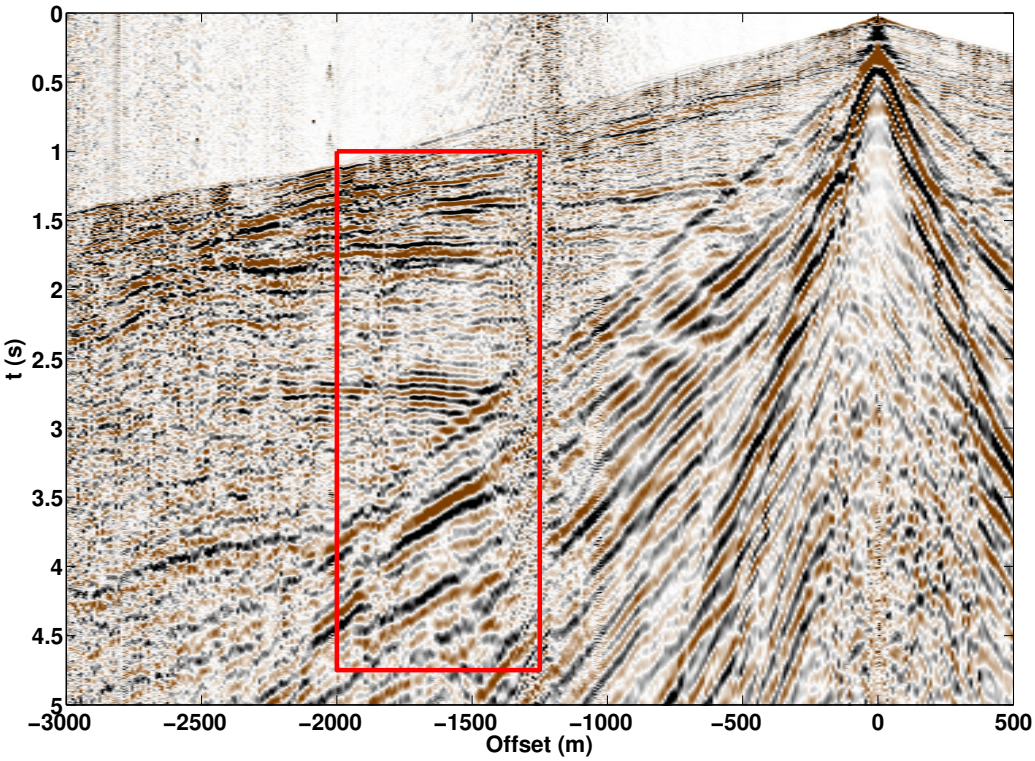

Figure 4.9: Source gather 197 after polarity reversals. The events inside the red box now display a consistent polarity.

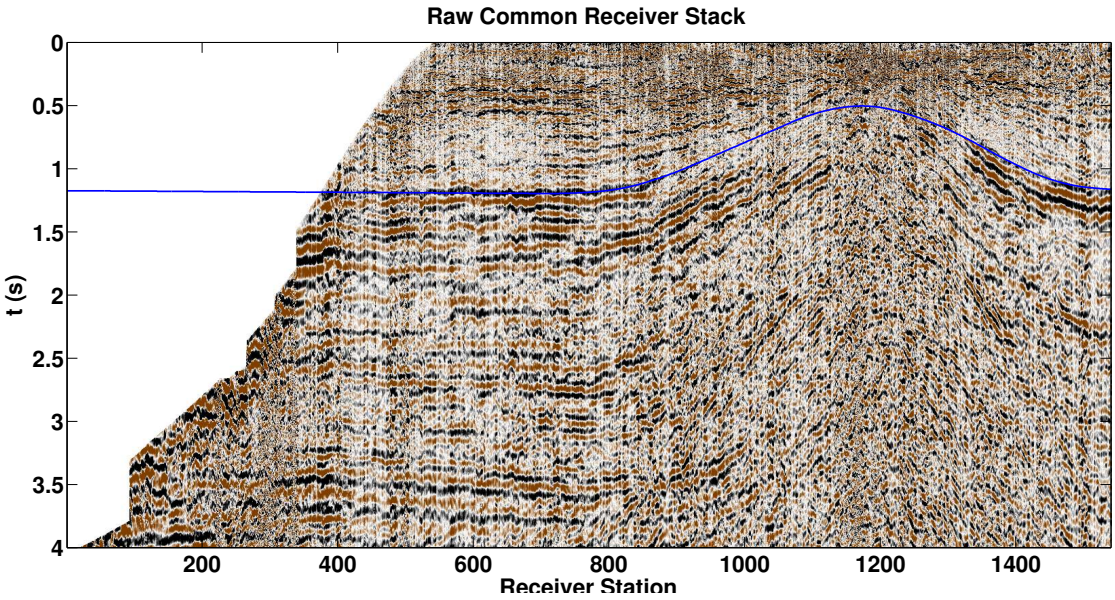

Figure 4.10: Common receiver stack before near-surface corrections. The blue line represents an horizon picked to capture the structural trend of the events.

way I intend to localize the averaging process around each fixed receiver location while still using reasonably wide windows ($\sim$ 50 traces). Once the filtering is completed, the structural trend initially picked is added back to the section.

Figure 4.11c displays the output of the crosscorrelation between the raw (Figure 4.11a) and pilot traces (Figure 4.11b). These crosscorrelation functions were conditioned by applying spectral whitening and Hanning weights. The spectral whitening aims at broadening the spectrum of the crosscorrelation functions. On this way, when the raw data is convolved with the crosscorrelation functions, in the next step, the original bandwidth of the data is preserved. The Hanning weights are designed in such a way that any energy at very large crosscorrelation lags is attenuated. Notice how most of the energy in Figure 4.11c is confined between $\pm$0.1 s. Therefore, a Hanning window centered around the zero-lag of the crosscorrelation functions that attenuates energy at times with absolute values larger than 0.1 s was used. The selection of this parameter also depends on the magnitude of the near-surface effects observed in the data. After inspection of the jitter present in the common receiver stack section near-surface effect of less than 0.1 s were expected in this dataset. Figure 4.11d shows how the convolution of these functions with the raw traces removes most of the jitter present in the data.

After all the rayparameter panels were corrected, the data were sorted back into receiver gathers and an inverse τ-p transformation was performed. Figure 4.12 displays common-receiver stacks before and after near-surface corrections, zoomed around receiver stations 400 to 1100. In Figure 4.12a, the lack of coherency on the events along the section is evident. The continuity of both shallow and deep events is interrupted by sudden time shifts between receiver stations. After corrections (Figure 4.12b), all the events exhibit better coherency. Moreover, the seismic resolution of the data before 0.8 s has been improved. This is the result of a better alignment of the waveforms before stacking the traces.

The observations made on the common-receiver stacks also apply to the CCP stacks in Figure 4.13. On both stacked sections spiking deconvolution and FX filters have been applied to improve resolution and coherency of the events. This type of post processing did not remove the jitter present in the raw data (Figure 4.13a). After removing the near-surface time delays, the continuity of the events is significantly improved, especially in the shallower

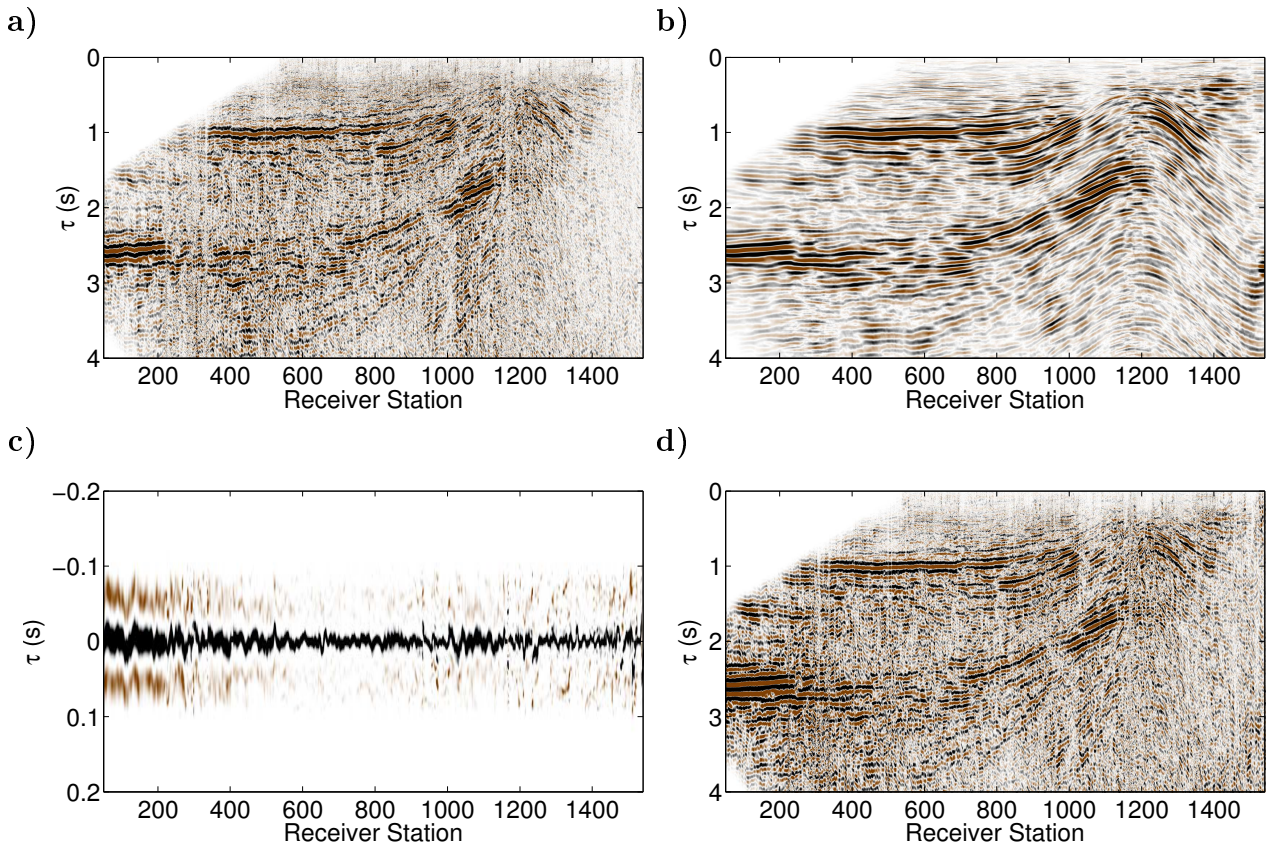

Figure 4.11: (a) Input common-rayparameter panel from the Sinopec dataset ($p = -3 \times 10^{-4}$ s/m). (b) Pilot rayparameter panel. (c) Crosscorrelation between (a) and (b) after conditioning. (d) Convolution of (a) and (c). Notice how coherency has been improved over most of the events on the rayparameter panel including the flanks of the structure around receiver station 1100.

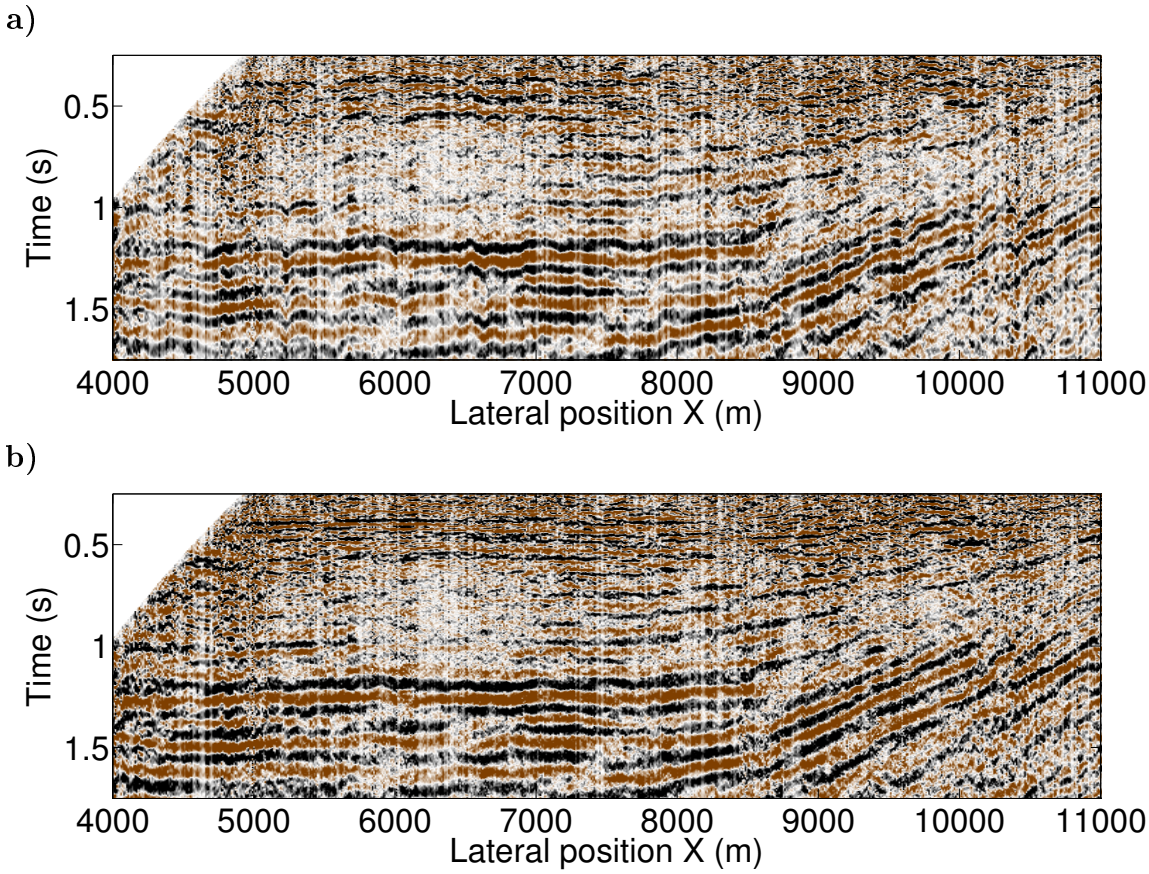

Figure 4.12: Common-receiver stacks (a) before and (b) after receiver-side static corrections. Continuity of the events has been improved on (b) even around the flanks of the structure. Resolution and coherency of the events above 0.5 s has been improved.

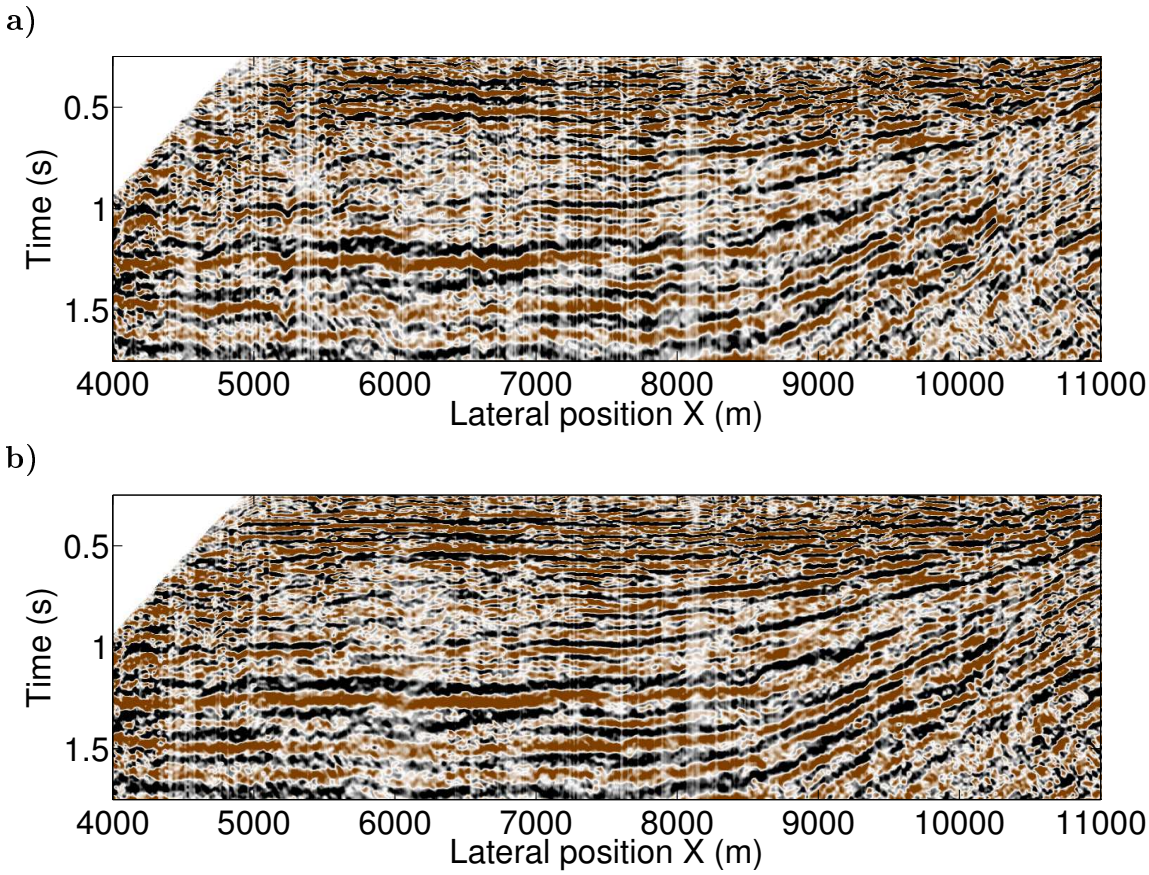

Figure 4.13: CCP stacked sections (a) before and (b) after receiver-side static corrections. The jitter present on the events on (a) has been removed after using raypath-consistent near-surface corrections. The events above 0.5 s in (b) are easier to track and display better resolution after corrections.

part of the section (Figure 4.13b). Since shallow events covered a wider range of reflection angles, they benefited most from removal of near-surface effects in this raypath-consistent framework.

4.3 Hussar dataset

In 2011 the Consortium for Research in Elastic Waves Exploration Seismology (CREWES) collaborated in the acquisition of a broad-band (1-100 Hz) experiment in the Hussar area in Southern Alberta (Margrave et al., 2012). Although originally designed for investigating broad-band inversion schemes, the preliminary processing of the horizontal components re-

vealed the presence of important near-surface time delays on the recorded converted-wave events. Figure 4.14a shows a radial component source gather after surface-wave removal and source static corrections. Notice how the events between 1500 m and 2000 m offsets are pulled down due to low near-surface velocities. This is even more evident in the common-receiver stack displayed in Figure 4.14b. There, one can also observe how the near-surface causes the continuity of the events to be interrupted by jumps between consecutive receiver stations.

Figure 4.15 illustrates each stage of the processing flow in Figure 4.1. Figure 4.15a represents one of the common-rayparameter panels obtained after transforming common-receiver gathers to the τ-p domain. A pilot panel (Figure 4.15b) is then computed by applying trim statics and a laterally moving average process, to remove the shifts between traces, and enhance the continuity of the events. Since a pull down effect with a width of approximately 400 m was identified between x = 1600 m to 2000 m, a window of 800 m width was used for the lateral smoothing.

The crosscorrelation between the input panel and the pilot traces is plotted in Figure 4.15c. Notice that the lag of the crosscorrelation traces has captured the deformation present in the input panel. Spectral whitening and Hanning weights have been applied to these traces, to increase the bandwidth, and suppress energy at very large lags, respectively. Since the largest near-surface effect observed in the common-receiver stack was of 200 ms, the Hanning window was designed to attenuate any crosscorrelation energy at time lags larger than this magnitude. The near-surface correction is then applied by convolving the input traces with the conditioned set of crosscorrelation functions (Figure 4.15c). The output is displayed in Figure 4.15d. Notice that the deformation present in the input panel between the x-coordinates 1500 m and 2500 m has been removed. Moreover, the continuity of the events all along the section has been significantly improved.

This process is applied over all the rayparameter panels available. Following this, an inverse τ-p transform returns the data back to the time-offset domain. The corrected source gather displayed in Figure 4.16a shows how the coherency on the events has been improved. Of importance is the improvement in coherency of the energy recorded at large offsets ($>$ 3000 m). On the raw source gather (Figure 4.14a) this energy is poorly recognizable, not only

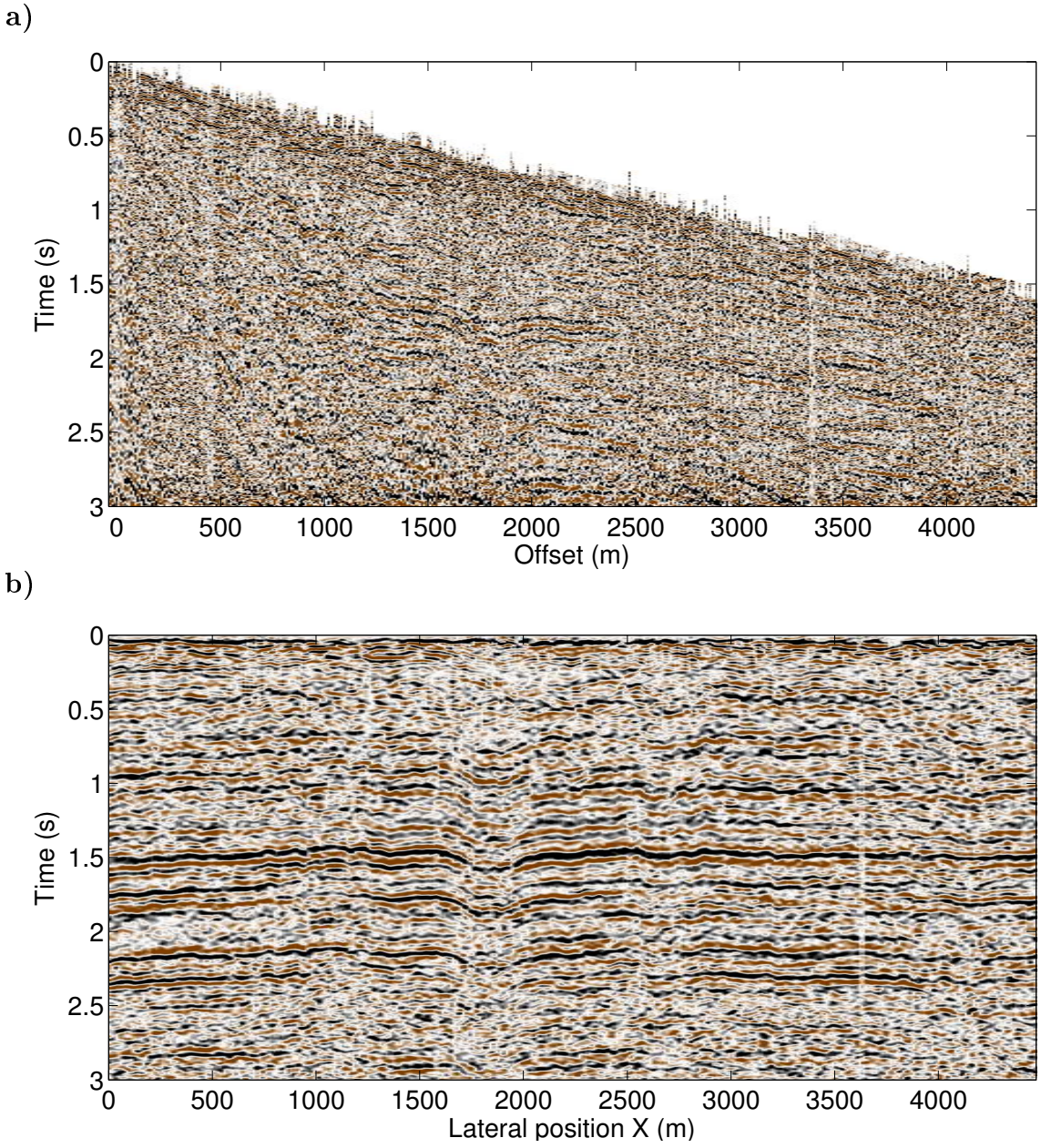

Figure 4.14: (a) Radial component source gather and (b) common-receiver stacked section from the Hussar experiment before receiver-side static corrections. Notice the pull down between offsets 1500 and 2500 m affecting the events around 1.7 s in (a). The effect is more evident in (b) where the shifts between traces caused by receiver statics problems can be observed.

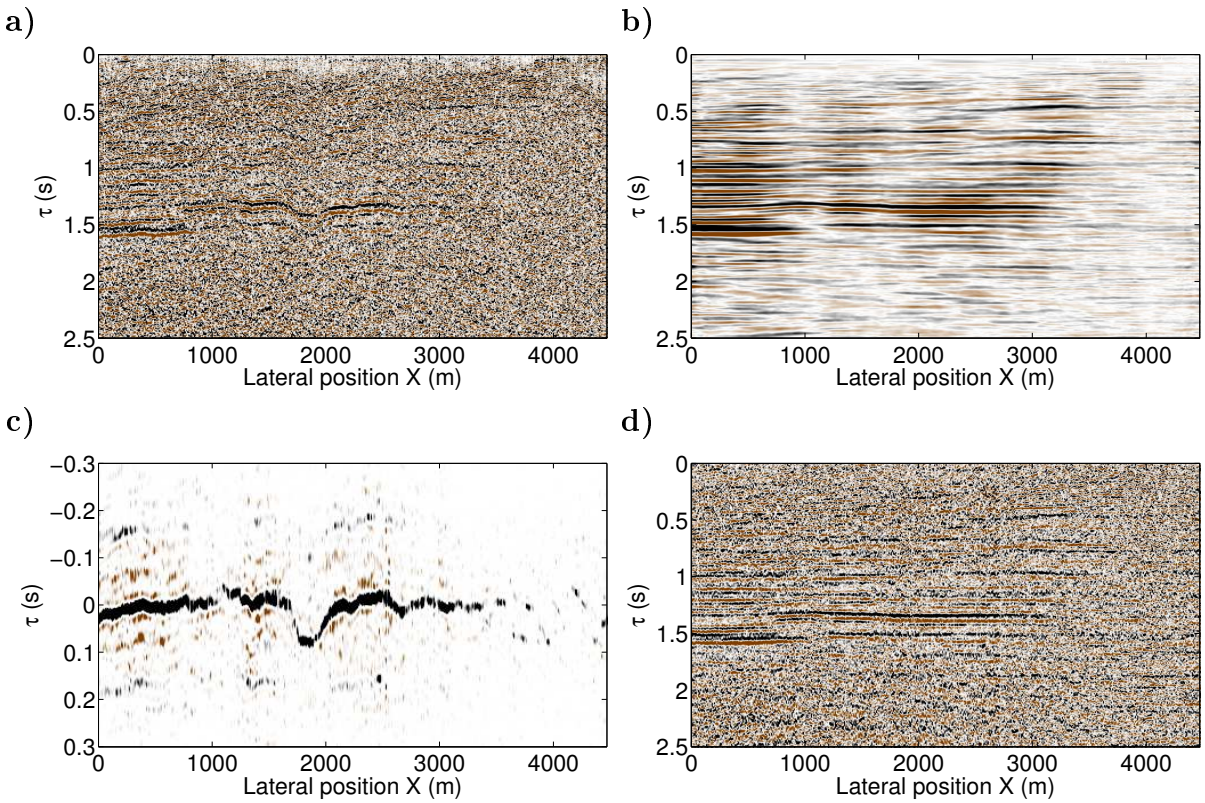

Figure 4.15: Key elements of the interferometric processing of near-surface effects in the τ-p domain. (a) Input common-rayparameter panel. (b) Pilot rayparameter panel created by applying trim statics and trace averaging on (a). (c) Crosscorrelation between (a) and (b) after conditioning. (d) Convolution of (a) and (c). Notice how coherency of the events has been improved over most of the section on the rayparameter panel.

due to the very low signal-to-noise ratio but also to the lack of continuity in the amplitudes.

The common-receiver stack after near-surface corrections (Figure 4.16b) shows very important improvements in the alignment and stacking power of the events in the section. This is especially true at times less than 1 s where almost no coherent energy was initially recognizable. The same observations can be made on the common-conversion-point (CCP) stack plotted in Figure 4.17a. A CCP-stack obtained by using a surface-consistent solution is displayed in Figure 4.17b for comparison purposes. Although on both sections the coherency of the event around 1.5 s has been improved and the deformation removed, it is at early times (< 1 s) where the raypath-consistent solution displays superior results.

Dipole sonic data from a well located around the x-coordinate 3950 m was used to compute a synthetic converted-wave seismogram. The P-wave sonic, S-wave sonic and density logs where loaded into the Syngram software available in the CREWES toolbox (Figure 4.18a). A PS-gather covering a range of offsets from 0 m to 3500 m was modelled without including NMO effects (Figure 4.18b). The stacked trace is repeated and inserted in the CCP stack at the well location. A bulk-shift of 94ms was applied to the synthetic traces to compensate for the lack of well log velocities in the overburden. This bulk-shift was obtained by crosscorrelating the synthetic trace with the actual traces around the well location. The well tie displayed in Figure 4.19 confirms that the events in the shallow part of the sections are correlated with rock property changes recorded in the well logs. This correlation would have been difficult to identify on the CCP-stack obtained by using surface-consistent static corrections (Figure 4.17b). There, almost no coherent energy is present at shallow times around the x-coordinate 3950 m.

4.4 Remarks

Correcting acquisition-related problems from the data before applying any processing is critical to ensure reliable results. The τ-p transformation involved in my near-surface correction process is very sensitive to this type of problem. Particularly, the presence of polarity reversals or sudden changes in amplitude can introduce numerical artifacts in the transformation. Therefore, proper data conditioning is needed to avoid the introduction of spurious events

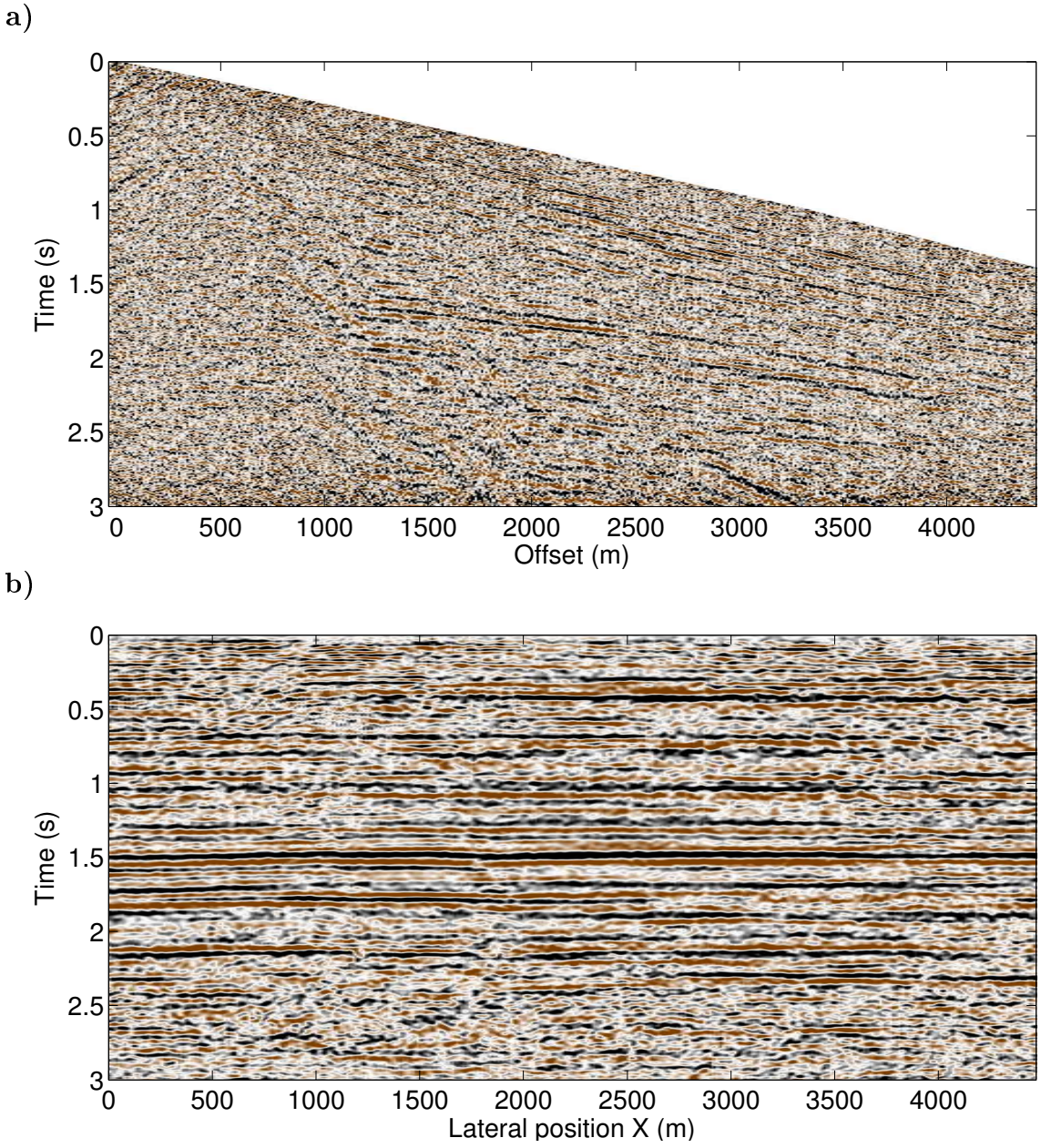

Figure 4.16: (a) Radial component source gather and (b) common-receiver stacked section from the Hussar experiment after receiver-side static corrections. The deformations present on the moveout and geometry of the events have been successfully removed. Stacking power of the events on (b) has been improved all over the section, especially for the events before 0.5 s.

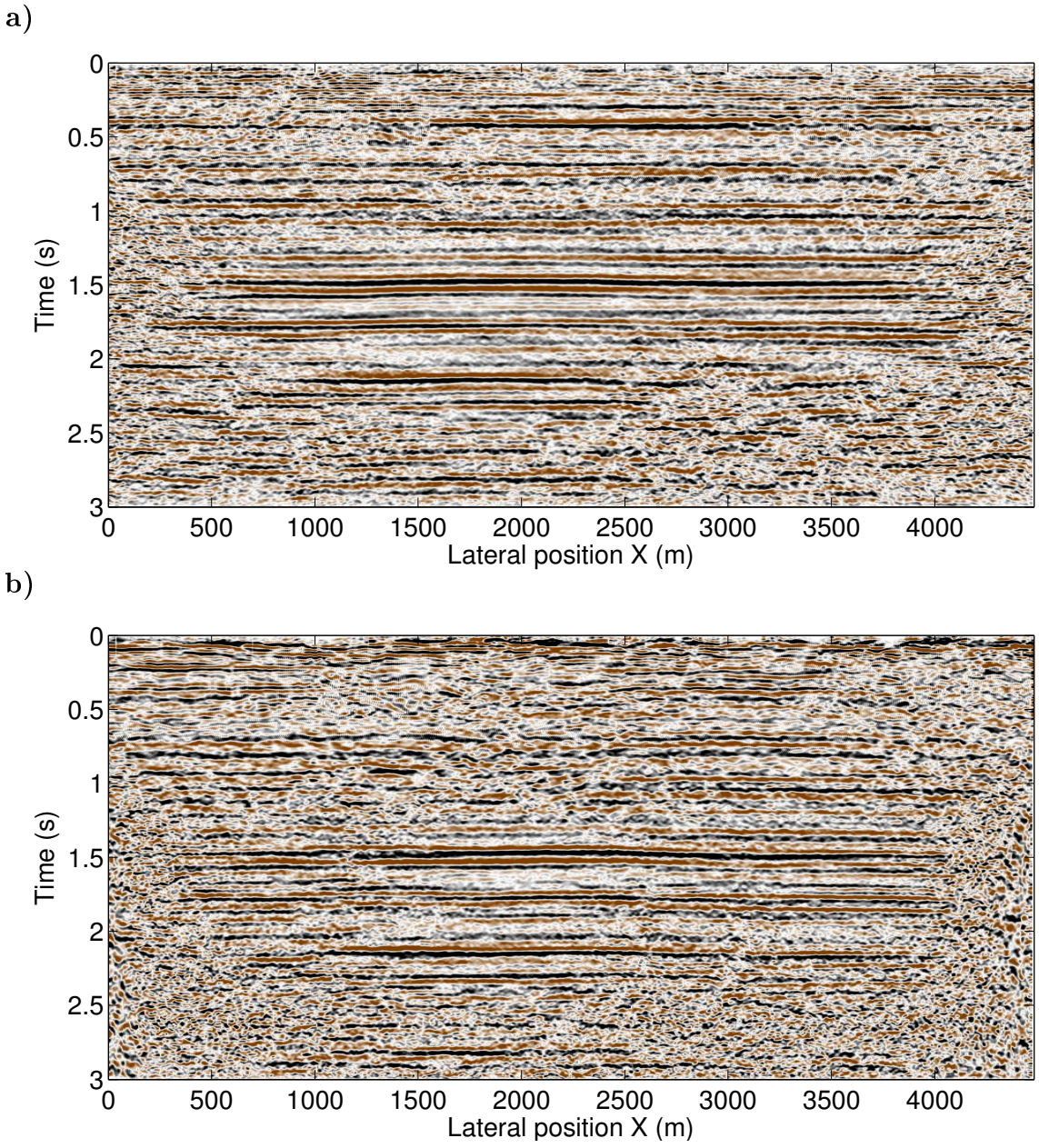

Figure 4.17: CCP stacks obtained by using (a) a raypath-consistent solution and (b) a surface-consistent solution. Notice the superior improvement on resolution and coherency of the events before 0.5 s after using raypath-consistent near-surface corrections.

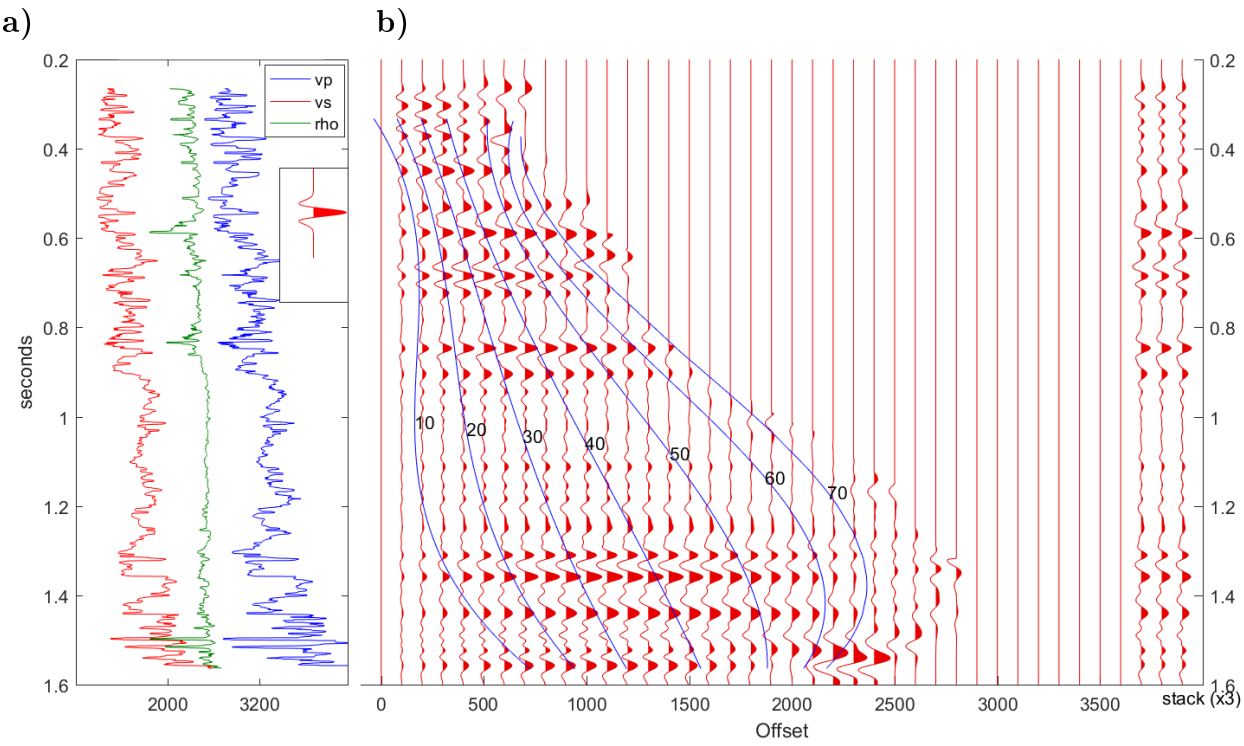

Figure 4.18: (a) Well logs and (b) resulting synthetic PS-gather. The blue contours on the synthetic gathers represent the incidence angles. The last three traces on panel (b) are repetitions of the trace obtained after stacking the gather.

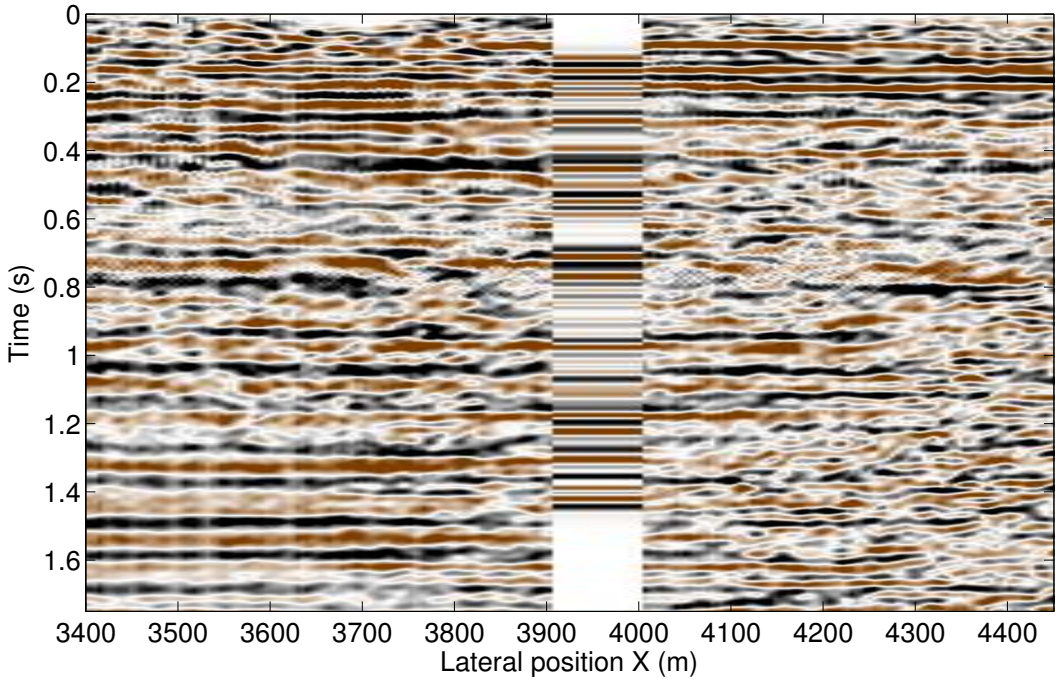

Figure 4.19: Well tie obtained after creating synthetic converted-wave traces using dipole sonic data available at a well located around x = 3900 m. Correlation of the field data and synthetic seismogram events above 0.5 s is very clear after applying raypath-consistent near-surface corrections.

in this method.

The ability of raypath-consistent corrections to accommodate near-surface effects for shallow and deep events simultaneously is one of the most important features of this processing flow. The computation of pilot traces is one of the most critical steps in this workflow. Since the method relies on enforcing continuity along seismic events there is a risk of removing structural information. To avoid this, one must be careful when choosing the size of the windows used for applying any lateral smoothing operator. In general, one should choose a large enough window to remove long wavelength near-surface effects but at the same time small enough to not remove structural features.

In the processing of deep reflection data the assumption of vertical raypath angles may be sufficient for the use of a surface-consistent approach. However, the very low velocity of S-waves and the ability of shallow events to reach wide reflection angles requires a raypath-dependent framework. The methodology I showed in this study demonstrates how this can be achieved even when the geology of the area presents some structural complexity. This approach can be useful in the processing of wide-angle broadband data, where the assumption of vertical raypaths in the near-surface is threatened.

Chapter 5

Near-surface S-wave velocity inversion

A near-surface velocity model is one of the typical products generated when computing static corrections, particularly in the processing of PP data. Critically-refracted waves are the input usually needed for this process. However, in multicomponent data acquisition, critically-refracted S-waves are difficult to identify when using P-wave energy sources.

Using scaled versions of P-wave velocity models by assuming a fixed V_p/V_s ratio to compute S-wave static corrections has been demonstrated to lead to inadequate corrections (Cox, 1999; Garotta and Granger, 1988; Tessmer et al., 1990). These authors report lateral changes of the V_p/V_s ratio that range between 2 and 6. Fromm et al. (1985) and Yilmaz (2015) show that S-wave velocity variations in the near-surface do not necessarily conform with the P-wave velocity structure. Therefore, the use of a fixed ratio is likely to significantly under-correct or over-correct the data in some places.

Henley (2012) introduced a raypath-consistent approach in which no near-surface velocity model is needed. Instead, interferometric principles are employed to build a reference wavefield that is free of near-surface effects. Raypath consistency is achieved by processing the data in the radial-trace domain (Claerbout, 1983). In Chapter 4, I showed how this processing can be extended to the τ-p domain where the kinematics of the raypath-dependency can honor vertical velocity changes.

In this chapter I develop an inversion algorithm to compute near-surface velocity models from the raypath-dependent static corrections. A raypath-dependent elevation correction is also introduced in order to separate traveltime distortions produced by velocity changes from those resulting from elevation changes. In this way, I not only provide a set of S-wave statics corrections, but I am able to compute a near-surface S-wave velocity model related to them. This velocity information can be useful for converted-wave imaging and also may form an important input into the creation of starting models for elastic FWI algorithms.

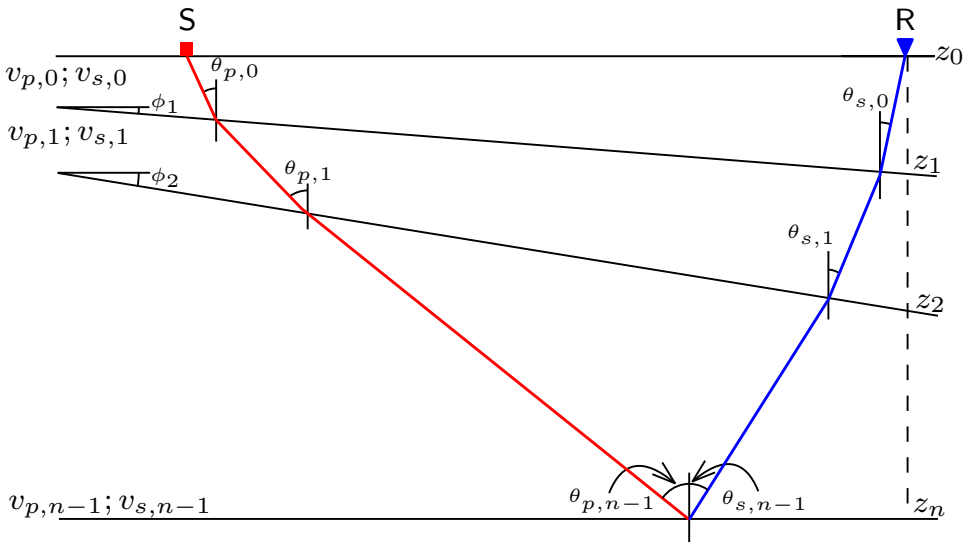

Figure 5.1: Schematic representation of a PS raypath through a model with two dipping layers in the near-surface.

5.1 Raypath-consistent corrections in a multilayer near-surface medium

In a layered medium, the intercept time τ represents the aggregate product of vertical slownesses and thickness (Bessonova et al., 1974; Diebold and Stoffa, 1981; Hake, 1986):

$$\tau = \sum_{i=0}^{n-1} \Delta z_i \left(q_i^d + q_i^u\right) = \tau^d + \tau^u, \tag{5.1}$$

where q_i is the vertical slowness $q_i = \cos(\theta_i)/v_i$ in the i-th layer and Δz_i is the layer thickness $\Delta z_i = z_{i+1} - z_i$. The superscripts ^{d} and ^{u} denote the downgoing and upgoing legs of the raypath in Figure 5.1, respectively. For PS-waves the downgoing segments are controlled by P-wave velocities and the upgoing by S-wave velocities.

Assuming that the near-surface spans the first m layers and that the receiver lies in the $z_0 = 0$ plane, the upgoing τ-contribution in equation 5.1 can be rewritten as

$$\tau^u = \sum_{i=m}^{n-1} \Delta z_i q_i^u + z_m q_{m-1}^u + \sum_{i=0}^{m-1} z_{i+1} \left(q_i^u - q_{i+1}^u\right). \tag{5.2}$$

The first term in equation 5.2 gives the total upgoing τ-contribution from the conversion point to the base of the m-th layer. The second term represents the contribution from the base of the m-th layer to the surface with velocity v_{m-1} and raypath angle θ_{m-1}, as if the

overlying m layers were not present in the model. This term accounts for the replacement process used in static corrections, with v_{m-1} being the equivalent to the replacement velocity.

The effect of the near-surface is therefore contained in the last term of equation 5.2. To remove the near-surface effect amounts to isolating and subtracting this term from the total intercept time. The receiver-side near-surface correction can then be written as

$$\Delta\tau^u = \sum_{i=0}^{m-1} z_{i+1} \left(q_{i+1}^u - q_i^u\right). \tag{5.3}$$

Equation 5.3 is the generalization of Equation 2.10 for a near-surface medium with multiple layers. This correction represents a layer-stripping process in which the τ contribution of each layer i is subtracted and replaced by the τ contribution given by the propagation parameters in the underlying $i+1$ layer. Since the correction depends on the vertical slowness q of each layer, the raypath angles in each layer are honored.

The vertical slowness q is related to the horizontal slowness or rayparameter value p by the relationship $p^2 + q^2 = s^2$, where s is the total slowness or the velocity inverse $1/v$. In horizontally layered media, according to Snell's Law, the rayparameter p is constant, even if conversion occurs along the ray. Hence, by knowing the rayparameter on the surface one can propagate this value through the subsurface if the geological conditions allow it. Therefore, the vertical slowness in each layer can be expressed as

$$q_i^u = \left(s_i^2 - p^2\right)^{1/2}. \tag{5.4}$$

Equations 5.3 and 5.4 are used as the engine for computing static corrections in the τ-p domain in a horizontally layered medium. Given the rayparameter values p measured at the surface, the velocities and thicknesses of the near-surface layers, one can compute the corrections needed to remove the effect of the near-surface in a raypath-consistent fashion.

5.1.1 Elevation corrections

Elevation or datum corrections are often handled by assuming vertical raypaths associated with the velocity of the replacement medium (Cox, 1999). For the sake of consistency I introduce a raypath-dependent elevation correction into my solution.

To extend the near-surface correction process up to a datum different from the recording surface, an additional term in equation 5.3 is needed. This term can be written as,

$$\Delta\tau^u_{elev} = (z_d - z_r)\, q^u_m, \tag{5.5}$$

where z_d is the elevation of the final datum and z_r is the receiver elevation, measured from a fixed reference surface. Notice that for vertical raypaths, where $q = s$, equation 5.5 reduces to the most simple form of elevation correction $\Delta\tau^u_{elev} = (z_d - z_r)/v_m$.

5.1.2 Dipping near-surface layers

For dipping interfaces, equation 5.1 still holds (Diebold and Stoffa, 1981). However, a dip correction is needed for each interface.

Two rotations can be used to address this problem. The first of them allows us to obtain the projection of the total slowness vector along the base of each near-surface layer. The apparent slowness p_a at the base of the $(m-1)$-th layer can be expressed as,

$$p_{a,m-1} = p\cos\phi_m - q_m \sin\phi_m. \tag{5.6}$$

According to Snell's Law the in-plane slowness must be preserved across interfaces. Therefore, the apparent vertical slowness on the $(m-1)$-th medium can be computed as

$$q_{a,m-1} = \left(s^2_{m-1} - p^2_{a,m-1}\right)^{1/2}. \tag{5.7}$$

However, these apparent slownesses are measured over the coordinate system defined by the dipping interface. To obtain the horizontal and vertical slownesses as measured by the reference system defined by the recording surface one must apply a second rotation. This rotation can be written as,

$$\begin{pmatrix} p_{m-1} \\ q_{m-1} \end{pmatrix} = \begin{pmatrix} \cos\phi_m & \sin\phi_m \\ -\sin\phi_m & \cos\phi_m \end{pmatrix} \begin{pmatrix} p_{a,m-1} \\ q_{a,m-1} \end{pmatrix} \tag{5.8}$$

Equations 5.6 to 5.8 can be used to obtain the slownesses needed in equation 5.3 to compute the near-surface corrections. By including a dip correction, any asymmetry that may be present in the raypath-dependent correction can be addressed.

5.1.3 Relationship with interferometric near-surface corrections

Henley (2012) proposed an interferometric approach for near-surface corrections where time differences are captured by computing the crosscorrelation between raw traces and a set of pilot traces. The latter are meant to approximate the recorded wavefield conditions as if the near-surface velocity anomalies had not been present. The same operation can be done in τ-p domain, as shown in Chapter 3. I propose using a fixed τ-p receiver gather, where the near-surface velocity model is assumed to be known, as the representation of the reference wavefield. The τ-difference between the intercept-times at the j-th receiver location and the reference location j_0 is,

$$\Delta\tau_{xcorr,j} = \tau_j - \tau_{j_0}. \tag{5.9}$$

Assuming that only the S-wave velocity structure of the first m layers in the near-surface has changed and including the elevation correction term (equation 5.5), one may write,

$$\Delta\tau_{xcorr,j} = \sum_{i=0}^{m-1} z_{i+1,j}\left(q^u_{i,j} - q^u_{i+1,j}\right) + \left(z_d - z_{r,j}\right) q^u_m - \sum_{i=0}^{m-1} z_{i+1,j_0}\left(q^u_{i,j_0} - q^u_{i+1,j_0}\right) - \left(z_d - z_{r,j_0}\right) q^u_m. \tag{5.10}$$

Reordering terms in equation 5.10, I obtain an expression for the τ-differences in terms of the near-surface corrections at the reference and current locations:

$$\Delta\tau_{xcorr,j} = \Delta\tau_{j_0} - \Delta\tau_j + \left(z_{r,j_0} - z_{r,j}\right) q^u_m. \tag{5.11}$$

Therefore, if the near-surface parameters at a reference location are known, the near-surface corrections at a different location can be computed from the τ differences captured by the crosscorrelation. The last term in equation 5.11 allows us to include an elevation correction in the solution. In the next section I explain an iterative inversion scheme for computing the near-surface parameters.

5.2 Inversion of τ-differences

I employ a quasi-Newton inversion approach to solve for the near-surface parameters. In this inversion an initial guess for the model parameters m is iteratively updated until the minimum of an objective function Φ(m) is reached. I used the L_2 norm of the data misfit

(equation 5.12) as the objective function.

$$\Phi(\mathrm{m}) = ||\mathrm{g(m)} - \mathrm{d_{obs}}||^2, \tag{5.12}$$

where $\mathrm{d_{obs}}$ is the observed data and g(m) is the forward modelled data for a given set of model parameters m. In my formulation, the model parameters used in the inversion are the depth at the base of each layer in the near-surface (z_i), its S-wave slowness (s_i) and its dip (ϕ_i).

At the i-th iteration, the model parameters are updated as

$$\mathrm{m_i} = \mathrm{m_{i-1}} + \delta\mathrm{m_i}, \tag{5.13}$$

with the model update (δm) given by

$$\delta\mathrm{m_i} = \left[\mathrm{J(m_i)^T J(m_i)} + \mu\mathrm{I}\right]^{-1} \mathrm{J(m_i)^T}\delta\mathrm{d}, \tag{5.14}$$

where, μ is a regularization weight, I is the identity matrix, ($^{\mathrm{T}}$) denotes the transpose operator and J(m) is the Jacobian or sensitivity matrix.

In the case of a two-layer near-surface model there are six parameters to be solved for $(z_1, z_2, s_0, s_1, \phi_1, \phi_2)$. The associated sensitivity matrix is

$$\mathrm{J(m)} = \left[\frac{\partial \mathrm{g(m)}}{\partial \mathrm{z_1}}, \frac{\partial \mathrm{g(m)}}{\partial \mathrm{z_2}}, \frac{\partial \mathrm{g(m)}}{\partial \mathrm{s_0}}, \frac{\partial \mathrm{g(m)}}{\partial \mathrm{s_1}}, \frac{\partial \mathrm{g(m)}}{\partial \phi_1}, \frac{\partial \mathrm{g(m)}}{\partial \phi_2}\right]. \tag{5.15}$$

Using the formulae developed in the previous section, values for each of the derivatives in equation 5.15 can be determined analytically. Expressions for each of these terms are listed in the Appendix A.

The inversion algorithm halts once a given number of iterations is reached or when a given threshold for the objective function is crossed. The Matlab codes I wrote for computing near-surface corrections and the inversion of the near-surface model parameters are listed in the Appendix B.

5.3 Synthetic Data Analysis

To examine the behavior of the inversion algorithm developed in the previous section, I computed PS converted-wave synthetic traces via raytracing using the software Omni. Figure

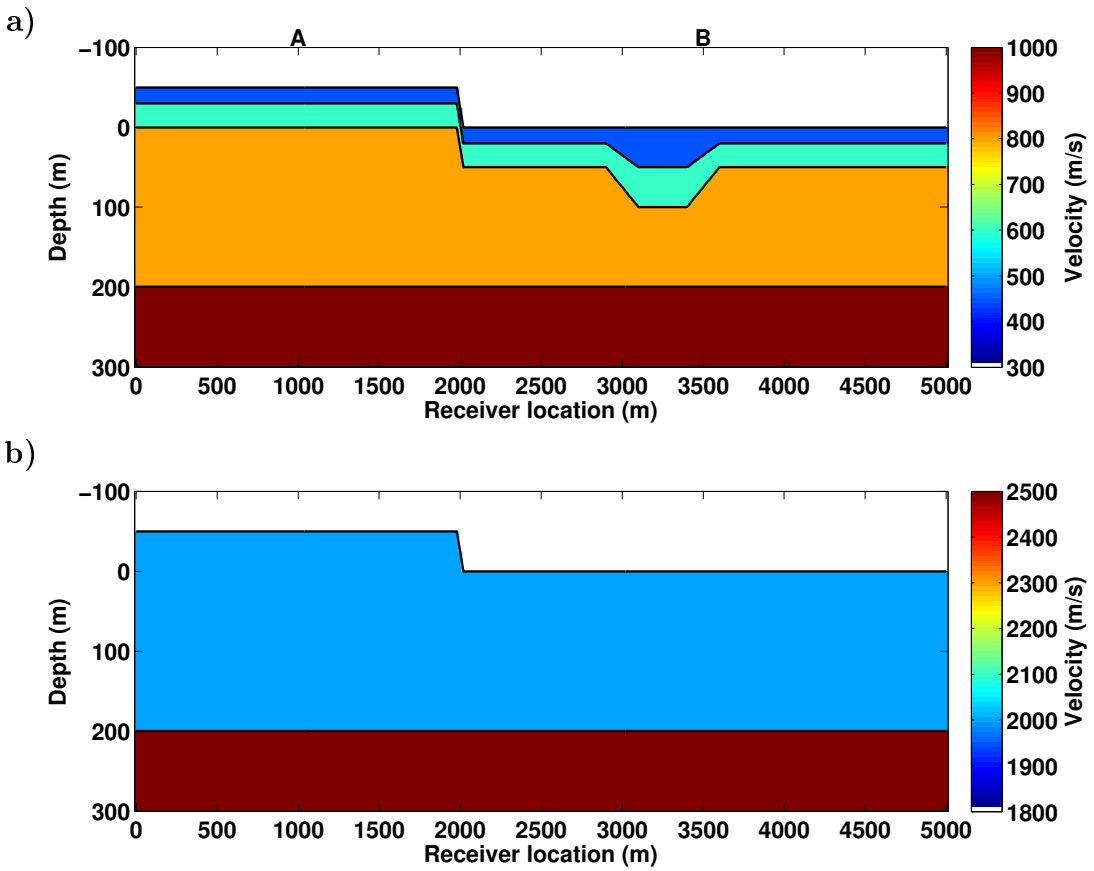

Figure 5.2: (a) S-wave and (b) P-wave velocity models used for raytracing PS-data. No near-surface velocity changes exist on the P-wave velocity model to simulate the case where P-wave near-surface effects have been already removed. Only P-wave elevation corrections are needed on the source side for this case.

5.2 displays the model used for the modelling. Notice that no P-wave velocity contrast exists between the near-surface layer and the medium beneath. This simulates the case where P-wave statics have already been removed. The S-wave velocity model consists of two near-surface layers with velocities of 450 m/s and 600 m/s, respectively. A channel-like anomaly is included on the right side of the model.

The effect of the near-surface structure on the travel times is evident on the source gather shown in Figure 5.3a. This gather corresponds to the data recorded from a source located at location B in Figure 5.2. The moveout of the converted-wave traveltimes has been clearly deformed by the presence of low S-wave velocities in the near-surface. In contrast, the

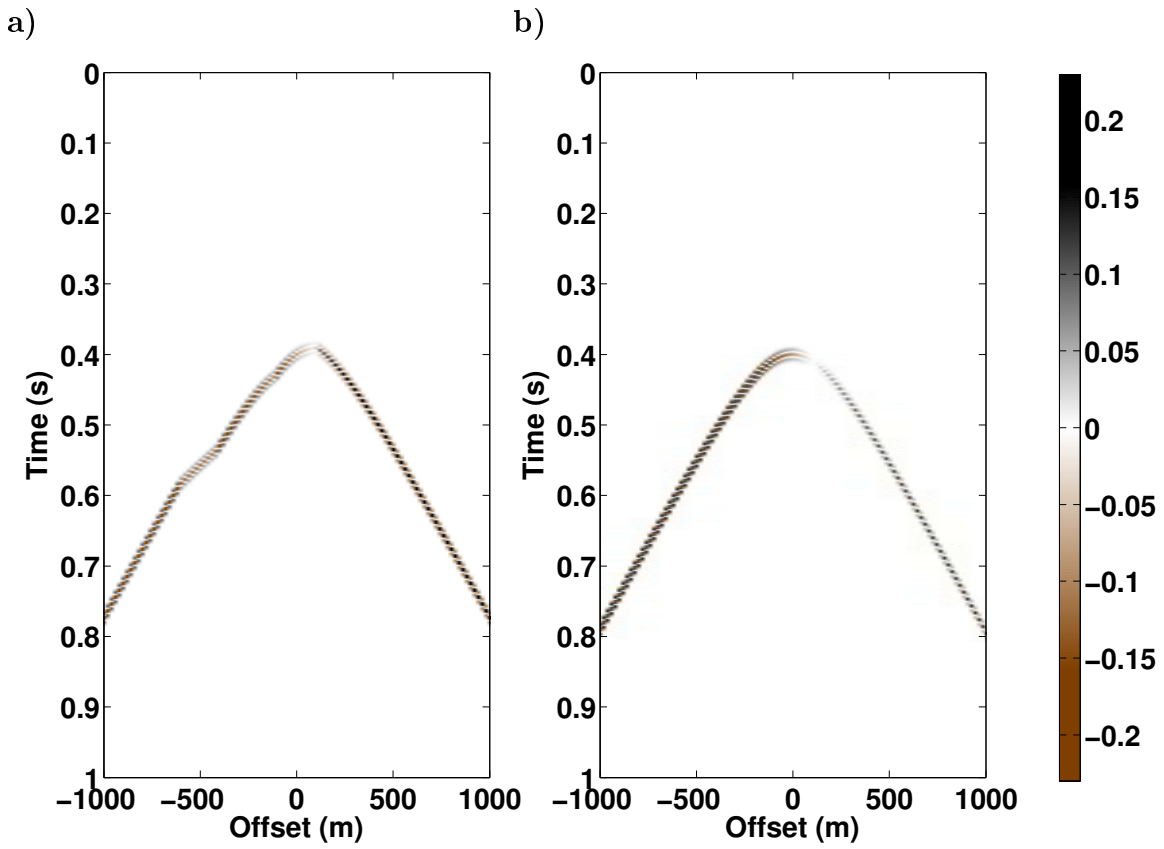

Figure 5.3: (a) Source and (b) receiver gathers obtained at location B in Figure 5.2. The imprint of the structure of the near-surface layers is very clear on the source gather. Since source-side elevation statics have been applied and no P-wave near-surface effects were modeled, the moveout of the event in the receiver gather (b) displays no deformation.

receiver gather recorded by a receiver at location B (Figure 5.3b), displays a more coherent moveout. Since there are no near-surface P-wave velocity changes, only P-wave elevation statics were used on the source side.

Even though S-wave near-surface effects are not evident on receiver gathers, they are highlighted when comparing gathers from different locations. I do such a comparison after transforming the data to the τ-p domain. Figure 5.4 displays two receiver gathers, corresponding to locations A and B in Figure 5.2, after transformation to the τ-p domain. The third panel to the right shows the output crosscorrelation functions and the picks at the maximum value of the functions. Notice that these picks closely match the modelled τ-differences predicted by equation 5.11. The two gaps around p=0 s/m and 0.19×10^{-3} s/m

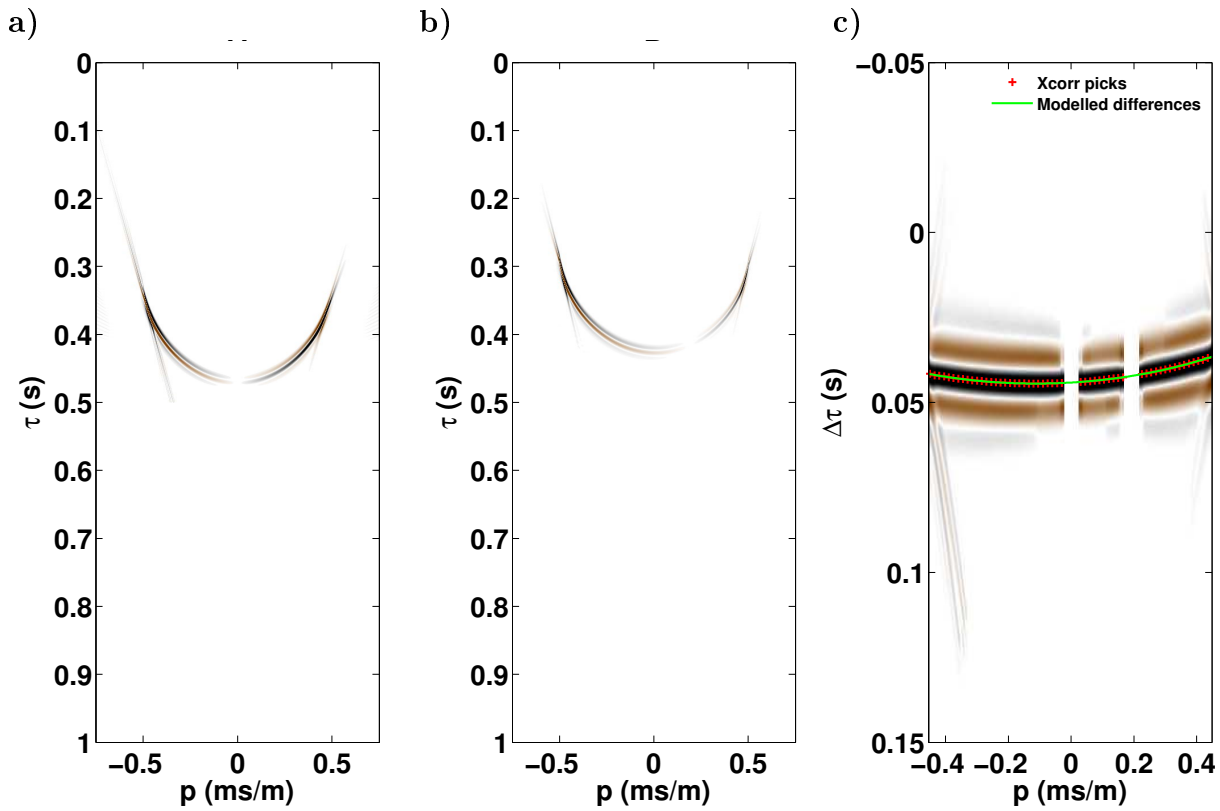

Figure 5.4: (a) τ-p receiver gathers obtained at locations (a) A and (b) B in Figure 5.2. (c) Crosscorrelation between (a) and (b). The maximum of the crosscorrelation functions match the τ-differences given by equation 5.11. The gaps in the crosscorrelation functions around $p = 0$ ms/m and $p = 0.2$ ms/m, correspond to the rayparameter values at which the normal incidence condition is achieved at each receiver location. Under this condition no converted-wave energy is expected.

are the result of the polarity reversals shown in Figure 5.3. Since the near-surface structure beneath the receiver location B is dipping, the location of this polarity reversal is shifted toward positive offsets. Polarity reversals should be addressed before τ-p transformation to avoid the presence of artifacts in the output.

Gaussian pseudo-random noise with zero mean and a standard deviation of 4 ms was added to the $\Delta\tau$-picks to simulate pick errors. Figure 5.5 shows the inversion results in the data domain. The initial guess for the τ-differences is equal to zero since the initial model parameters for location B were set equal to those in the reference location. After fifteen iterations the inversion converged to a solution very close to the actual model parameters.

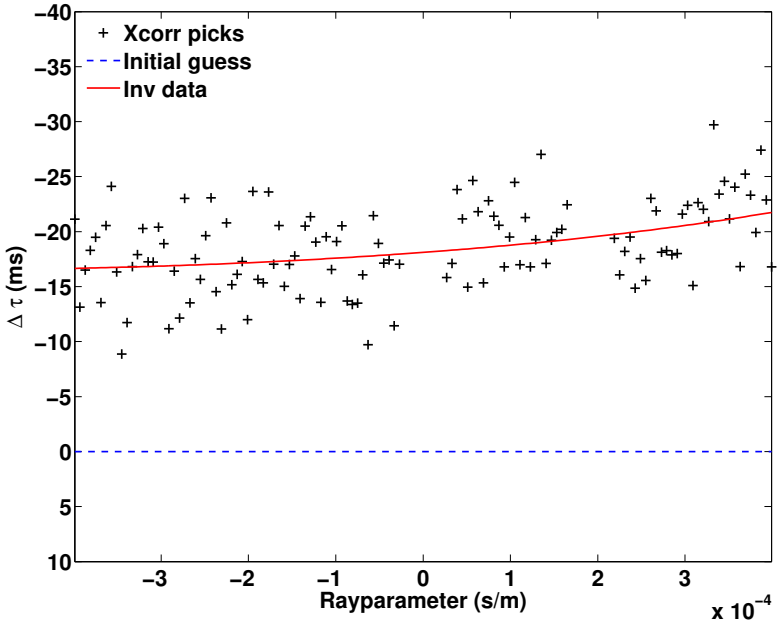

Figure 5.5: Inversion results obtained from the τ-differences captured in Figure 5.4c. The same parameters assumed to be known at location A were used as the initial guess for the parameters at location B. For this reason the initial model differences are zero. After fifteen iterations the inverted differences match the picked differences providing an estimation of the near-surface parameters at location B.

Data residuals dropped from 18.7 ms to 4.3 ms, slightly above the noise level. The depths the near-surface layers were estimated at 40.8 m and 65.4 m respectively. These represent errors of 5.8 m and -9.58 m in the z_1 and z_2 estimations, respectively.

This process is repeated for all receiver locations to invert for the near-surface structure. In Figure 5.6 the inverted S-wave velocity model for the near-surface is plotted. The dashed lines represent the actual depths of the two interfaces defined in the original model. In the area near the channel-like feature, the average absolute errors for the depths of the first and second interfaces were 8.4 m and 14.6 m, respectively. Outside of that area, the errors drop to 0.9 m and 0.6 m, respectively. Velocity estimations were stable along the model with average absolute errors of 0.76 m/s and 5.2 m/s for the first and second layers, respectively.

These synthetic data results illustrate the process of using the τ-differences captured by the crosscorrelation functions to obtain a S-wave velocity model for the near-surface. In the next section I apply this processing to a field dataset.

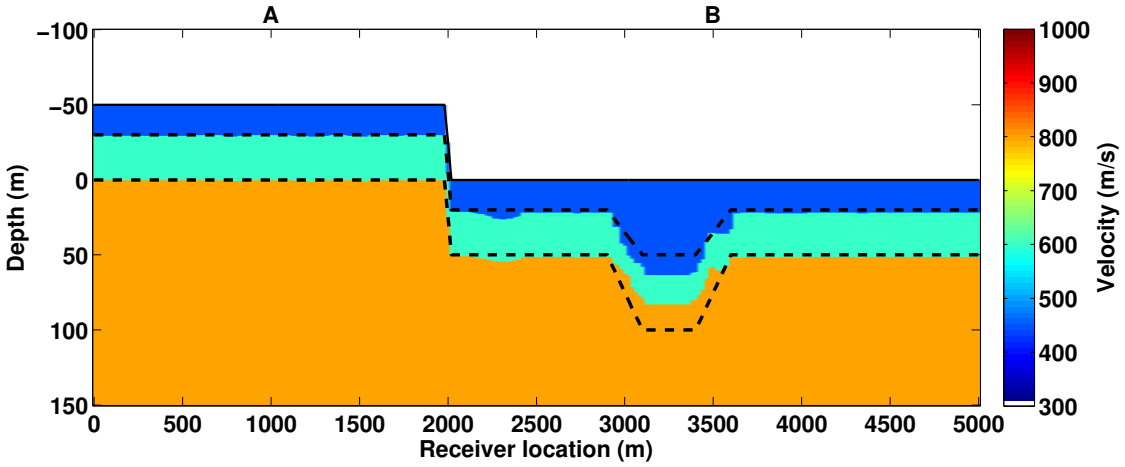

Figure 5.6: Near-surface S-wave velocity model inverted from the synthetic data. The dashed lines represent the actual depth of each velocity change. The average absolute errors are of 2.42 m and 3.52 m for the depth estimations and, 0.76 m/s and 5.2 m/s for the velocity estimations of the first and second layer, respectively.

5.4 Field data example

The field data used in this part of the study were acquired by the Consortium for Research in Elastic Waves Exploration Seismology (CREWES) in the Hussar area in Southern Alberta (Margrave et al., 2012). These data were also used in Section 4.3 to demonstrate the use of interferometric raypath-consistent near-surface corrections. In Figure 5.7 a common receiver stacked section is plotted, in which near-surface/elevation effects are present. Particularly in the vicinity of the receivers located between 1750 m and 2250 m along the line, all events display an important pull-down of about 100 ms. Higher frequency "jumps" with smaller magnitudes are also observed along the rest of the line. The vertical-component sections processed in this area display very continuous and coherent horizontal events (Henley, 2014b).

Figures 5.8a and 5.8b display two different receiver gathers after surface-wave removal and P-wave static correction. These receiver gathers correspond to locations A and B in Figure 5.7, respectively. The transformation of these gathers to the τ-p domain is plotted in Figures 5.8c and 5.8d. The τ-differences between the data recorded at these two receiver locations is captured by the crosscorrelation operation (Figure 5.8e).

The τ-lags associated with the maxima of the crosscorrelation functions are then extracted and input into the inversion scheme outlined previously. Figure 5.9 displays the

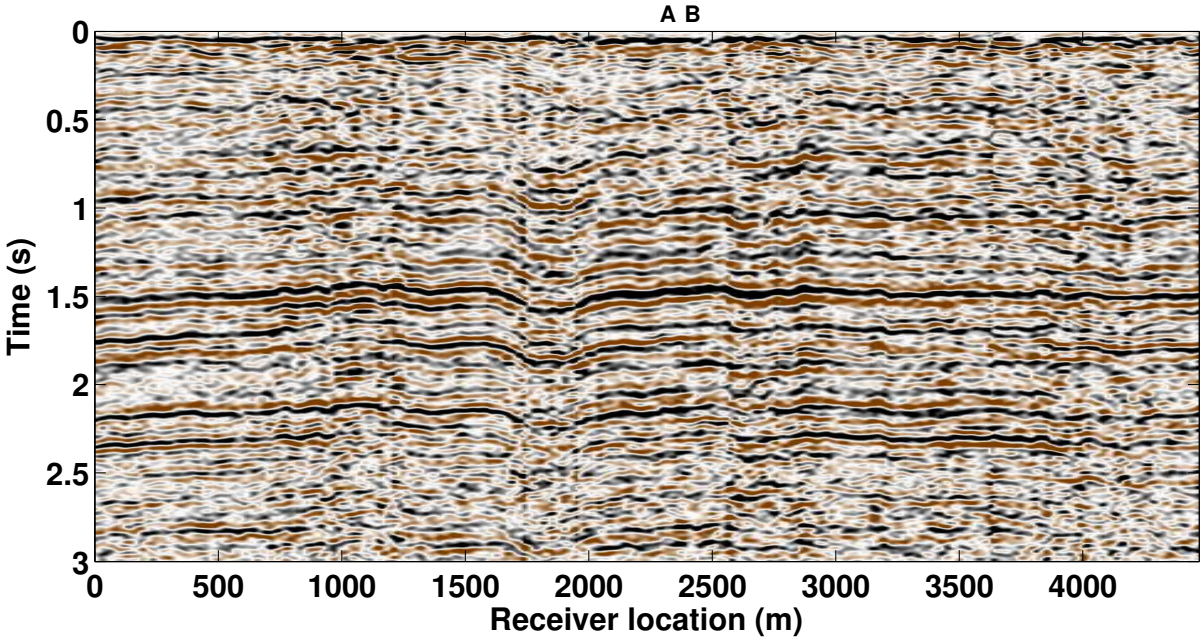

Figure 5.7: Common-receiver stacked section for the Hussar dataset. Only source side statics were applied at this stage. Notice the pull down of the events particularly on the traces around 1750 m along the line. Shorter wavelength shifts are also observed along the section.

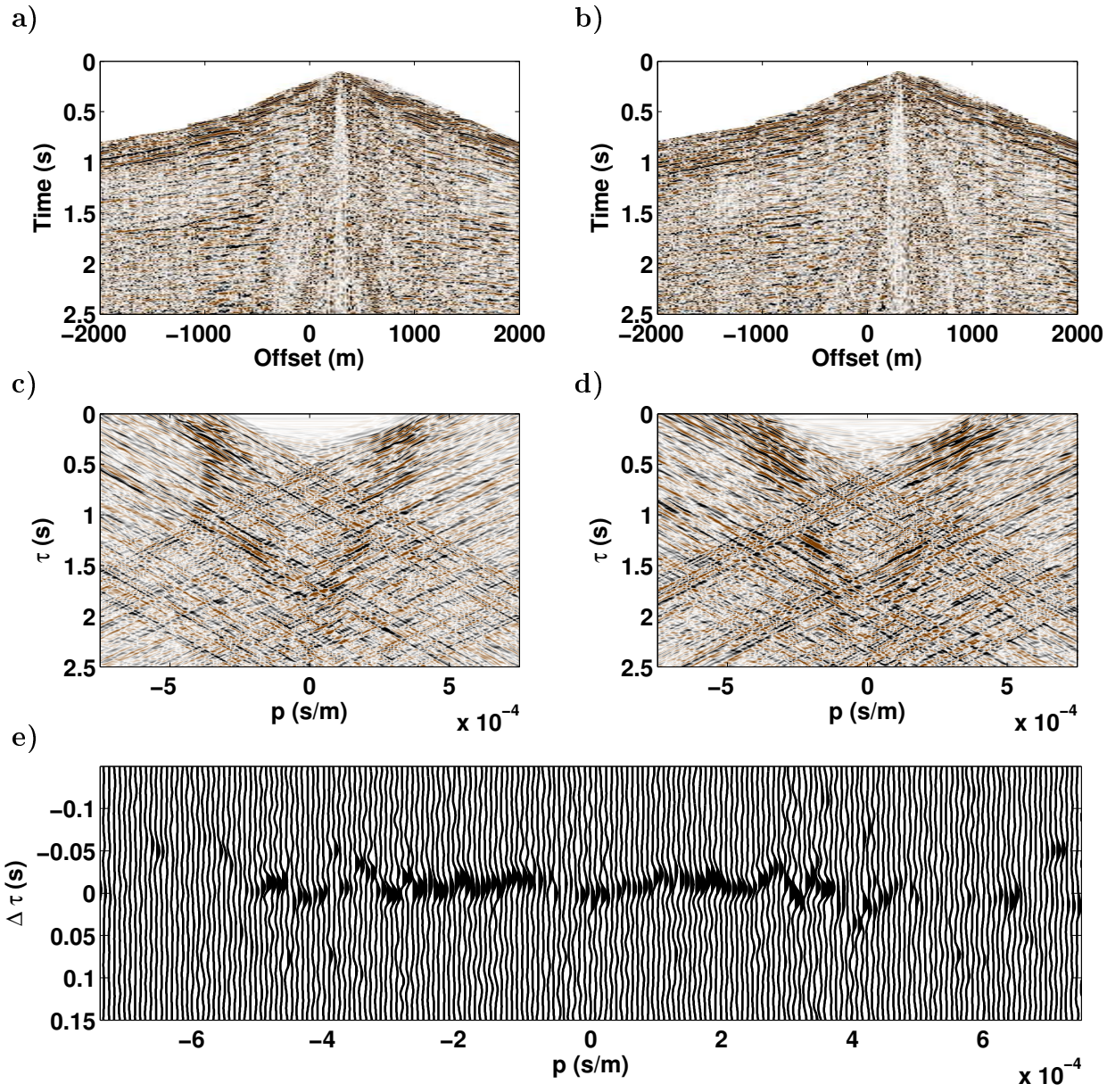

Figure 5.8: Receiver gathers recorded at the (a) reference and (b) estimation location and their τ-p representations (c) and (d), respectively. (e) Crosscorrelation between (c) and (d). Notice that the autocorrelation functions display significant energy for rayparameter values smaller than 3×10^4 s/m.

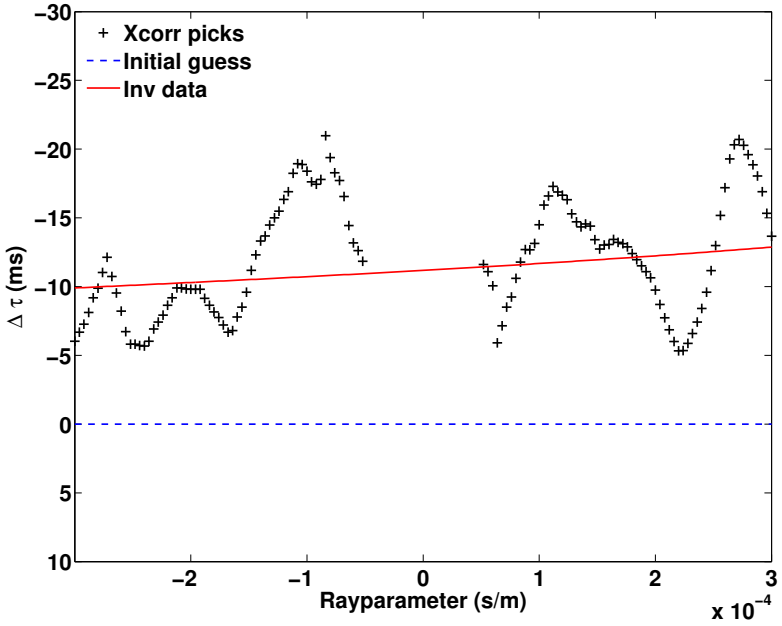

Figure 5.9: Data domain inversion results. Only τ-differences between 3×10^{-4} s/m and 0.5×10^{-4} s/m were used for the inversion. The average misfit between the final modeled data and the input data is 4.1 ms.

input and predicted data from the inverted model for this case. Absolute rayparameter values between 0.5×10^{-3} s/m and 3×10^{-3} s/m were used, because most of the crosscorrelation functions show good energy within this range. I chose not to use picks from rayparameter values lower than 0.5×10^{-3}, given that PS reflectivity is expected to be very low as the normal incidence condition is approached. The large crosscorrelation energy around $p = 0$ s/m could be the result of coherent noise still present in the data. The complex and coherent pattern of the picks might be the result of near-surface effects of short wavelength. These will not be removed using the near-surface corrections I derive from the inversion. Instead, a residual static correction will be needed before stacking the data to remove these effects.

The near-surface parameters for the reference location A were taken from a previous surface-wave velocity inversion study done with the same data (Askari et al., 2012). A two layer velocity model was assumed with $z_1 = 40$ m, $z_2 = 100$ m, $v_0 = 400$ m/s, $v_1 = 600$ m/s. The replacement velocity was set at 800 m/s and the final datum at 990 m. As the initial guess for the receiver location B I used the same parameters used for location A. For

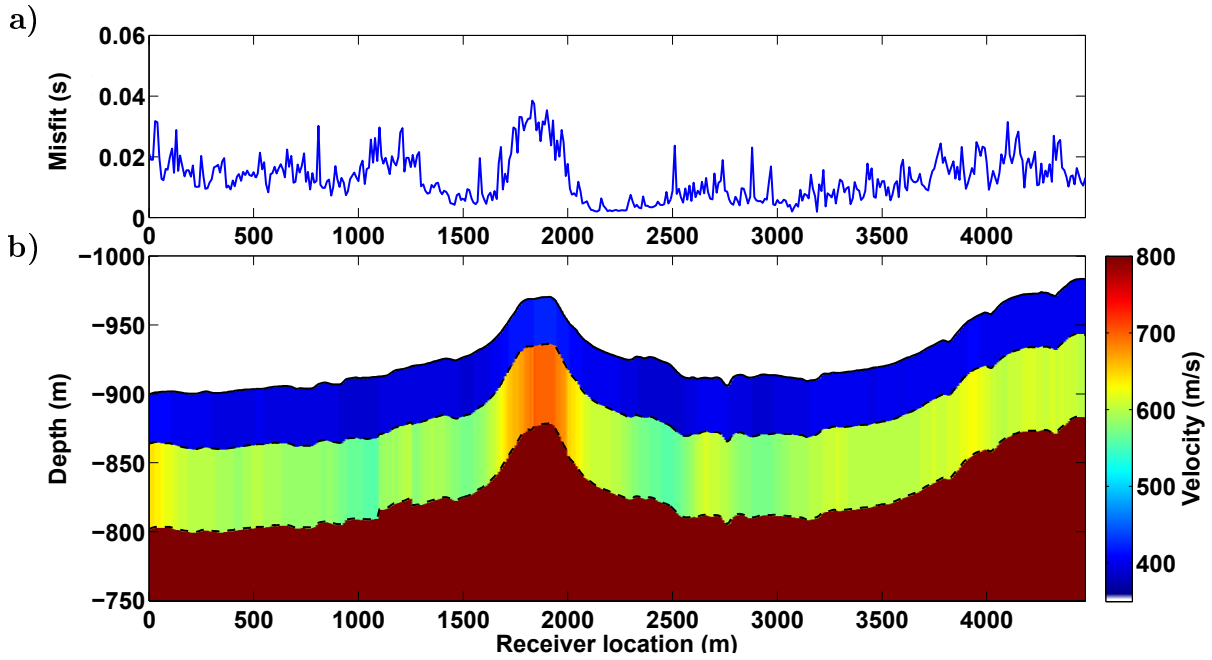

Figure 5.10: (a) Average inversion misfit per receiver location and (b) inverted near-surface S-wave velocity model for the field data. The average misfit along the line was 18 ms increasing up to 40 ms around the topographic high at 1750 m.

this reason, the τ differences modeled with the initial parameters are zeros. The inverted model for the receiver location B provided $z_1 = 43.2$ m, $z_2 = 101.7$ m, $v_0 = 390.2$ m/s and $v_1 = 568.6$ m/s, with an average misfit of 4.1 ms on the data domain.

In Figure 5.10 the inverted velocity model and the average misfit obtained at each receiver location are plotted. The largest velocity changes in the model are located near to the topographic high located around 1750 m. This anomaly appears to be the cause of the pull down observed on the initial common-receiver stack (Figure 5.7). The average misfit along the section is of 18 ms, decreasing to about 4 ms for the receivers closer to the reference location. The misfit increases in the area around the topographic high reaching values of 40 ms.

The rayparameter-dependent static corrections computed from this model are plotted in Figure 5.11. The correction due to elevation changes is displayed on Figure 5.11a and the component due to near-surface thickness and velocity variations is displayed on Figure

5.11b. Both corrections display similar absolute magnitude ranges for this dataset. Elevation corrections range between -50 ms and -110 ms while near-surface corrections range between 10 ms and 110 ms. The total static corrections displayed on Figure 5.11c are indicative of a negative correction around 1750 m that should remove the pull down present in the common receiver stack.

After applying the trace shifts indicated in Figure 5.11c to the τ-p receiver gathers the data were transformed back to the x-t domain. The new common receiver stack is displayed in Figure 5.12. Notice how all the deformations present in Figure 5.7 have been removed. Especially for times earlier than 1 s, more events are now visible and the data display an improved coherence.

For comparison, a common receiver stack obtained using a surface-consistent solution is displayed in Figure 5.13. There, events shallower than 1 s show significantly lower degree of continuity. Moreover, the overall coherency of the events in the section is lower than in Figure 5.12.

5.5 Remarks

Removing near-surface effects in a raypath-consistent framework provides stacked sections with enhanced coherence and resolution. My approach removes raypath-dependent near-surface effects while simultaneously extracting information about the velocities in the near-surface. In this way, the corrections applied to the data can be removed at later stages of the processing if needed. Also, the velocity information about the near-surface layers can be useful for building velocity models for migration or elastic full waveform inversion.

One limitation of the inversion algorithm presented here is that results are tied to one's knowledge of the velocity structure at the reference location. This could be mitigated by using more reference locations along the seismic line and creating a more complex initial velocity model.

The method I developed in this chapter provides an alternative approach to the application of S-wave near-surface corrections. In contrast to the approach used in chapter 4, the application the corrections can be performed via time shifts instead of a convolution

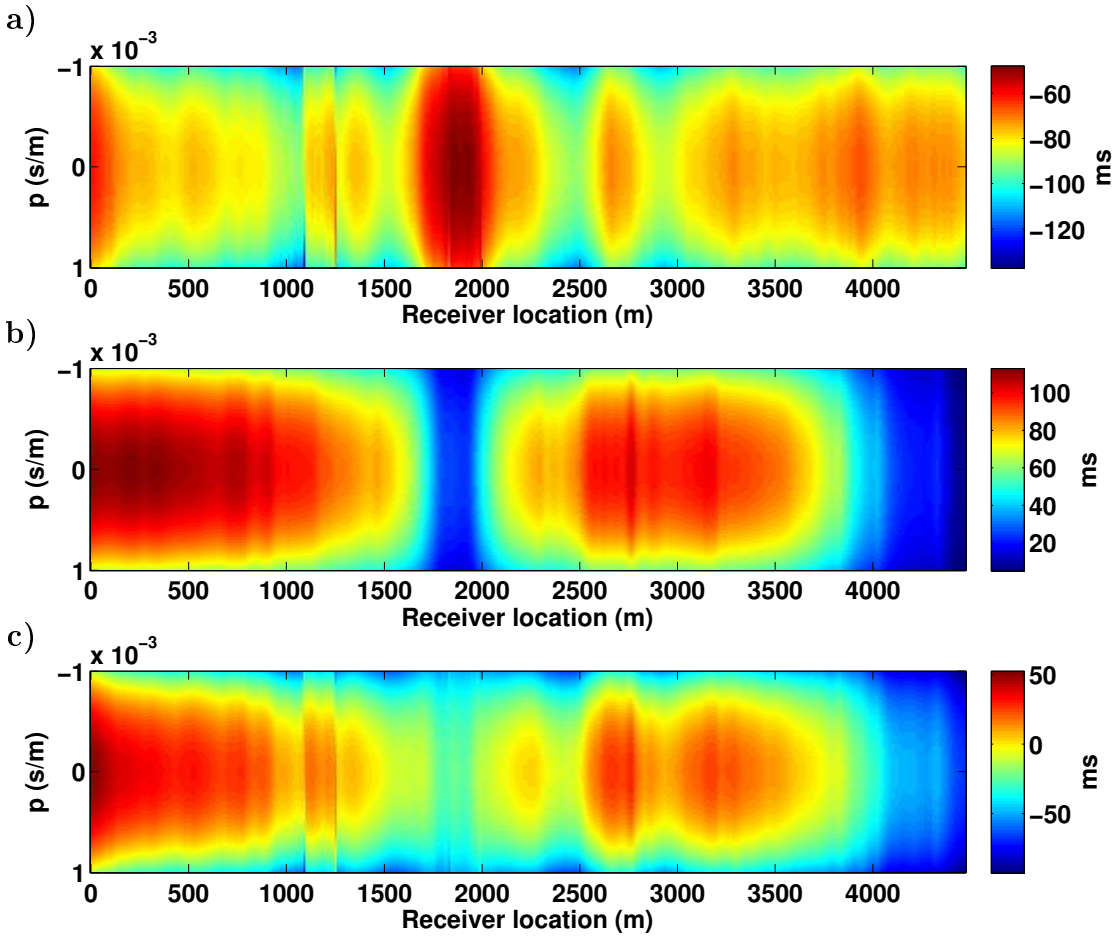

Figure 5.11: Rayparameter-dependent corrections: (a) elevation, (b) near-surface and (c) total corrections. A significant anomaly is observed on the three panels around 1750 m. In general the total near-surface correction changes from 50 ms at the origin of the section to -50 ms on the opposite side.

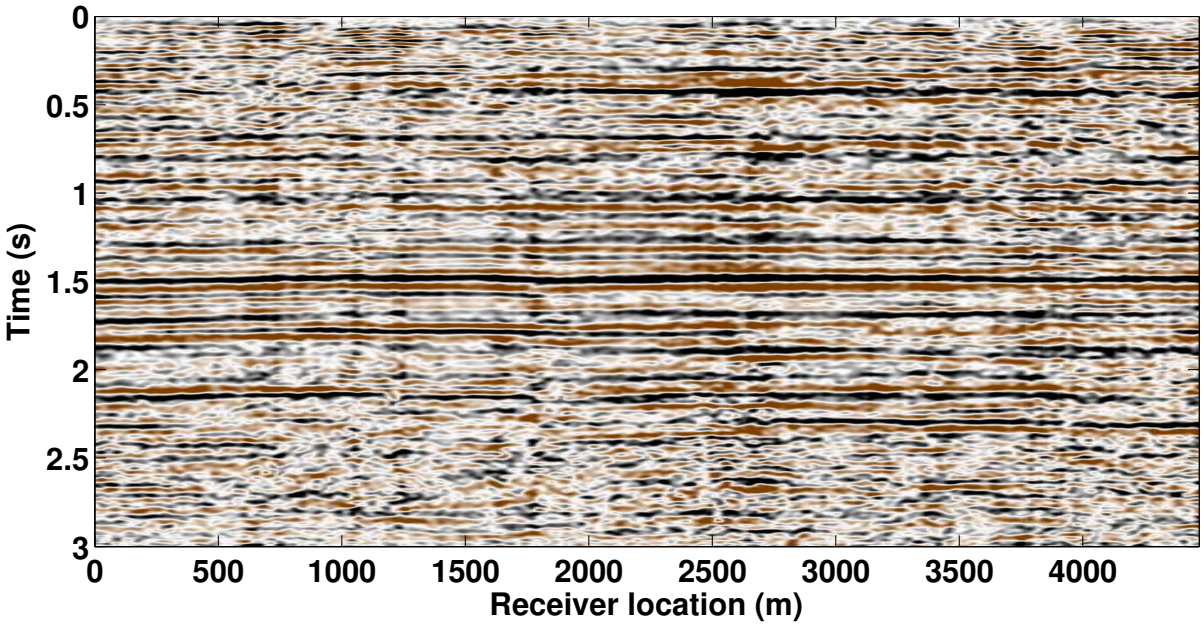

Figure 5.12: Common-receiver stacked section after applying rayparameter-dependent near–surface corrections. Notice how continuity and coherency of the events have been improved. Shallow events (<1 s) are now easier to identify. The deformations and shifts present in Figure 5.7 have been removed.

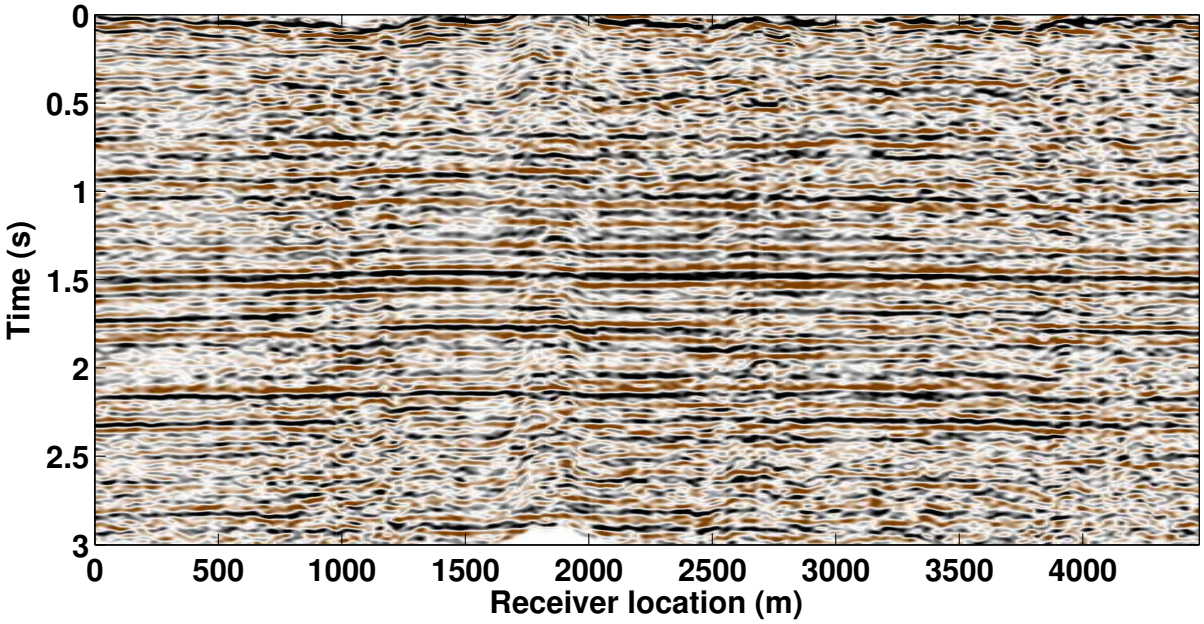

Figure 5.13: Common-receiver stacked section after applying surface-consistent static corrections. Even though the deformations and shifts have been removed the coherency and stacking power of shallow events is poor.

operation. Moreover, pilot trace panels are not required. Hence, there is no need to enforce continuity or smoothness on the events. The trade-off is that, since the correlation functions are not used as matching filters, reflection waveform variations associated with scattering or multi-path arrivals can not be accounted for in the correction.

Chapter 6

Discussion and Conclusions

The raypath-dependent framework for removing non-stationary near-surface effects presented in this thesis has been demonstrated to provide stacked sections with enhanced stack coherence.

Applying corrections in the τ-p domain relies on the ability to properly transform the data forward and backward the target domain. Therefore, knowing the limitations of the transformation process is very important. In the case of the τ-p transform some of these limitations are related to spatial sampling. In its continuous form, the Radon transform, on which the τ-p transform is based, is complete and invertible. The discrete form, however, is limited in the fidelity of its inversion by the range and number of offset values chosen for the transform (the aperture). The maximum offset available in the data effectively truncates the integral in equation 2.5. Therefore, amplitudes in τ-p domain must be treated carefully to preserve their resolution. A similar problem arises with the inverse transform. The number of p values available is usually chosen based on the number of traces in the input gather or a multiple of it. Aliasing criteria like the one proposed by Turner (1990) are also used to define the minimum number of p values that can be used without losing the information available in the input data. In any case, the infinite number of p values required by equation 2.6 is not available. For these reasons, I suggest testing the forward/inverse τ-p transform to find parameters that preserve the maximum resolution of the data without requiring unreasonable computer resources (memory and execution time).

Other limitations are related to subsurface conditions. According to Snell's law, rayparameters are constant only in a homogeneous horizontally layered medium. The derivation of the corrections I presented for a dipping near-surface layer considered that all interfaces are flat except for the base of the near-surface. Since near-surface velocities are much slower than in the subsurface one should expect that consistent traveltime shifts between consecutive receiver stations to be related with near-surface effects instead of structural effects. The term "consistent" plays an important role in this statement since the near-surface impacts

all the events recorded at a given location, regardless of their timing. However, structural effects might be limited to an specific time window and they might impact different events with different magnitudes. Therefore, as long as the time delays produced by the near-surface structure are larger than the delays introduced by the changes in the structure of the subsurface between receiver stations, the method proposed here should be valid. This is the case of smoothly variant structures like the one displayed in the Sinopec dataset. The performance of this method in structurally complex media remains to be studied.

One additional assumption in the work-flow is that source-side statics have already been corrected. Although this can be done by using refraction or tomography based methods, Henley (2012) showed that a similar approach to the one presented here can also be used. Regardless of the method, it is important that any distortion on the event's traveltimes that is not related to the subsurface or the S-wave velocities in the near-surface needs to be addressed before using this method. This includes topographic effects on the source side. After application of source-side statics, receiver gathered data should not be affected by changes in the elevation of the sources. This is an important condition for the τ-p transform to provide adequate results.

A single reference location was used in the inversion of the Hussar dataset, constraining the results to solutions close to the model parameters affecting the reference location. This setup provided very low misfit values (~ 4 ms) for the receivers nearby the reference location. However, these misfit levels could not be reached at any other location along the line. This implies that more than one reference location might be needed to obtain better results along larger seismic lines.

Regardless of the accuracy of the inverted model, the solution I presented here is one that can be removed at any time, since the velocity model is known. This contrasts with surface-consistent solutions based on stacking power optimization through residual static algorithms where the near-surface velocities remain unknown. In fact, my approach aims to extract the coherent component of the residual statics solution and translate it into a near-surface velocity model. Residual static algorithms should perform better after any coherent trend has been removed from the data.

Two different approaches for the application of S-wave static corrections in the τ-p domain

were presented in this thesis. The first approach aimed at applying near-surface corrections via interferometric processing of the near-surface effects. There, the output of the cross-correlation between raw traces and a set of pilot trace panels was used as matching filters. In this way, waveform variations due to scattering or multipath arrivals are included in the solution. The second approach was to use the τ-differences captured by crosscorrelation with a reference receiver gather to compute a S-wave velocity model for the near-surface. Then, corrections were computed from the output velocity model and applied via time shifts, instead of a convolution operation. This option can be appropriate for amplitude preserving work-flows since the original character of the waveform is affected at a minimum. Moreover, since pilot trace panel are not required, fewer constraints about the underlying geology are imposed. The limitation of this approach is that waveform variations are not accounted for. The convenience of either approach will depend on the final goal of the processing.

6.1 Future Work

Two different lines of work remain to be explored for improvements in the method I presented.

First, robust τ-p transformations able to handle the particular character of converted-waves are needed. Particularly requiring of attention are the changes in the phase of converted-wave events that are expected to happen around the critical angle. This type of AVO (amplitude-variation-with-offset) signature may introduce numerical artifacts during the transformation. This results in spurious events during the crosscorrelation and convolution operations. Also, extension of this method to 3D datasets will require the use of a 3D τ-p transform. The dissimilar spatial sampling in the inline and crossline directions of 3D surveys is one of the most important challenges on this regard.

Secondly, the output crosscorrelation functions resulting from the capture of the near-surface effects could be used directly within a waveform-based inversion. This will provide a tomographic-like solution with better resolution than the one presented here. Equation 5.3 can be interpreted as the τ contribution resulting from the propagation in a medium with thickness z_{i+1} and an effective velocity equal to $(q_{i+1} - q_i)$. Therefore, a crosscorrelation based inversion process could be used to find the effective velocity model that matches the

τ-differences captured from the data.

As a final remark, I would like to mention that the τ-p domain presents many advantages for the processing of converted-wave data. The most important one is that the asymmetry of the PS-raypath can be better accommodated in this domain. This is a result of the conservation of the rayparameter value p along both legs of the raypath. Also, many of the features of converted-waves that are angle-related, like AVO effects, could be better handled in this domain. It is my view that there is still room for improvement in the processing of converted-wave data and part of it requires to look into a more convenient domain for the processing of this type of data.

References

Alkhalifah, T. and Bagaini, C. (2006). Straight-rays redatuming: A fast and robust alternative to wave-equation-based datuming. *Geophysics*, 71(3):U37–U46.

Anno, P. (1983). Statics solutions and event correlations: two critical aspects of shear-wave exploration. *SEG Technical Program Expanded Abstracts 1983*, pages 347–349.

Askari, R., DeMeersman, K., and Ferguson, R. J. (2012). Estimation of near surface shear wave velocity using cmp cross-correlation of surface waves (CCSW). *SEG Technical Program Expanded Abstracts 2012*, pages 1–5.

Bagaini, C. and Alkhalifah, T. (2006). Application of the topographic datuming operator to a data setfrom the eastern arabian peninsula. *Geophysical Prospecting*, 54(6):731–737.

Berryhill, J. R. (1984). Wave-equation datuming before stack. *Geophysics*, 49(11):2064–2066.

Bessonova, E. N., Fishman, V. M., Ryaboyi, V. Z., and Sitnikova, G. A. (1974). The tau method for inversion of travel times-I. Deep seismic sounding data. *Geophysical Journal of the Royal Astronomical Society*, 36(2):377–398.

Blackburn, G. (1981). Seismic static corrections in irregular or steeply dipping water-bottom environments. *Exploration Geophysics*, 12(4):93–100.

Blyth, C. I., Fisher, N. J., and Heath, A. M. (1989). Dynamic time corrections and their application to seismic data over sea floor canyons in the gippsland basin. *Exploration Geophysics*, 20(1/2):237–243.

Bodet, L., van Wijk, K., Bitri, A., Abraham, O., Côte, P., Grandjean, G., and Leparoux, D. (2005). Surface-wave inversion limitations from laser-doppler physical modeling. *Journal of Environmental & Engineering Geophysics*, 10(2):151–162.

Chapman, C. H. (1978). A new method for computing synthetic seismograms. *Geophysical Journal of the Royal Astronomical Society*, 54(3):481–518.

Claerbout, J. F. (1975). Slant-stacks and radial traces. *Stanford Expl. Project Report*, SEP-5:1–12.

Claerbout, J. F. (1983). Ground roll and radial traces. *Stanford Expl. Project Report*, SEP-35:43–53.

Claerbout, J. F. (1985). Imaging the earth's interior. *Stanford Expl. Project Report*, pages 216–219.

Cova, R., Henley, D., and Innanen, K. A. (In press 2017). Computing near-surface velocity models for s-wave static corrections. *Geophysics*.

Cova, R., Henley, D., Wei, X., and Innanen, K. A. (2017). Receiver-side near-surface corrections in the τ-p domain: A raypath-consistent solution for converted wave processing. *Geophysics*, 82(2):U13–U23.

Cox, M. (1999). *Static Corrections for Seismic Reflection Surveys*. Geophysical references; v. 9. Society of Exploration Geophysicists.

Curtis, A., Gerstoft, P., Sato, H., Snieder, R., and Wapenaar, K. (2006). Seismic interferometryâĂŤturning noise into signal. *The Leading Edge*, 25(9):1082–1092.

Diebold, J. B. and Stoffa, P. L. (1981). The traveltime equation, tau-p mapping, and inversion of common midpoint data. *Geophysics*, 46(3):238–254.

Dulaijan, K. A. and Stewart, R. R. (2010). Using surface-wave methods for static corrections: a near-surface study at Spring Coulee, Alberta. *SEG Technical Program Expanded Abstracts 2010*, pages 1897–1901.

Eaton, D. W. S., Cary, P. W., and Schafer, A. W. (1991). Estimation of P-SV statics using stack-power optimization. *CREWES Research Report*, 3:32.1–32.18.

Fromm, G., Krey, T., and Wiest, B. (1985). Static and dynamic corrections. In Dohr, G., editor, *Seismic shear waves. Part A: Theory*, volume 15a of *Handbook of geophysical exploration*, pages 191–225. Geophysical Press.

Fromm, G., Krey, T., and Wiest, B. (1991). Accuracy and resolution of surface wave inversion. In Bhatia, S. K. and Blaney, G. W., editors, *Recent advances in instrumentation, data acquisition and testing in soil dynamics*, pages 17–32. Am. Soc. Civil Eng.

Gardner, L. W. (1939). An areal plan of mapping subsurface structure by refraction shooting. *Geophysics*, 4(4):247–259.

Garotta, R. and Granger, P. Y. (1988). Acquisition and processing of 3C × 3-D data using converted waves. *SEG Technical Program Expanded Abstracts 1988*, pages 995–997.

Hagedoorn, J. G. (1959). The plus-minus method of interpreting seismic refraction sections. *Geophysical Prospecting*, 7(2):158–182.

Hake, H. (1986). Slant stacking and its significance for anisotropy. *Geophysical Prospecting*, 34(4):595–608.

Henley, D. (2000). More radial trace domain applications. *CREWES Research Report*, 12:21.1–21.14.

Henley, D. (2012). Interferometric application of static corrections. *Geophysics*, 77(1):Q1–Q13.

Henley, D. (2014a). Static corrections via raypath interferometry: recent field experience. *CSEG Geoconvention 2014 Expanded abstracts*.

Henley, D. C. (2014b). Raypath interferometry vs. conventional statics: Recent field data and model comparisons. *SEG Technical Program Expanded Abstracts 2014*, pages 2040–2044.

Krey, T. (1978). Seismic stripping helps unravel deep reflections. *Geophysics*, 43(5):899–911.

Lawton, D. C. (1989). Computation of refraction static corrections using first-break traveltime differences. *Geophysics*, 54(10):1289–1296.

Lin, C. and Lin, C. (2007). Effect of lateral heterogeneity on surface wave testing: Numerical simulations and a countermeasure. *Soil Dynamics and Earthquake Engineering*, 27(6):541 – 552.

Margrave, G., Bertram, M., Bertram, K., Hall, K., Innanen, K., Lawton, D., Mewhort, L., and Phillips, T. (2012). A low-frequency seismic field experiment. *SEG Technical Program Expanded Abstracts 2012*, pages 1–5.

Operto, S., Gholami, Y., Prieux, V., Ribodetti, A., Brossier, R., Metivier, L., and Virieux, J. (2013). A guided tour of multiparameter full-waveform inversion with multicomponent data: From theory to practice. *The Leading Edge*, 32(9):1040–1054.

Ottolini, R. (1982). *Migration of reflection seismic data in angle-midpoint coordinates*. PhD thesis, Stanford University.

Palmer, D. (1980). *The Generalized Reciprocal Method of Seismic Refraction Interpretation*. Society of Exploration Geophysicists.

Schafer, A. W. (1991). Converted-wave statics methods comparison. *CREWES Research Report*, 3:8.107–8.125.

Schuster, G. (2009). *Seismic interferometry*. Cambridge University Press.

Schuster, G. T., Yu, J., Sheng, J., and Rickett, J. (2004). Interferometric/daylight seismic imaging. *Geophysical Journal International*, 157(2):838–852.

Sheriff, R. (2002). *Encyclopedic Dictionary of Applied Geophysics*. Society of Exploration Geophysicists, fourth edition.

Shtivelman, V. and Canning, A. (1987). Datum correction by wave equation extrapolation. *SEG Technical Program Expanded Abstracts 1987*, pages 454–457.

Socco, L. V., Boiero, D., Foti, S., Maraschini, M., Piatti, C., Bergamo, P., Garofalo, F., Pastori, M., and Molino, G. D. (2010). Surface wave analysis for S-wave static correction computation. *SEG Technical Program Expanded Abstracts 2010*, pages 1929–1933.

Stewart, R. R., Gaiser, J. E., Brown, R. J., and Lawton, D. C. (2002). Converted-wave seismic exploration: Methods. *Geophysics*, 67(5):1348–1363.

Stoffa, P. L. (1989). *Tau-p: A plane wave approach to the analysis of seismic data*. Kluwer Academic Publishers.

Survey, I. G. E., Edge, A., Laby, T., and Rivett, A. (1931). *The Principles & Practice of Geophysical Prospecting: Being the Report of the Imperial Geophysical Experimental Survey*. The University Press.

Tao, Y. and Sen, M. K. (2013). On a plane-wave based crosscorrelation-type seismic interferometry. *Geophysics*, 78(4):Q35–Q44.

Tatham, R. (1989). Tau-p filtering. In Stoffa, P., editor, *Tau-p: a plane wave approach to the analysis of seismic data*, volume 8 of *Modern Approaches in Geophysics*, pages 35–70. Springer Netherlands.

Tatham, R., McCormack, M., Neitzel, E., and Winterstein, D. (1991). *Multicomponent seismology in petroleum exploration*. Investigations in geophysics. Society of Exploration Geophysicists.

Tessmer, G., Krajewski, P., Fertig, J., and Behle, A. (1990). Processing of ps-reflection data applying a common conversion-point stacking technique. *Geophysical Prospecting*, 38(3):267–268.

Thomsen, L. (1999). Converted-wave reflection seismology over inhomogeneous, anisotropic media. *Geophysics*, 64(3):678–690.

Turner, G. (1990). Aliasing in the tau-p transform and the removal of spatially aliased coherent noise. *Geophysics*, 55(11):1496–1503.

Virieux, J. and Operto, S. (2009). An overview of full-waveform inversion in exploration geophysics. *Geophysics*, 74(6):WCC1–WCC26.

Wapenaar, C. P. A., Cox, H. L. H., and Berkhout, A. J. (1992). Elastic redatuming of multicomponent seismic data. *Geophysical Prospecting*, 40(4):465–482.

Wapenaar, K. (2004). Retrieving the elastodynamic Green's function of an arbitrary inhomogeneous medium by cross correlation. *Physical Review Letters*, 93:254301.1–254301.4.

Wapenaar, K. and Fokkema, J. (2006). GreenâĂŹs function representations for seismic interferometry. *Geophysics*, 71(4):SI33–SI46.

Wapenaar, K., van der Neut, J., Ruigrok, E., Draganov, D., Hunziker, J., Slob, E., Thorbecke, J., and Snieder, R. (2011). Seismic interferometry by crosscorrelation and by multidimensional deconvolution: a systematic comparison. *Geophysical Journal International*, 185(3):1335–1364.

Wenzel, F. (1988). Processing of wideâĂŘangle vibroseis data. *Geophysics*, 53(10):1303–1310.

Wiest, B. and Edelmann, H. A. K. (1984). Static corrections for shear wave sections. *Geophysical Prospecting*, 32:1091–1102.

Yilmaz, O. (2015). *Engineering Seismology with Applications to Geotechnical Engineering:*. Investigations in Geophysics. Society of Exploration Geophysicists.

Yilmaz, O. and Lucas, D. (1986). Prestack layer replacement. *Geophysics*, 51(7):1355–1369.

Appendix A

Inversion sensitivities

The elements of the Jacobian matrix in equation 5.15 are obtained by taking partial derivatives of equation 5.11 with respect to each one of the model parameters. In the case of a two-layer velocity model the sensitivities related to the depth of each interface are,

$$\frac{\partial \Delta\tau_{xcorr}}{\partial z_1} = q_1 - q_0, \tag{A.1}$$

$$\frac{\partial \Delta\tau_{xcorr}}{\partial z_2} = q_2 - q_1. \tag{A.2}$$

The derivatives with respect to the slownesses of the first two layers can be written as,

$$\frac{\partial \Delta\tau_{xcorr}}{\partial s_0} = -\frac{z_1 s_0}{q_{a,0}} \cos(\phi_1), \tag{A.3}$$

$$\frac{\partial \Delta\tau_{xcorr}}{\partial s_1} = \frac{s_1}{q_{a,0} q_{a,1}} \left[(z_2 - z_1) q_{a,0} \cos(\phi_2) + z_1 p_0 \sin(\phi_2 - \phi_1) \right]. \tag{A.4}$$

where,

$$p_0 = q_{a,0} \sin(\phi_1) + p_{a,0} \cos(\phi_1), \tag{A.5}$$

and,

$$p_{a,0} = p_1 \cos(\phi_1) - q_1 \sin(\phi_1). \tag{A.6}$$

Equations A.5 and A.6 represent the horizontal slownesses measured along the surface and the base of the first layer respectively.

The sensitivity to changes in the dip of the first interface is given by,

$$\frac{\partial \Delta\tau_{xcorr}}{\partial \phi_1} = \frac{z_1 p_0}{q_{a,0}} \left[q_{a,0} - p_1 \sin(\phi_1) - q_1 \cos(\phi_1) \right]. \tag{A.7}$$

Finally, I write the sensitivity to changes in the dip of the second interface in terms of the derivatives of the vertical slowness as,

$$\frac{\partial \Delta\tau_{xcorr}}{\partial \phi_2} = (z_1 - z_2) \frac{\partial q_1}{\partial \phi_2} - z_1 \frac{\partial q_0}{\partial \phi_2}, \tag{A.8}$$

with,

$$\frac{\partial q_1}{\partial \phi_2} = \frac{p_1}{q_{a,1}} \left[p \sin(\phi_2) + q_2 \cos(\phi_2) - q_{a,1} \right], \tag{A.9}$$

$$\frac{\partial q_0}{\partial \phi_2} = \frac{1}{q_{a,0} p_1} \left[q_1 \cos(\phi_1) - p_1 \sin(\phi_1) \right] \left[p_{a,0} \cos(\phi_1) - q_{a,0} \sin(\phi_1) \right] \frac{\partial q_1}{\partial \phi_2}. \tag{A.10}$$

Appendix B

Matlab codes

B.1 Rayparameter-dependent near-surface corrections

```
function [dtau,J]=taudiff(p,sr,s1,s2,z1,z2,phi1,phi2)
% taudiff: computes the rayparamter-dependent near-surface correction and
% its derivatives respect to each model parameter for a two-layers
% near-surface model
%
% [tau,difft]=taudiff(p,sr,s1,s2,z1,z2,phi1,phi2)
%
% p   ... vector of rayparameter values
% sr  ... replacement slowness
% s1  ... slowness of the first near-surface layer
% s2  ... slowness of the second near-surface layer
% z1  ... depth at the base of the first near-surface layer
% z2  ... depth at the base of the second near-surface layer
% phi1  ... dip at the base of the first near-surface layer
% phi2  ... dip at the base of the secod near-surface layer
%
% dtau   ... near-surface corrections to be applied in the tau-p domain
% difft: ... Jacobian matrix containin the derivatives of the
%            forward modelling operator respect to each model paramter
%            J=[dg/ds1 dg/ds2 dg/dz1 dg/dz2 dg/dphi1 dg/dphi2]
%
% R.J. Cova, 2017, CREWES
%
% NOTE: It is illegal for you to use this software for a purpose other
```

```
% than non-profit education or research UNLESS you are employed by a CREWES
% Project sponsor. By using this software, you are agreeing to the terms
% detailed in this software's Matlab source file.

% BEGIN TERMS OF USE LICENSE
%
% This SOFTWARE is maintained by the CREWES Project at the Department
% of Geology and Geophysics of the University of Calgary, Calgary,
% Alberta, Canada.  The copyright and ownership is jointly held by
% its author (identified above) and the CREWES Project.  The CREWES
% project may be contacted via email at:  crewesinfo@crewes.org
%
% The term 'SOFTWARE' refers to the Matlab source code, translations to
% any other computer language, or object code
%
% Terms of use of this SOFTWARE
%
% 1) Use of this SOFTWARE by any for-profit commercial organization is
%    expressly forbidden unless said organization is a CREWES Project
%    Sponsor.
%
% 2) A CREWES Project sponsor may use this SOFTWARE under the terms of the
%    CREWES Project Sponsorship agreement.
%
% 3) A student or employee of a non-profit educational institution may
%    use this SOFTWARE subject to the following terms and conditions:
%    - this SOFTWARE is for teaching or research purposes only.
%    - this SOFTWARE may be distributed to other students or researchers
%      provided that these license terms are included.
%    - reselling the SOFTWARE, or including it or any portion of it, in any
```

```
%      software that will be resold is expressly forbidden.
%    - transfering the SOFTWARE in any form to a commercial firm or any
%      other for-profit organization is expressly forbidden.
% END TERMS OF USE LICENSE

p=p(:); %ensure p is a column vector

qr=sqrt(sr^2-p.^2); %vertical slowness in the replacement medium

%slownesses parallel and perpendicular to the base of the second layer
pa2=p*cos(phi2)-qr*sin(phi2);
qa2=sqrt(s2.^2-pa2.^2);

%horizontal and vertical slowness in the second layer
p2=qa2*sin(phi2)+pa2*cos(phi2);
q2=qa2*cos(phi2)-pa2*sin(phi2);

%slownesses perpendicular and parallel to the base of the first layer
pa1=p2*cos(phi1)-q2*sin(phi1);
qa1=sqrt(s1.^2-pa1.^2);

%horizontal and vertical slownesses in the first layer
p1=qa1*sin(phi1)+pa1*cos(phi1);
q1=qa1*cos(phi1)-pa1*sin(phi1);

dtau=z1.*(q2-q1)+z2.*(qr-q2); %near-surface correction

%derivatives respect to the depth of each layer
dtdz1=(q2-q1);
dtdz2=(qr-q2);
```

```
85
86  %derivatives respect to the slowness of each layer
87  dtds1=-z1.*s1.*cos(phi1)./qa1;
88  dtds2=(s2./qa2).*((z1-z2).*cos(phi2)+z1.*sin(phi2-phi1).*(p1./qa1));
89
90  %derivatives respect to the dip of each layer
91  dtdphi1=-z1.*((p2.*sin(phi1)+q2.*cos(phi1)).*(p1./qa1)-...
92      sin(phi1)*qa1-cos(phi1).*pa1);
93
94  dq1dphi2=(p2./qa2).*(p.*sin(phi2)+qr.*cos(phi2)-qa2);
95  dqodphi2=(p.*sin(phi2)+qr.*cos(phi2)-qa2).*(q2.*cos(phi1)+...
96      p2.*sin(phi1)).*p1./(qa2.*qa1);
97  dtdphi2=(z1-z2).*dq1dphi2-z1.*dqodphi2;
98
99  J=[dtds1 dtds2 dtdz1 dtdz2 dtdphi1 dtdphi2]; %output Jacobian matrix
100
101 end
```

B.2 Inversion of near-surface model parameters from τ-differences

```
function [minv,dtauf]=TauPNearSurfInv(dtau,p,sr,zref,zrec,m0,mref,u,scal)
% TauPNearSurfInv: computes a 2-layers near-surface velocity model from the
% tau-differences between a reference location and the current location
%
% [minv,tauf,objf]=TauPNearSurfInv(dtau,p,sr,zref,zrec,m0,mref,u,scal)
%
% dtau  ... tau-differences between two receiver or source locations
% p     ... rayparameter values
% sr    ... replacement slowness
% zref  ... surface elevation at reference location
% zrec  ... surface elevation at current receiver location
% m0    ... vector containing initial guess for the slownesses, depths and
%         dips of each layer. (e.g. m0=[s1 s2 z1 z2 dip1 dip2])
% mref  ... vector containing the slownesses, depths and
%         dips of each layer at the reference location.
%         (e.g. mref=[s1ref s2ref z1ref z2ref dip1ref dip2ref])
% u     ... regularization weight
% scal  ... scale factor for tau-differences and slownesses. This scale
%           factor has an important effect in the trade-off between the
%           thickness and velocity values during the inversion
%
%Note: tau-difference values, thicknesses and slownesses must be input in
%consistent units. Dip values must be input in radians.
%
% minv   ... vector containing inverted model parameters
%            (minv=[s1inv s2inv z1inv z2inv dip1inv dip2inv])
% tauf:  ... tau-differences modelled using inverted parameters
%
```

```
% R.J. Cova, 2017, CREWES
%
% NOTE: It is illegal for you to use this software for a purpose other
% than non-profit education or research UNLESS you are employed by a CREWES
% Project sponsor. By using this software, you are agreeing to the terms
% detailed in this software's Matlab source file.

% BEGIN TERMS OF USE LICENSE
%
% This SOFTWARE is maintained by the CREWES Project at the Department
% of Geology and Geophysics of the University of Calgary, Calgary,
% Alberta, Canada.  The copyright and ownership is jointly held by
% its author (identified above) and the CREWES Project.  The CREWES
% project may be contacted via email at:  crewesinfo@crewes.org
%
% The term 'SOFTWARE' refers to the Matlab source code, translations to
% any other computer language, or object code
%
% Terms of use of this SOFTWARE
%
% 1) Use of this SOFTWARE by any for-profit commercial organization is
%    expressly forbidden unless said organization is a CREWES Project
%    Sponsor.
%
% 2) A CREWES Project sponsor may use this SOFTWARE under the terms of the
%    CREWES Project Sponsorship agreement.
%
% 3) A student or employee of a non-profit educational institution may
%    use this SOFTWARE subject to the following terms and conditions:
%    - this SOFTWARE is for teaching or research purposes only.
```

```
%    - this SOFTWARE may be distributed to other students or researchers
%      provided that these license terms are included.
%    - reselling the SOFTWARE, or including it or any portion of it, in any
%      software that will be resold is expressly forbidden.
%    - transfering the SOFTWARE in any form to a commercial firm or any
%      other for-profit organization is expressly forbidden.
% END TERMS OF USE LICENSE

%setting default parameters for u and scal
if nargin <6
    u=1e-3;
end

if nargin <7
    scal=1;
end
%
%computing replacement vertical slowness and elevation correction
qrs=sqrt(sr^2-p.^2);
elevcorr=(zref-zrec).*qrs;
dtau=dtau-elevcorr';

%scaling slownesses and tau-differences
dtau=dtau.*scal;
p=p.*scal;
s0ref=mref(1).*scal;
s1ref=mref(2).*scal;

%extracting model parameter at reference location
z1ref=mref(3);
```

```
89  z2ref=mref(4);
90  phi1ref=mref(5);
91  phi2ref=mref(6);
92
93  %modelling near-surface correction at the reference location
94  [tauref]=taudiff(p,sr,s0ref,s1ref,z1ref,z2ref,phi1ref,phi2ref);
95
96  niter=15; %maximum number of iterations
97
98  %initializing variables
99  objf=zeros(niter,1);
100 m=zeros(6,niter);
101 m(:,1)=m0;
102 I=eye(6);
103
104 %modelling near-surface correction using the initial guess
105 [taum,J]=taudiff(p,sr,m0(1),m0(2),m0(3),m0(4),m0(5),m0(6));
106
107 %computing tau-differences
108 taum=taum-tauref;
109
110 %checking if initial guess and its derivatives provide real solutions
111 if ~isreal(taum) || ~isreal(J)
112     disp('Derivatives or tau values are imaginary: Check initial parameters'
        )
113     minv=mref;
114     dtauf=taum;
115     return
116 end
117
```

```
%computing initial residuals and objective function values
R=taum-dtau;
objf(1)=R'*R;

%only run the inversion if initial tau-differences are significative.
%Otherwise model parameters at the current and reference location should be
%the same

kk=2; %initializing iterations counter
if norm(dtau)>=1e-12

    while kk<=niter
        %computing model update
        dm=((J'*J)+u*I)\(J'*R);
        m(:,kk)=m(:,kk-1)-dm;

        %modelling near-surface corrections with new model parameters
        [taum,J]=taudiff(p,sr,m(1,kk),m(2,kk),m(3,kk),m(4,kk),m(5,kk),m(6,kk
            ));

        %computing new tau-differences
        taum=taum-tauref;

        %updating residuals and objective function
        R=taum-dtau;
        objf(kk)=R'*R;

        kk=kk+1; %updating counter
    end
else
```

```
147     disp('break')
148     m(:,kk)=mref;
149 end
150 
151 minv=m(:,end); %output inverted model parameters
152 dtauf=taum; %output modelled tau-diferences using inverted parameters
```

Copyright and Permissions